UNIVERSIDADE ESTADUAL DE CAMPINAS

INSTITUTO DE FÍSICA "GLEB WATAGHIN"

ANDRÉ VIEIRA DA SILVA

Simulando colisões de íons pesados usando um modelo híbrido baseado em QCD e espalhamento hadrônico

Simulating heavy-ion collisions using a hybrid model based on QCD and hadronic rescattering

Campinas

2020

André Vieira da Silva

Simulating heavy-ion collisions using a hybrid model based on QCD and hadronic rescattering

Simulando colisões de íons pesados usando um modelo híbrido baseado em QCD e espalhamento hadrônico

Tese apresentada ao Instituto de Física "Gleb Wataghin" da Universidade Estadual de Campinas como parte dos requisitos exigidos para a obtenção do título de Doutor em Ciências, na área de Física.

Thesis presented to the "Gleb Wataghin" Institute of Physics of the University of Campinas in partial fulfillment of the requirements for the degree of Doctor of Science, in the area of Physics.

Supervisor/Orientador: Prof. Dr. David Dobrigkeit Chinellato

Este trabalho corresponde à versão final da Tese defendida pelo aluno André Vieira da Silva, e orientada pelo Prof. Dr. David Dobrigkeit Chinellato.

Campinas

2020

Ficha catalográfica
Universidade Estadual de Campinas
Biblioteca do Instituto de Física Gleb Wataghin
Lucimeire de Oliveira Silva da Rocha - CRB 8/9174

Si38s

Silva, André Vieira da, 1987-
Simulating heavy-ion collisions using a hybrid model based on QCD and hadronic rescattering / André Vieira da Silva. – Campinas, SP : [s.n.], 2020.

Orientador: David Dobrigkeit Chinellato.
Tese (doutorado) – Universidade Estadual de Campinas, Instituto de Física Gleb Wataghin.

1. Cromodinâmica quântica. 2. Fenomenologia de íons pesados. 3. Colisões entre íons pesados. I. Chinellato, David Dobrigkeit, 1983-. II. Universidade Estadual de Campinas. Instituto de Física Gleb Wataghin. III. Título.

Informações para Biblioteca Digital

Título em outro idioma: Simulando colisões de íons pesados usando um modelo híbrido baseado em QCD e espalhamento hadrônico
Palavras-chave em inglês:
Quantum chromodynamics
Heavy ion phenomenology
Heavy ion collisions
Área de concentração: Física
Titulação: Doutor em Ciências
Banca examinadora:
David Dobrigkeit Chinellato [Orientador]
Arthur Marques Moraes
Matthew William Luzum
Ernesto Kemp
Pedro Cunha de Holanda
Data de defesa: 27-08-2020
Programa de Pós-Graduação: Física

Identificação e informações acadêmicas do(a) aluno(a)
- ORCID do autor: https://orcid.org/0000-0003-4923-023X
- Currículo Lattes do autor: http://lattes.cnpq.br/7580978088452236

MEMBROS DA COMISSÃO JULGADORA DA TESE DE DOUTORADO DE **ANDRÉ VIEIRA DA SILVA – RA 83252** APRESENTADA E APROVADA AO INSTITUTO DE FÍSICA "GLEB WATAGHIN", DA UNIVERSIDADE ESTADUAL DE CAMPINAS, EM 27 / 08 / 2020.

COMISSÃO JULGADORA:

- Prof. Dr. David Dobrigkeit Chinellato – Orientador – DRCC/IFGW/UNICAMP
- Prof. Dr. Arthur Marques Moraes – CBPF
- Prof. Dr. Matthew William Luzum – IF/USP
- Prof. Dr. Ernesto Kemp – DRCC/IFGW/UNICAMP
- Prof. Dr. Pedro Cunha de Holanda – DRCC/IFGW/UNICAMP

OBS.: Ata da defesa com as respectivas assinaturas dos membros encontra-se no SIGA/Sistema de Fluxo de Dissertação/Tese e na Secretaria do Programa da Unidade.

CAMPINAS
2020

Acknowledgements

First and foremost, I would like to express my deepest gratitude to my advisor Prof. Dr. David Dobrigkeit Chinellato for the continuous and incredible support to my Ph.D. studies and research, for his patience, motivation, enthusiasm, and immense knowledge. This work would not have been possible without his help and guidance my journey would be more difficult. I would also like to thank the Prof. Dr. Jun Takahashi and Prof. Dr. Giorgio Torrieri for discussions, criticisms and suggestions regarding to this work.

When I started to develop this project the collaboration with Christian Bierlich from Lund University (LU) was an important contribution for this work and I would like to express my appreciation and gratitude for his help.

I would also like to give very special thanks to the incredible people from the Experimental Hadronic Physics Group (HadrEx) at the "Gleb Wataghin" Institute of Physics (IFGW) at University of Campinas (UNICAMP), especially Dr. Rafael Derradi de Souza, Prof. Dr. Tiago Nunes, Dr. Danilo Silva de Albuquerque, Dr. Willian Matioli Serenone, Dr. Maurício Hippert, Prof. Dr. Edmilson José Tonelli Manganote, Lugas Salgado, Gabriel Reis Garcia and Kayman Jhosef for the support, criticism, suggestions and discussions that were very important in the development this thesis.

During my studies in the beginning of my Ph.D. I would like to thank Prof. Dr. José Augusto Chinellato, Profa. Dra. Carola Dobrigkeit Chinellato and Prof. Dr. Orlando Peres from DRCC/IFGW/UNICAMP for teaching and guidance on the field of particle physics. This fundamental knowledge allowed me to start on the field research of phenomenology of heavy-ion collisions.

I would also like to thank the professors for the discussions and insightful comments about this work: Prof. Dr. Arthur Marques Moraes (CBPF), Prof. Dr. Matthew William Luzum (IF/USP), Profa. Dra. Arlene Cristina Aguilar (DRCC/IFGW/UNICAMP),

Prof. Dr. Ernesto Kemp (DRCC/IFGW/UNICAMP) and Prof. Dr. Pedro Cunha de Holanda (DRCC/IFGW/UNICAMP).

We acknowledge the support from the Brazilian National Council for Scientific and Technological Development (CNPq) through the process number 165762/2014-4. This study was financed in part by the Coordenação de Aperfeiçoamento de Pessoal de Nível Superior - Brasil (CAPES) - Finance Code 001. I would also like to thank the John David Rogers Computing Center (CCJDR) in the Institute of Physics "Gleb Wataghin", University of Campinas for providing the computing power to this work.

Resumo

Em condições normais, a matéria nuclear é constituída de quarks confinados em hádrons, como o próton e o nêutron. Porém, em condições de densidade de energia muito alta, é esperado que seja formado um plasma de quarks e glúons, o 'Quark-Gluon Plasma' (QGP), no qual quarks e glúons encontram-se desconfinados. Essa matéria em condições extremas pode ser recriada no laboratório, o que é feito atualmente nos aceleradores RHIC, em Nova Iorque, nos Estados Unidos, e LHC, em Genebra, na Suíça.

A modelagem destes sistemas é extremamente desafiadora e é usualmente feita através de uma descrição efetiva do QGP na qual é empregada hidrodinâmica relativística para expandir um fluído semi-contínuo, efetivamente utilizando as interações da QCD apenas indiretamente via uma equação de estado que é usada na hidrodinâmica. Neste trabalho, nós nos propomos a não seguir este molde e acoplamos um simulador de interações nucleares inspirado na QCD, o PYTHIA/Angantyr, e um simulador de cascata hadrônica, o UrQMD, para simular colisões nucleares isentas de QGP e nas quais a modelagem é feita de forma tal que cada interação é acompanhada de forma precisa pelos modelos.

Os resultados da nossa cadeia de simulação PYTHIA/Angantyr + UrQMD indicam que vários dos sinais usualmente atribuídos exclusivamente à presença de um QGP na realidade já aparecem mesmo na ausência deste. Desta forma, este trabalho sugere fortemente que é necessária mais atenção a modelos controle, nos quais não há QGP, para isolar efeitos exclusivamente devidos ao QGP. Finalmente, este trabalho ainda aponta uma direção nova para a modelagem de colisões de íons pesados na qual as interações são todas rastreadas e realizadas individualmente, ao contrário do que é usualmente feito na literatura de colisão de íons pesados.

Palavras-chave: Cromodinâmica quântica, Fenomenologia de íons pesados, Colisões entre íons pesados

Abstract

In typical conditions, nuclear matter is comprised of quarks confined into hadrons such as protons and neutrons. However, at very high energy densities, matter may undergo a phase transition into a quark-gluon plasma (QGP) in which quarks and gluons are no longer confined into hadrons. This exotic state of matter can be recreated in a laboratory by colliding two heavy nuclei at relativistic energies, as is done at RHIC, in New York, USA, as well as at the LHC, in Geneva, Switzerland.

Modeling the evolution of the QGP is a very challenging task that is usually done employing an effective description using hydrodynamics to expand a fluid. In these codes, base QCD interactions are only sampled indirectly and are encoded in an Equation of State that is used in hydrodynamics. In this work, we propose an alternate approach in which we use a QCD-inspired nuclear collision simulator, PYTHIA/Angantyr, coupled to a hadronic cascade simulator, UrQMD, to generate a full nuclear collision without a QGP and in which each and every interaction is tracked individually and modeled to the best of our knowledge in terms of QCD.

The results from this PYTHIA/Angantyr + UrQMD simulation chain suggest that several signatures of the QGP are already present even in a system in which no locally equilibrated plasma is present. Therefore, this work suggests that further developments in control models in which no QGP is present is needed to truly isolate QGP-related effects. Finally, this work also points to a bold new direction in heavy-ion collision modeling in which all interactions are tracked and executed individually with QCD as much as possible, in contrast to the vast majority of modeling efforts in the field of heavy-ion collision.

Keywords: Quantum chromodynamics, Heavy ion phenomenology, Heavy ion collisions

List of Figures

List of Tables

Contents

Chapter 1

Introduction

1.1 Physics motivation

One motivation to study physics is to understand the fundamental laws of nature that rule the universe around us. For a long time, the fundamental questions about nature were the inspiration for mankind to keep looking for answers. One basic question of physics is "*what are the basic building blocks of matter?*" - how far have we advanced in this question? According to our current knowledge:

> *"Particle physics is at the heart of our understanding of the laws of nature. It is concerned with the fundamental constituents of the Universe, the elementary particles, and the interactions between them, the forces. Our current understanding is embodied in the Standard Model of particle physics, which provides a unified picture where the forces between particles are themselves described by the exchange of particles. Remarkably, the Standard Model provides a successful description of all current experimental data and represents one of the triumphs of modern physics."* **Modern Particle Physics, Mark Thomson** [1].

Thus far, the known elementary particles of nuclear matter are quarks and gluons. These particles are governed by the strong nuclear force and the interaction between quarks is mediated by gluons. Quarks and gluons have never been detected experimentally, due to colour confinement in Quantum Chromodynamics (QCD) [2, 3], the fundamental theory of the strong interaction. In ordinary nuclear matter, quarks and gluons are

confined into hadrons such as pions, kaons, protons, neutrons, etc. QCD predicts the existence of a phase transition of hadronic matter from a confined state to a deconfined phase, where hadrons lose their identity and dissociate into their elementary constituents, quarks and gluons. This new state of nuclear matter is known as Quark-Gluon Plasma (QGP) [4–7].

A QGP is expected to be formed when matter is at extreme high temperatures and densities. These extreme conditions can be achieved in two different scenarios: either at high net baryonic density inside the neutron stars [8] or in high-energy collisions in a laboratory such as the Relativistic Heavy Ion Collider (RHIC) [9] and Large Hadron Collider (LHC) [10], as the systems formed in such collisions are expected to reach very high temperatures. As part of the high-energy physics programmes at RHIC and LHC, the collisions of heavy ions[1] (AA) allow experiments to collect a large amount of data on the QGP to study the dynamics of the fundamental interactions (For one historical perspective and theoretical motivation, please see the review [11]). Such ultra-relativistic heavy-ion collisions are the only known tool that allows for the creation of hot QCD matter under controlled conditions and enables the investigation of the phase diagram of QCD in the laboratory.

In the following sections of this chapter, we will describe the general formalism for heavy-ions physics by introducing the QCD theory and discuss the concepts of QGP in sections 1.2 and 1.3, respectively. In section 1.4 we will introduce the physics terminology used in the field. Finally, we present two important signatures associated to the QGP formation in heavy-ion collisions: the nuclear modification factor and the anisotropic flow, described in sections 1.6 and 1.7, respectively.

1.2 Quantum Chromodynamics (QCD)

In particle physics, QCD is the fundamental theory that describes the strong interactions between quarks and gluons in the Standard Model (SM). QCD is a quantum field theory (QFT) classified as a non-Abelian theory represented by the gauge group $SU(3)_c$ [3]. The strong interaction is mediated by the gauge bosons known as gluons that carry the physical quantity responsible for the strong interaction, the colour charge. It can be

[1]The term “heavy ions” is used for heavy atomic nuclei (A).

one of three types: red, blue and green. The QCD theory is very similar to another QFT in the SM known as quantum electrodynamics (QED), which describes the interactions between charged particles and photons. In this theory, photons are the mediators of the interactions and do not carry electric charge, in contrast to QCD, in which the mediators - gluons - carry colour charge.

There are two fundamental phenomena in QCD: colour confinement and asymptotic freedom. Colour confinement is a property of the theory that states that quarks and gluons cannot exist as free particles in nature [12, 13], i.e., quarks are always bound into composite particles known as hadrons. These particles are without colour charge (or "colourless"), because the only allowed combination of colour charges is such that the resulting color is white [14]. Hadrons are classified as baryons, mesons and their antiparticles, which have opposite electric charge. Baryons are composed by three quarks and mesons by one quark (q) and one antiquark ($\bar{q}$), with the following notation: qqq (baryon) and q$\bar{q}$ (meson) with their antiparticles denoted by $\bar{q}\bar{q}\bar{q}$ and q$\bar{q}$, respectively. Asymptotic freedom is a property according to which very high-energy quarks and gluons behave as 'free particles' and interact weakly at very short distances (or large momentum transfers) [15] of the order the proton size of 1 fm [2]. These two phenomena are manifestations of nuclear matter in different regions of energy: confinement appears at low energies and asymptotic freedom appears at high energies.

Whenever a quark-antiquark pair (quark dipole, e.g. meson) interact and the the distance between them is increased, the energy stored in the colour field (or colour flux tube) between quark-antiquark progressively increases nutil it becomes energetically favorable to create a new quark-antiquark pair (q$\bar{q}$) from the vacuum, as we can see in Fig. 1.1. An effective QCD potential for the quark-antiquark interaction can be derived using lattice QCD results [16] between the quarks can be written as:

$$V_{QCD}(r) = -\frac{4}{3}\frac{\alpha_s \hbar c}{r} + \kappa r, \tag{1.1}$$

where α_s is the coupling strength, κ represents an effective interaction strength similar to a spring tension, $\hbar c$ is the Planck constant h divided by 2π times speed of light c and r is the distance between the quark and the antiquark. In Eq. (1.1), the first term

[2] The symbol fm stands for femtometer, which is a unit of measurement in the SI (International System of Units) and 1 fm = 10^{-15} m is also known as fermi.

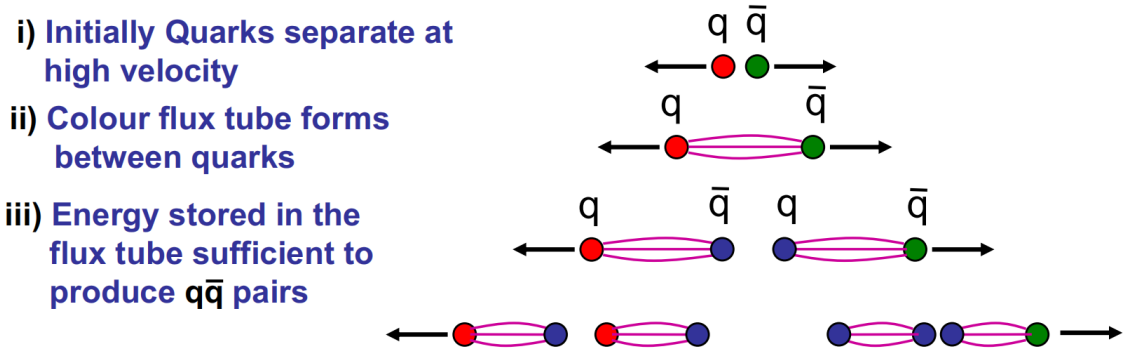

Figure 1.1: Quark dipole production at high energy. Figure adapted from the lecture *Handout 8 : Quantum Chromodynamics*, M.A. Thomson, Michaelmas 2009.

shows that, for small distances, e.g. for $r \ll 1$ fm, the effective QCD potential is like the electromagnetic potential ($V_{QED}(r) = \alpha/r$, where α is the fine structure constant and r is the distance between charged particles [1, 17]). The second term shows that if the distance r increases, a strong attraction appears to prevent the separation of the quark dipole. This term becomes the dominant one in the QCD potential at large distances and can be approximated to $V_{QCD}(r) \approx \kappa r$. The effective QCD potential can be seen in Fig. 1.2, where it is also compared to the QED potential.

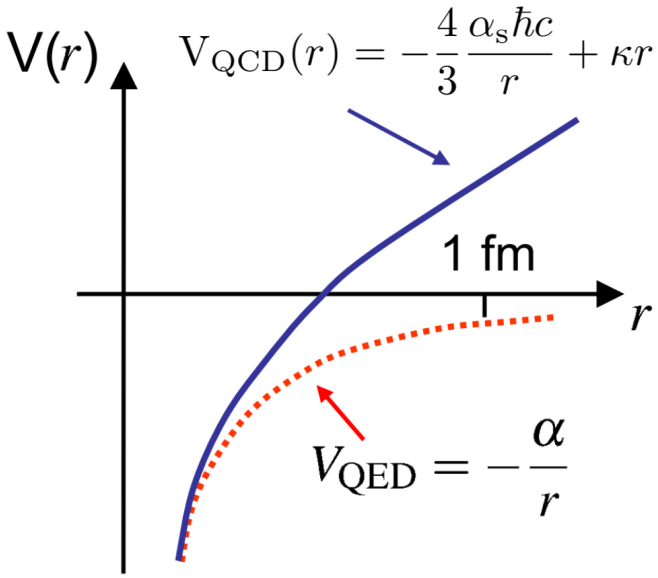

Figure 1.2: Effective QCD potential between a quark and an antiquark calculated using Lattice QCD [16]. Figure adapted from the lecture *Handout 8 : Quantum Chromodynamics*, M.A. Thomson, Michaelmas 2009

The coupling strength α_s depends on the momentum transfer Q of the interaction. To understand the behavior of the QCD coupling, is necessary to look at the complete Q^2 range to describe the strong interaction at short and long distances. Below we show the

first term of the expansion for the coupling strength $\alpha_s(Q^2)$ as a function of Q^2 according to ref. [18]:

$$\alpha_s(Q^2) \approx \frac{4\pi}{\beta_0 \ln(\frac{Q^2}{\Lambda_{QCD}})}, \tag{1.2}$$

where Q^2 is the momentum transfer, the term $\beta_0 = 11 - \frac{2}{3}n_f$ is the first one from the β-series [15, 19], where n_f is the number of quark flavours[3] active at the scale Q^2 and Λ_{QCD} is the energy scale of QCD at low-Q^2. The dependence of the coupling strength on Q^2 has been sketched in Fig. 1.3a and is based on experimental results [20]. At low-Q^2- of the order of $\Lambda_{QCD} \approx 200$ MeV [4] - the coupling strength $\alpha_s(Q^2)$ of QCD is in a region where the perturbative theory is not applicable and breaks down. This is the domain known as the non-perturbative regime. At low energy, i.e. at long distance R or low momentum transfer, quarks and gluons are confined into hadrons due to colour confinement and $\alpha_s(R)$ is large, as can be seen in Fig. 1.3b. On the other hand, at high-Q^2, $\alpha_s(Q^2)$ is small and ordinary matter made of protons and neutrons reaches a state of asymptotic freedom, where quarks and gluons behave as if they were quasi-free particles, i.e., they interact weakly inside the hadron.

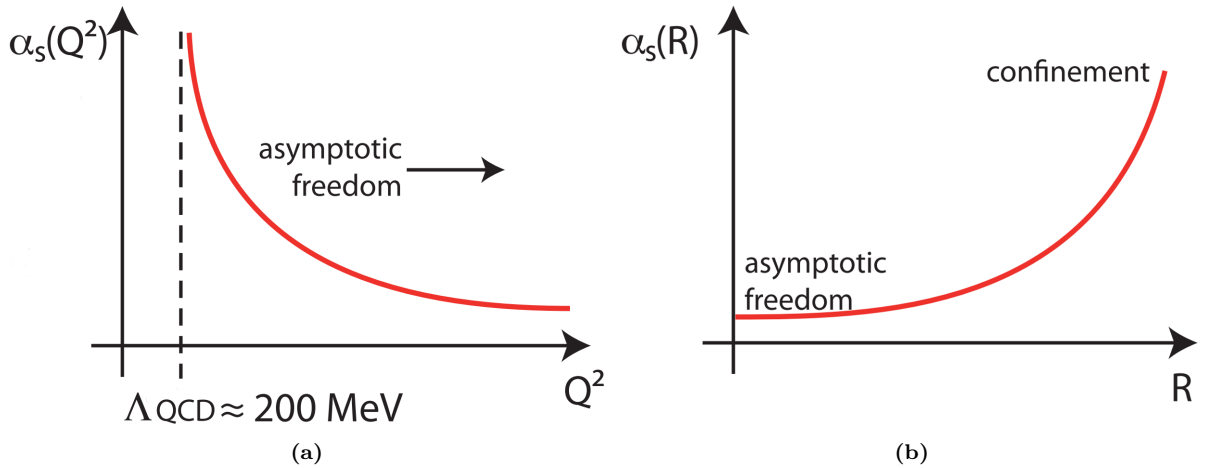

Figure 1.3: **(a)** The coupling strength $\alpha_s(Q^2)$ as a function Q^2 and **(b)** the coupling strength $\alpha_s(R)$ as a function the distance R. Figure taken from the lecture 1: *perturbative QCD*, Aude Gehrmann-De Ridder in AcademicTraining Lectures, CERN, May 2013.

[3] In the Standard Model, six types of quark flavours exist: up (u), down (d), strange (s), charm (c), bottom (b), top (t) and their antiquarks. For more information, see the Ref. [20].

[4] In physics, an electronvolt (eV) is an unit of energy define as the quantity of kinetic energy carried by one single electron when accelerated by one electric potential difference of one volt in vacuum. One million (M) of electronvolt is denoted by MeV. In this thesis, we also use the prefixes G = 10^9 and T = 10^{12}, to denoted by GeV and TeV.

Asymptotic freedom can be described by perturbative QCD because the expansion of the strong coupling does not diverge at high energies and can be approximated by a constant of the order of $\alpha_s = g_s/(4\pi) \ll 1$, where g_s is a gauge coupling parameter that appears in the Lagrangian density of QCD [3].

At high energies or high densities, ordinary matter starts to lose their identity and undergoes a phase transition to a QGP, where new degrees of freedom associated to quarks and gluons, broadly called 'partons', appear. In the next section, we will go into more detail regarding the Quark-Gluon Plasma phenomenon.

1.3 Quark-Gluon Plasma (QGP)

Ordinary matter is made up of atoms, which in turn are made up of electrons and nuclei, as represented schematically in Fig. 1.4 (a). Nuclei are also composite objects and are composed of 3 valence quarks each. While nuclear matter is very dense, the nucleons - protons and neutrons - still confine their constituents in hadrons and therefore quarks and gluons cannot traverse the nuclear volume freely. However, if nuclear matter were to increase significantly, hadronic boundaries would cease to be relevant and quarks and gluons would be free to roam inside this high-density environment. This is one of the potential ways to create a quark-gluon plasma, and it is thought that it might occur inside neutron stars.

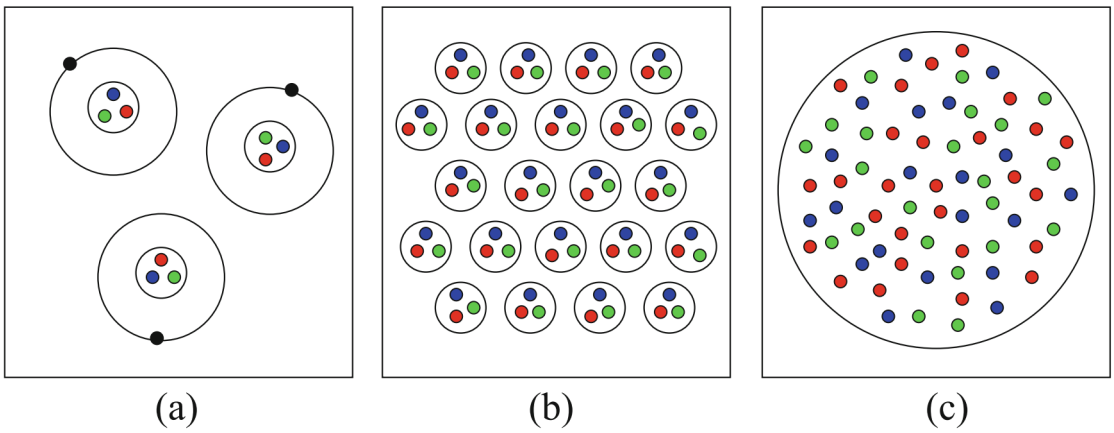

Figure 1.4: A schematic view of increasing density, from atomic **(a)** to nuclear **(b)** and then to quark matter **(c)**. Figure taken from [21].

Quark deconfinement can also occur at very high energy densities. In this case, it is not the baryonic density that drives the phase transition, but rather the large available energy

for particle-antiparticle creation. A schematic representation of the two ways of reaching the QGP phase can be seen in Fig. 1.5: while the neutron star limit is reached at $T \approx 0$, the high-energy limit is achieved in highly energetic events such as the big bang or high-energy collisions in the laboratory. At net baryonic densities of zero, calculations from Lattice QCD [22] show that the phase transition is a crossover, with a critical temperature (T_c) [5] in the range from 150 to 200 MeV. In heavy-ion collisions, we expect to obtain a QGP when the energy density achieves the estimated value of 1 GeV/fm^3 according to Ref. [24]. If converted to a temperature, this would correspond to a value that is of the order of 10^6 times the core temperature of the sun.

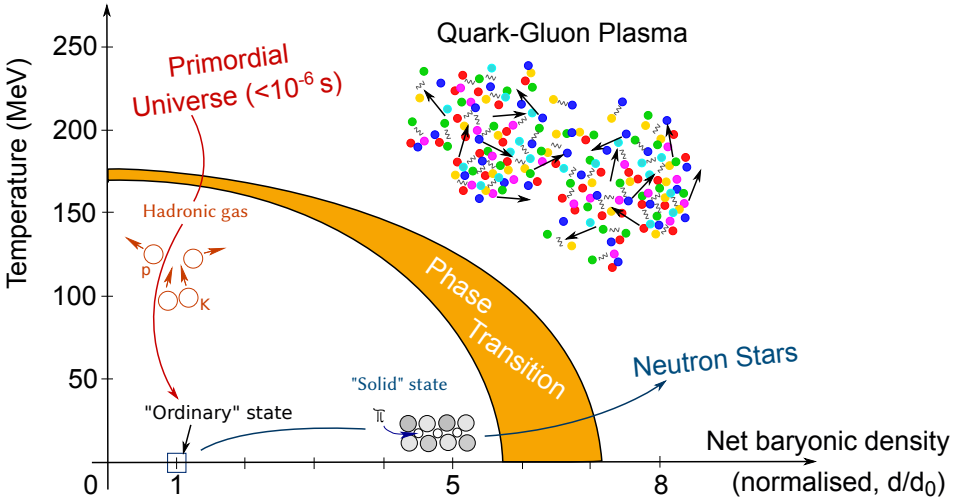

Figure 1.5: A schematic view of the phase diagram of QCD matter. Figure taken from [25].

While reaching a high net baryonic density in the laboratory is essentially impossible, high-energy events with net baryonic density close to zero can be done in the laboratory using particle accelerators and heavy-ion beams. This is what is done at RHIC and at the LHC, where heavy-ion programs exist to study the properties of the QGP and the phase transition to a deconfined medium and back.

The QGP phase lives about 10 fm/c (10^{-24} s) after the collision and cannot be observed directly. The many experiments set up at RHIC and at the LHC therefore have to search for indirect signatures of the QGP. To date, many signatures have been found. In this work, we will focus on anisotropic flow and the nuclear modification factor [11] and we will explain these concepts in Sections 1.6 and 1.7. Before we come to that, however, we will briefly describe the experimental efforts involving heavy-ion physics.

[5] This temperature is also known as Hagedorn temperature (T_H) [23].

1.4 Heavy-ion collision experiments

Relativistic heavy-ion colliders can be used to study the nuclear matter under extreme conditions by colliding two nuclei at velocities close to the speed of light (c). At RHIC, at the center-of-mass energy per nucleon pair $\sqrt{s_{\mathrm{NN}}} = 200$ GeV, the Lorentz factor is about $\gamma \approx 100$, meaning that uranium nuclei with a diameter of 14 fm are contracted to 0.1 fm in the beam direction with velocity of ≈ 0.99994c. At the LHC, at $\sqrt{s_{\mathrm{NN}}} = 2.76$ TeV, the Lorentz factor $\gamma \approx 1500$ contracts the nucleus to ≈ 0.01 fm in the beam direction with velocity of 0.9999997c. In these accelerators, interactions occur when two beams[6] moving in the opposite direction (in separate beam pipes) cross in some pre-determined position, which then corresponds to where detectors have to be set up to measure particles produced via beam-beam interactions.

The LHC complex is the world's largest and most powerful accelerator ever built and localized at CERN[7] [26] close to the border between France and Switzerland, near Geneva. The main accelerator ring at the LHC has a circumference of 27 kilometers and is located approximately 100m underground. The points in which beams are allowed to cross are where experiments are set up, including the four main experiments at the LHC, as can be seen in Fig. 1.6. Below we give a brief description and the main purpose of the four experiments at the LHC:

- **ALICE** (A Large Ion Collider Experiment) [27] is a general-purpose heavy-ion detector optimized to study the properties of matter at extreme densities and temperatures, i.e. the quark-gluon plasma that existed in the first microseconds after the *Big Bang*.

- **ATLAS** (A Toroidal LHC ApparatuS) [28] is a general-purpose particle physics detector designed to explore the physics of matter at an infinitely small scale, heavy-ion collisions and physics beyond the Standard Model. ATLAS was one of the two experiments at LHC that discovered the Higgs boson, a discovery announced on the 4^{th} of July 2012 [29].

[6] At the LHC, Pb beams are composed of almost 600 bunches and each bunch contains approximately 7.0×10^7 Lead ($^{208}\mathrm{Pb}^{82+}$) ions.

[7] The acronym CERN is derived from the French *Conseil européen pour la recherche nucléaire*, meaning 'European Organization for Nuclear Research'.

- **CMS** (Compact Muon Solenoid) [30] experiment is a general-purpose particle physics detector that aims to explore a large range of physics. The CMS collaboration performed the search for the Higgs boson, which led to an independent verification of the ATLAS results [31]. In addition, the CMS collaboration studies heavy-ion collisions and searches for evidence of physics beyond Standard Model, such as supersymmetry or extra dimensions.

- **LHCb** (Large Hadron Collider beauty) [32] the word 'beauty' refers to the bottom quark. This experiment is dedicated to precision measurements of heavy flavour physics and to search for indirect evidence of CP violation, which could be a probe for new physics beyond the Standard Model.

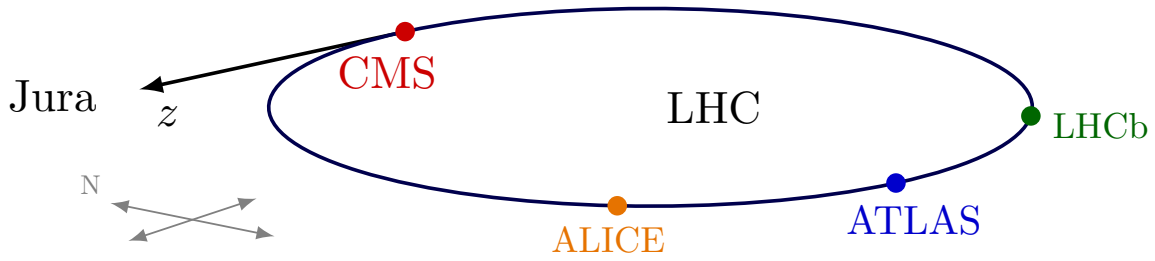

Figure 1.6: Schematic representation of the LHC ring layout with the experiments ALICE, ATLAS, CMS and LHCb located at the collision points. To guide the reader: Jura are mountains located north of the Western Alps. Figure adapted from CMS Wiki Pages.

All four experiments have already collected data during the data taking periods called 'Runs'. The first of these, Run 1, lasted from 2009 to 2013, while the second, Run 2, took place in the time frame between 2015 and 2018. At this time, the machine is in the second long shutdown (LS2) to perform important upgrades until the end of 2020, with Run 3 due to start at the beginning of 2021 [33]. In Tab. 1.1 we present a summary of which collision systems at which energies were measured by the experiments in Run 1 and Run 2.

In this work, we will focus on the Pb-Pb data collected at $\sqrt{s_{\mathrm{NN}}} = 2.76$ TeV, for which a very significant amount of information has already been published. The higher energy of 5.02 TeV and collision systems such as p-Pb are of course also extremely interesting but will be left for future studies.

Table 1.1: Collision systems measured by the LHC experiments during the LHC Run 1 and 2.

	Run 1 (2009-2013)			Run 2 (2015-2018)		
Energy	Collision system			Collision system		
$\sqrt{s_{\mathrm{NN}}}$ (TeV)	pp	p–Pb	Pb–Pb	pp	p–Pb	Pb–Pb
0.9	✓	-	-			
2.76	✓	-	✓			
5.02	-	✓	-	✓	✓	✓
7	✓	-	-			
8	✓	-	-			
8.16				-	✓	-
13				✓	-	-

1.4.1 Coordinate system and kinematic variables

Usually the experiments adopt a right-handed orthogonal Cartesian coordinate system [26] with its origin at the center of the detector, called a collision point (or interaction point), as described by the Fig. 1.7. The $\hat{z}$ direction is defined in the anticlockwise beam direction, the $\hat{x}$ direction points to the center of the LHC ring in the horizontal plane and finally, the $\hat{y}$ is defined as being perpendicular to the horizontal plane that contains the LHC ring.

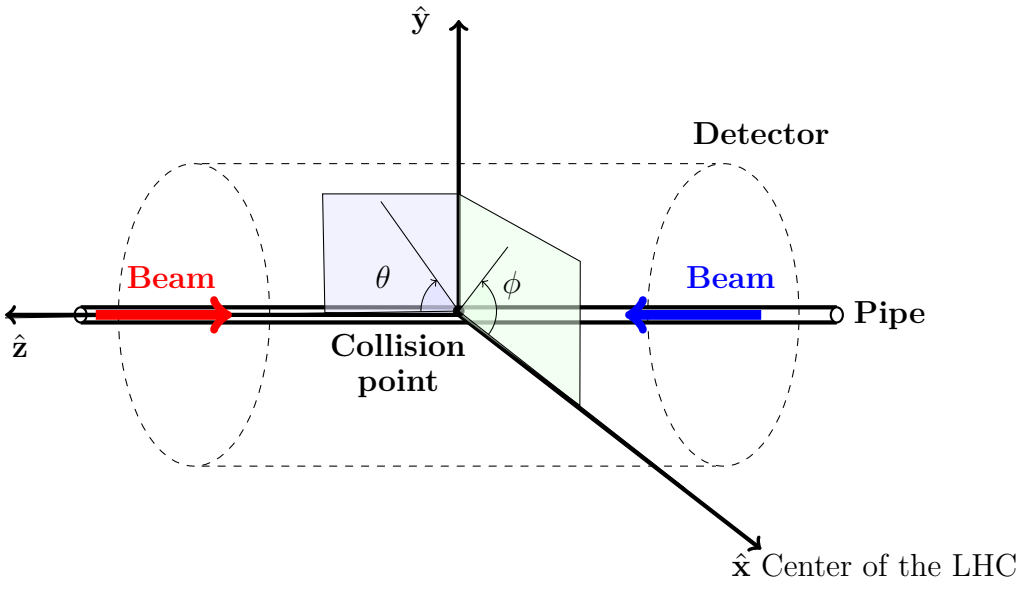

Figure 1.7: The coordinate system used by the collaborations at the LHC.

Once interactions take place, particles are produced in all directions in azimuth angle ϕ. It is because of this reason that a cylindrically symmetric detectors are preferred: they allow for maximum coverage in azimuth angle ϕ. Still, some particles cannot be observed in this manner because they are emitted at very large values of θ and are therefore close to being aligned with the beam direction. Overall, all experiments measure the products of the collision and reconstruct the interaction point, aiming at understanding how the primary interaction took place and how particles were produced.

The basic properties that need to be measured for each particle are contained in the four-vector $(E, \vec{p}_x, \vec{p}_y, \vec{p}_z)$, where E is the energy, $\vec{p}_x$, $\vec{p}_y$ and $\vec{p}_z$ are the momenta in the $\hat{x}$, $\hat{y}$ and $\hat{z}$ directions, respectively. It is especially interesting to separate the kinematic variables in the longitudinal and transverse planes, as described by the light green plane $x - y$ and the light purple plane $z - y$ in Fig. 1.7.

Since in high-energy collisions one is firmly in the domain of relativity, it is common to use a longitudinal variable called rapidity (y) (dimensionless quantity) instead of the velocity of the particle. Rapidity is defined as:

$$y = \frac{1}{2}\ln\left(\frac{E + p_z}{E - p_z}\right), \tag{1.3}$$

where E is the total energy of the particle, $E = \sqrt{m_0^2 + |\vec{p}\,|^2}$, m_0 is the mass in the rest frame (whose net momentum is zero) and $\vec{p}$ is the total momentum vector of the particle. The advantage of using rapidity is that this quantity is additive under Lorentz boosts along the z-direction, i.e., the rapidity distribution is boost-invariant under Lorentz transformations [34]. Moreover, is it only possible to calculate the rapidity when we know the particle mass, which has to be computed using the energy and momentum measured by the experiment. Having the entire energy-momentum information for a given particle is actually not trivial experimentally, which is why rapidity is typically only used when measuring particles of a specific species.

We can examine the rapidity for two cases: the first case is when the particle velocity is very small compared to the speed of light, which results in the particle rapidity being approximately equal to the velocity ($|\vec{v}|$), i.e. $y \approx |\vec{v}|$. The other case is that the particle velocity is very close to the speed of light, such that $E \gg m_0$, resulting in $E \approx |\vec{p}\,|$. Using this approximation, we can write the longitudinal momentum along the z-axis as $p_z = \vec{p} \cdot \hat{z}$, which as a function of E then becomes $p_z \approx E \cos\theta$, where θ is the polar angle

(or scattering angle) between the particle momentum vector and the beam direction, as can be seen in Fig. 1.7. Therefore, rapidity can be approximated by:

$$y \approx \frac{1}{2}\ln\left(\frac{E + E\cos\theta}{E - E\cos\theta}\right) = \frac{1}{2}\ln\left(\frac{1+\cos\theta}{1-\cos\theta}\right) \tag{1.4}$$

This approximation is known as a longitudinal variable called pseudorapidity, η, that can be written as:

$$\eta = -\ln\left[\tan\left(\frac{\theta}{2}\right)\right], \tag{1.5}$$

because the pseudorapidity does not dependent on the particle mass, we can compute η with just the angle θ for any charged particle that has been properly reconstructed in a tracking detector.

It is common to separate the pseudorapidity in two regions defined as midrapidity and forward. The midrapidity region is defined as the range $|\eta| < 0.5$ or $|\eta| < 0.8$ and is also called central region. It is very close to the fully transverse direction, i.e., at midrapidity particles produced at midrapidity are emitted with angles close to $\theta \approx \pi/2$. The forward region is broadly defined as the ranges $|\eta| \gtrsim 3$, such that particles emitted in the forward region are at small θ angles with respect to the beam direction.

In the transverse plane, the variable widely used is the transverse momentum (p_{T}) of a particle, which is defined as:

$$p_{\mathrm{T}} = \sqrt{p_x^2 + p_y^2}. \tag{1.6}$$

Since the original system had no transverse momentum to speak of, any momentum in the $x - y$ plane must be associated to the primary interaction by definition, making the transverse momentum, p_T, an especially important variable. In the literature, an important measurement is that of transverse momentum distributions, denoted as:

$$\frac{\mathrm{d}^2 N_{ch}}{\mathrm{d}y\mathrm{d}p_{\mathrm{T}}} = \frac{N_{ch}}{\Delta y \Delta p_{\mathrm{T}}} = f(p_{\mathrm{T}}), \tag{1.7}$$

where $\mathrm{d}y$, Δy and $\mathrm{d}p_{\mathrm{T}}$, Δp_{T} are the widths of the bins in rapidity and transverse momentum [35]. Transverse momentum distributions will be an important observable in this work when discussing the results coming from our simulations.

1.4.2 Basic concepts and definitions

To study heavy-ion collisions we first need to introduce the terminology of the field. In these collisions, heavy ions are extended objects and the geometry of the collision is directly related with the multiplicity of particles created in the interaction. It is common in heavy-ion physics to define the concept of collision centrality. Theoretically, centrality is defined using the impact parameter (b) that is the distance between the centers of the two colliding nuclei in the plane perpendicular to the beam direction. In Fig. 1.8(a), we describe the longitudinal view before the collision. In the longitudinal view, the full circles in the nuclei are participating nucleons that undergo one or more inelastic ('binary') collisions with nucleons of the other nucleus and the open circles are spectator nucleons that did not participate in AA collision. In the transverse view, the overlapping region of the two colliding nuclei forms an elliptic shape for non-central collisions in which $2R_A > \mathrm{b} > 0$, where R_A is the radius of the nucleus A. This overlap region is called 'interaction region'.

Because heavy-ion experiments cannot control the impact parameter of the collision directly, the overlap region can vary between the one observed for central collisions ($\mathrm{b} \to 0$) and for peripheral collisions ($\mathrm{b} \to 2R_A$).

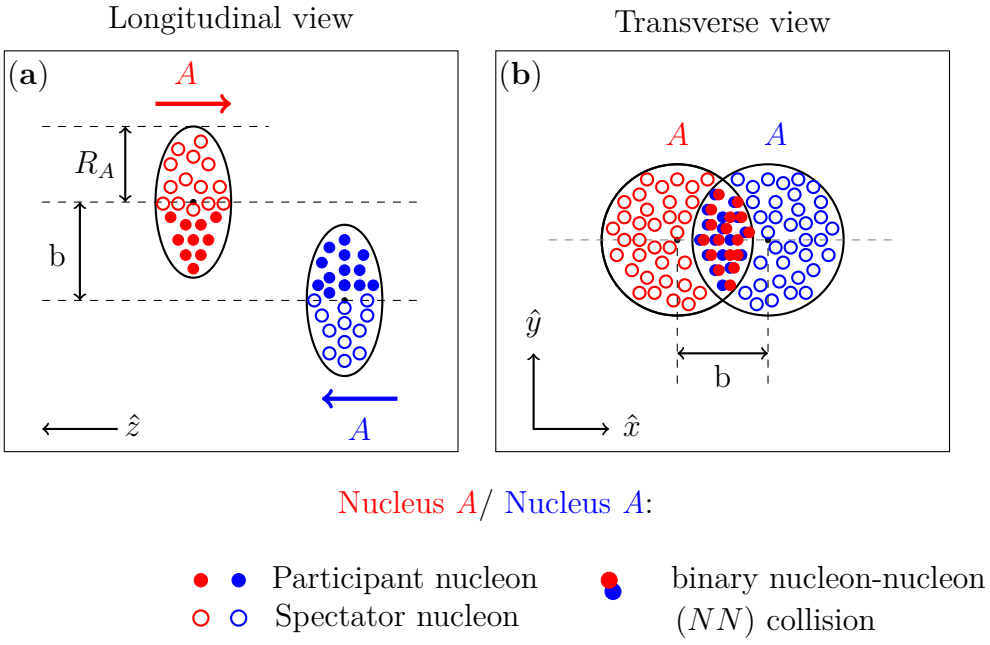

Figure 1.8: Initial geometry of the heavy-ion collision in the $z-y$ plane (left, not to scale) and in the $x-y$ plane (right).

Experimentally, the centrality of the collision can be estimated by measuring the charged-particle multiplicity $N_{\rm ch}$, given that the average multiplicity is a monotonic function of b, both at midrapidity and forward rapidity. Centrality is usually quantified using fractions of the geometrical cross-section, given by $\pi \mathrm{b}^2/\pi(2R_A)^2$, i.e., in central collisions more particles are produced compared to in peripheral collisions. As we know, the impact parameter, the number of participating nucleons (N_{part}) and number of binary inelastic collisions (N_{coll}) cannot be measured by the experiments. Typically, the distributions $\mathrm{d}N_{\rm events}/\mathrm{d}N_{\rm ch}$ and/or $\mathrm{d}\sigma/\mathrm{d}N_{\rm ch}$ can be used to estimate $\langle N_{\rm part}\rangle$ and $\langle N_{\rm coll}\rangle$ quantities using the Glauber model [36, 37].

Phenomenologically, we know that the total particle production measured by the experiments is correlated with $N_{\rm part}$ and $N_{\rm coll}$, where $N_{\rm part}$ is more closely related with soft processes (low momentum transfer or low-$p_{\rm T}$) and $N_{\rm coll}$ is more closely related to hard processes (high momentum transfer or high-$p_{\rm T}$). These quantities can be related to the impact parameter via the nuclear geometry in a Glauber calculation [37], as can be seen in Fig. 1.9.

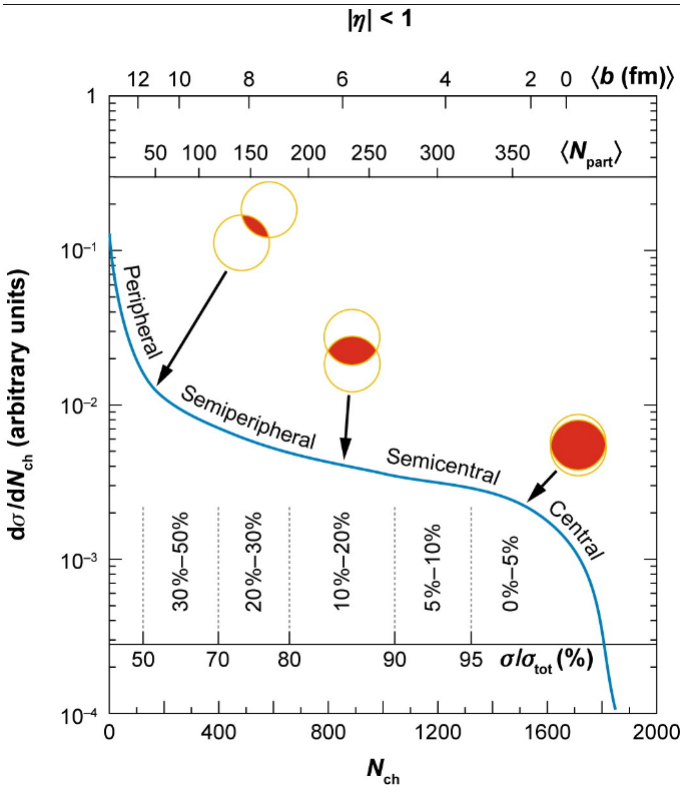

Figure 1.9: Charged-particle multiplicity distribution as a function of $N_{\rm ch}$ with the impact parameter(b) and $\langle N_{part}\rangle$ calculated by the Glauber Model. Taken from [37].

A systematic comparison of the measured charged-particle multiplicity distribution $\mathrm{d}N_{\mathrm{events}}/\mathrm{d}N_{\mathrm{ch}}$ at $|\eta| < 1$ midrapidity and the distribution simulated using the Glauber model enables the extraction of mean values of $\langle N_{\mathrm{part}} \rangle$ and $\langle N_{\mathrm{coll}} \rangle$ for each event centrality class. Centrality is widely expressed and quantified as a percentage of the total nuclear interaction cross section (σ_{tot}) [37]. Mathematically, this means that the centrality percentile of AA collisions is defined in terms of a fraction of the total integral of $\mathrm{d}N_{\mathrm{events}}/\mathrm{d}N_{\mathrm{ch}}$, with the integration evaluated from large to small values of N_{ch}. For example, the event class corresponding to very central collisions is denoted as $0-5\%$ and has N_{ch} boundaries defined as n_0 and n_5 given by:

$$\frac{\int_{\infty}^{n_0} \frac{\mathrm{d}N_{\mathrm{events}}}{\mathrm{d}N_{\mathrm{ch}}} \mathrm{d}N_{\mathrm{ch}}}{\int_{\infty}^{0} \frac{\mathrm{d}N_{\mathrm{events}}}{\mathrm{d}N_{\mathrm{ch}}} \mathrm{d}N_{\mathrm{ch}}} = 0 \qquad \text{and} \qquad \frac{\int_{\infty}^{n_5} \frac{\mathrm{d}N_{\mathrm{events}}}{\mathrm{d}N_{\mathrm{ch}}} \mathrm{d}N_{\mathrm{ch}}}{\int_{\infty}^{0} \frac{\mathrm{d}N_{\mathrm{events}}}{\mathrm{d}N_{\mathrm{ch}}} \mathrm{d}N_{\mathrm{ch}}} = 0.05. \tag{1.8}$$

The other centrality classes are calculated in the same way, with typical centrality bin widths being 5%, 10% or 20%, depending on the available data sample being considered for analysis. In this work, we use the same method of centrality selection adopted by the ALICE collaboration [38] to do a fair comparison between our simulation and the real data analysis. To estimate the centrality classes, the ALICE collaboration employs the charged-particle multiplicities measured at forward rapidities of $-3.7 < \eta < -1.7$ and $2.8 < \eta < 5.1$, measured using the VZERO-C and VZERO-A detectors, respectively, covering the full azimuthal angle (ϕ). For more details about the centrality determination used in this thesis, please see the Sec. 2.6.

1.5 Evolution of a heavy-ion collision

In collisions of large nuclei we expect to create a hot and dense QCD matter sample that will expand and cool down, as can be seen in Fig. 1.10. Basically, this space-time diagram describes the system evolution at different times before and after the collision at t = 0 fm/c. In the collision we reach the extreme densities and temperatures by depositing a large amount of energy (kinematic energy from the nuclei) in a small region of space in a short period of time.

The system evolution is broadly believed to take place in the following way:

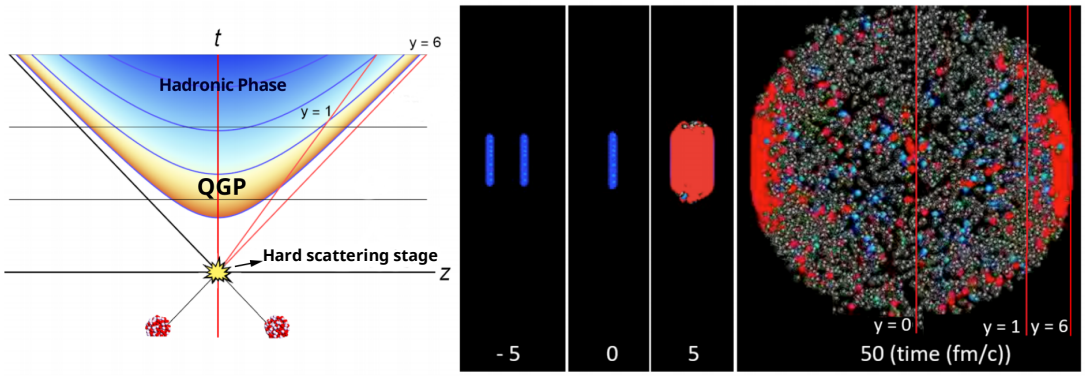

Figure 1.10: (**Left**) Space-time picture of the system evolution of the nuclear matter created in heavy-ion collisions. (**Right**) shows snapshots of a central Pb–Pb collision at $\sqrt{s_{\mathrm{NN}}} = 2.76$ TeV at different times. Figure adapted from [39].

- **Hard scattering stage:** The interaction begins at t = 0 fm/c with hard scatterings between quarks and gluons. At this stage, the relevant degrees of freedom are already partonic, but there is no local equilibrium of any kind.

- **The QGP:** local equilibration is reached after about 1 fm/c (the so-called 'thermalization time'). It is at this time in which one can think of the QGP being formed as such. The system continues to evolve until quarks and gluons combine into hadrons, a process called hadronization.

- **Hadronic Phase:** At this point, the system is in the stage known as hadronic phase, in which hadrons can still undergo inelastic and elastic scatterings. These interactions cease when the chemical and kinetic 'freeze-out' is reached.

It is only after all of this has taken place that experiments can measure the final products of the collision. Therefore, a direct observation of the QGP phase is impossible. The only way to confirm that a QGP was indeed formed is via the study of final-state observables. The main signatures of the QGP are: *strangeness enhancement* [40] is the enhanced production of strange quarks in the QGP, *jet quenching* [41] is the energy loss suffered by high-momentum particles traversing the color-deconfined medium and *anisotropic flow* [42, 43] of the final-state particles is a clear experimental signature of collective behavior in heavy-ion collisions. Given that in this work we are going to focus on observables associated to jet quenching and collective flow in the next sections, we will discuss these two phenomena in the next two sections.

1.6 Jet quenching

In high-energy physics, jets are defined as cluster of particles with relatively high p_{T} that are rather close in phase space, essentially looking like a 'spray' of particles in one direction. Jets are produced whenever a high momentum parton coming from a hard scattering 'fragments' into other partons, eventually producing colorless hadrons that are correlated to one another. In heavy-ion collisions, high-momentum partons coming from hard scatterings will travel through the QCD matter and will lose energy due to multiple interactions with the QGP medium before turning into hadrons. This process is known as jet quenching [44] and serves as an important phenomenon when studying the properties of the QCD matter that absorbed the energy of the original high-momentum parton. This difference is particularly evident when comparing measurements performed in Pb-Pb collisions, where the QGP is expected to be formed, to measurements done in pp collisions, as can be seen in Fig. 1.11: it is only in the presence of a QGP that jets will be absorbed and the usual dijet structure that is expected to be formed due to a high-momentum-transfer interaction will disappear.

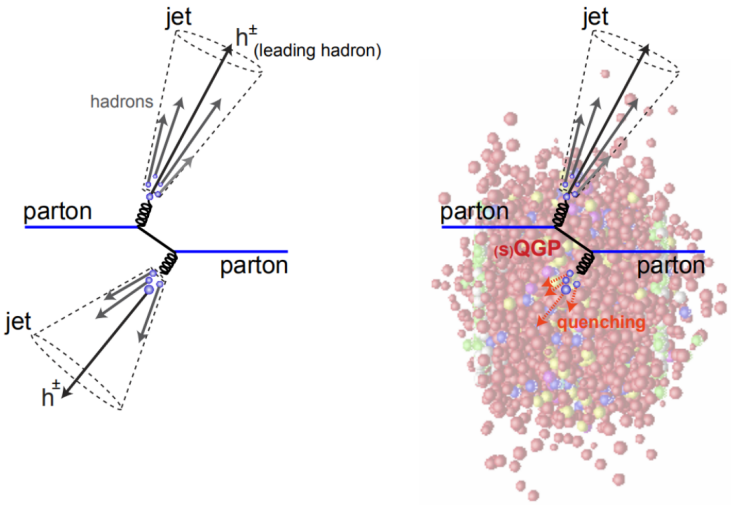

Figure 1.11: Sketch to describe jet quenching phenomenon in the presence of QCD medium. (**Left**) Jet production due to hard partonic scattering in pp collisions at high-p_{T} (no QGP) and (**Right**) Jets created in heavy-ion collisions travelling through the QGP medium lose a significant fraction of their energy. Figure adapted from [25].

This effect was first observed in central Au–Au collisions by the STAR collaboration at RHIC using the two-particle correlation technique [45] in azimuthal angle, as shown in Fig. 1.12. This technique allows for the search of correlations between the final-state particles by testing how particles are laid out with respect to a reference particle called

'trigger particle'. The particles that are studied with respect to the trigger particle are called 'associated particles'[8]. If the commonly expected dijet structure is present, there should be an accumulation of particles close in azimuth, i.e. $\Delta\phi$ close to zero, and also in the away-side, i.e. $\Delta\phi$ close to π, due to momentum conservation. The results by the STAR collaboration in central Au–Au collisions demonstrate a strong suppression of the away-side particle yield, while central d+Au and pp collisions do not show this effect, as seen in Fig. 1.12. This is an indication that in these small collision systems do not form a high-density medium that quenches outgoing partons.

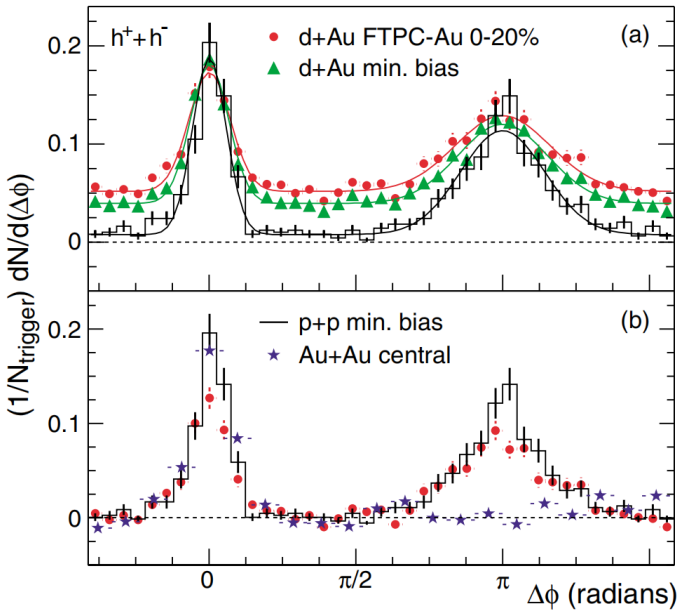

Figure 1.12: Two-particle correlation function (C($\Delta\phi$)) measured by the STAR collaboration at $\sqrt{s_{\rm NN}}$ = 200 GeV in Au–Au central collision (0 − 20%) compared with central d+Au and pp collisions (minimum bias). In this analysis was accepted only particles within $|\eta| < 0.7$. The trigger particles are selected in the $p_{\rm T}$ range $4 < p_{\rm T}^{\rm trigger}$ (GeV/c) < 6 with the number of trigger particles $N_{\rm trigger}$, where each trigger particle is correlated with all associated particles for the same event in the $p_{\rm T}$ range $2 < p_{\rm T}^{\rm assoc}$ (GeV/c) $< p_{\rm T}^{\rm trigger}$. Figure taken from [46].

There are many ways of studying the loss of high-momentum particles in heavy-ion collisions. One of the simplest ways is to understand how many high-momentum particles are observed with respect to a specific expectation: this is what is done in the observable called nuclear modification factor, or R_{AA}, which is defined in the next section.

1.6.1 Nuclear modification factor

The nuclear modification factor R_{AA} is defined as the ratio of the $p_{\rm T}$ spectrum of charged particles ($\mathrm{d}N_{\rm ch}/\mathrm{d}y\mathrm{d}p_{\rm T}$) in AA collisions and the $p_{\rm T}$ spectrum in pp collisions

[8]More details on this method will be given in Sec. 1.6.2

(reference) scaled by the average number of binary nucleon-nucleon (NN) collisions $\langle N_{\rm coll}\rangle$ as a function of $p_{\rm T}$ and can be written as:

$$R_{AA}(p_{\rm T}) = \frac{{\rm d}^2N_{\rm ch}^{AA}/{\rm d}y{\rm d}p_{\rm T}}{\langle N_{\rm coll}\rangle {\rm d}^2N_{\rm ch}^{\rm pp}/{\rm d}y{\rm d}p_{\rm T}} = \frac{{\rm d}^2N_{\rm ch}^{AA}/{\rm d}y{\rm d}p_{\rm T}}{\langle T_{AA}\rangle {\rm d}^2\sigma_{\rm inel}^{\rm pp}/{\rm d}y{\rm d}p_{\rm T}}, \tag{1.9}$$

where $N_{\rm ch}^{AA}$ and $N_{\rm ch}^{\rm pp}$ are the charged-particle yields in AA and pp collisions, respectively, and $\sigma_{\rm inel}^{\rm pp}$ is the inelastic cross section in pp collisions. The scaling is done with the average nuclear overlap function, $\langle T_{\rm AA}\rangle = \langle N_{\rm coll}\rangle/\sigma_{\rm inel}^{\rm pp}$, with the collision centrality dependence estimated using the Glauber model.

The R_{AA} can be interpreted and classified as:

$$R_{AA} = \frac{\text{“QCD medium”}}{\langle\text{scale}\rangle\text{“QCD vacuum”}} = \begin{cases} R_{AA} = 1 & \text{no nuclear medium effect,} \\ R_{AA} < 1 & \text{suppression.} \end{cases} \tag{1.10}$$

The case in which R_{AA} is equal to unity is representative of the absence of nuclear effects, i.e., AA collisions can be considered as a superposition of independent pp collisions (e.g. the $R_{AA} \approx 1$ measured at RHIC and LHC for photons [47, 48] and electroweak bosons ($\rm W^{\pm}$ and $\rm Z^0$) measured at LHC [49, 50]). On the other hand, R_{AA} less than unity is expected if the yield measured in AA collision is modified when high-$p_{\rm T}$ particles undergo interactions in a hot and dense medium.

Several measurements of the R_{AA} at RHIC and at the LHC have shown that $R_{AA} \ll 1$, suggesting a strong nuclear medium effect in AA collisions. At RHIC energies of $\sqrt{s_{\rm NN}}$ = 130 GeV and 200 GeV, the yields of charged hadrons [51, 52] or neutral pions [53] measured in central Au–Au collisions were found to exhibit a strong suppression with a factor of about 5 in the $p_{\rm T}$ range of 5 – 25 GeV/c, again an indication of strong nuclear medium effects.

The R_{AA} measurements for charged-particles at the LHC [54–57] have indicated that in central Pb–Pb collisions at $\sqrt{s_{\rm NN}}$ = 2.76 TeV the yield are suppressed by a factor of about 7 in the $p_{\rm T}$ range of 6 – 7 GeV/c. For higher $p_{\rm T}$, the suppression decreases, but the magnitude is still significant: it is a factor of about 2 for the $p_{\rm T}$ range of 30 – 150 GeV/c. Below in Fig. 1.13 we show the R_{AA} as a function $p_{\rm T}$ measured by the

ALICE collaboration in central $(0-5\%)$ and peripheral $(70-80\%)$ Pb–Pb collisions at $\sqrt{s_{\rm NN}} = 2.76$ TeV of charged-particles in the $|\eta| < 0.8$.

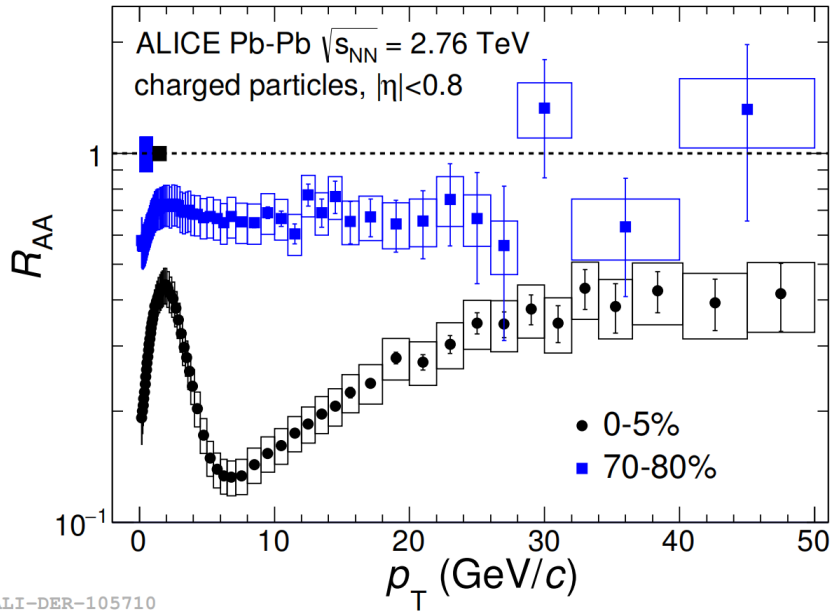

Figure 1.13: Nuclear modification factor R_{AA} in Pb–Pb collisions at $\sqrt{s_{\rm NN}} = 2.76$ TeV for charged particles at midrapidity ($|\eta| < 0.8$) in two centrality classes $0-5\%$ and $70-80\%$ measured by the ALICE collaboration. The boxes around the data points are the systematic uncertainties. The overall normalization uncertainties for the R_{AA} are shown as the black and blue boxes around unity for both centralities. Taken from [55].

The ALICE results for R_{AA} shows a clear centrality dependence from central to peripheral in Pb–Pb collisions. The R_{AA} for central collisions $(0-5\%)$ reaches a minimum of approximately 0.14 at 6 – 7 GeV/c. For intermediate-$p_{\rm T}$ we can see a maximum value of R_{AA} at $p_{\rm T} = 2$ GeV/c with a strong $p_{\rm T}$ dependence. In peripheral collisions, the R_{AA} does not show a significant $p_{\rm T}$ dependence and is of about 0.7 for $p_{\rm T} > 2$ GeV/c.

1.6.2 Two-particle angular correlations

The two-particle correlation (2PC) method is widely used to investigate the different physics mechanisms associated to particle production in pp, p–Pb and Pb–Pb collisions [58–60]. Basically, the correlation function is a distribution in relative pseudorapidity $\Delta\eta = |\eta_{\rm trigger} - \eta_{\rm assoc}|$ and in relative azimuthal angle $\Delta\phi = |\phi_{\rm trigger} - \phi_{\rm assoc}|$ phase space $(\Delta\phi - \Delta\eta)$ between the trigger and associated particles in the same event. The correction function C($\Delta\phi$, $\Delta\eta$) is normalized dividing by the number of trigger particles ($N_{\rm trig}$) found

in all events, that can be more than one trigger particle per event and to obtain the C($\Delta\phi$, $\Delta\eta$) [45] that can be written as:

$$C(\Delta\phi, \Delta\eta) = \frac{1}{N_{trigg}} \frac{d^2N^{pair}}{d(\Delta\phi)d(\Delta\eta)}, \tag{1.11}$$

where N^{pair} is the total number of correlated particle pairs. A thorough study of this correlation function enables a better understanding of several aspects of particle production, such as jet fragmentation and collective behaviour. Some basic concepts need to be defined in order to set the stage for the method to be explained. To calculate the correlation between the trigger and associated particles, the trigger particle is usually chosen with a high momentum so that it is likely related to the direction of a jet. Associated particles of a relatively lower momentum are then chosen and their layout in phase space with respect to the trigger particle is studied on a statistical basis.

The traditional procedure to construct the two-particle correlation function are established in [60, 61]. We are going to illustrate how we calculate the correlation function applying this method to events generated by the Monte Carlo (MC) simulations (e.g. PYTHIA/Angantyr for heavy-ion collisions [62, 63]). First, we need to apply some cuts to events to be a fair comparison with experimental conditions. In pseudorapidity η to select only particles in the range $|\eta| < 2.5$, because particles with $|\eta| > 2.5$ are emitted close to the beam direction, i.e. with the momentum making an angle $\theta \lesssim \pi/18$ with respect to the beam direction that are not observed by the detectors. This technique makes the correlation between the trigger and associated particles within $|\eta| < 2.5$ with your respective p_T ranges. The correlation function corrected $C_{correct}$ is given by:

$$C_{correct}(\Delta\phi, \Delta\eta) = \frac{C_{same}(\Delta\phi, \Delta\eta)}{\alpha \times C_{mix}(\Delta\phi, \Delta\eta)}, \tag{1.12}$$

where the correlation functions: $C_{same}(\Delta\phi, \Delta\eta)$ is calculated with the pair in the same event and $C_{mix}(\Delta\phi, \Delta\eta)$ is calculated using particles from different events by using the 'mixed event' technique. This technique is used to correct the limited pair acceptance, in order to do the same analysis performed by experiments. Theses correlations functions are defined as:

$$C_{same}(\Delta\phi, \Delta\eta) = \frac{1}{N_{trig}} \frac{d^2N^{pair}}{d(\Delta\phi)d(\Delta\eta)} \tag{1.13}$$

and

$$C_{mix}(\Delta\phi, \Delta\eta) = \frac{d^2N^{mix}}{d(\Delta\phi)d(\Delta\eta)}. \quad (1.14)$$

In Eq. (1.12) the $C_{mix}(\Delta\phi, \Delta\eta)$ is normalized by α to be unity at $\Delta\eta = 0$, meaning that all particles with the same η value will always be accepted by the cut $|\eta| < 2.5$, otherwise some pairs will not be accepted due to cut in η, e.g. the η value for the trigger and associated particles can be $\eta_{trigger} = 2$ and $\eta_{assoc} = 1$, $\Delta\eta = 1$ (pair accepted in $|\eta| < 2.5$) or $\eta_{trigger} = -2$ and $\eta_{assoc} = -3$, $\Delta\eta = 1$ (the associated particle is not accepted in $|\eta| < 2.5$). We calculate the correlation functions $C_{same}(\Delta\phi, \Delta\eta)$ and $C_{mix}(\Delta\phi, \Delta\eta)$ with events generated by the PYTHIA/Angantyr model [62, 63] in Pb–Pb collisions at $\sqrt{s_{NN}} = 2.76$ TeV, as can be seen in Fig. 1.14. The correlation functions 'same' and 'mix' were calculated for the p_T ranges of $2 < p_T^{trigger}$ (GeV/c) < 10 and $2 < p_T^{assoc}$ (GeV/c) < 4, where the trigger and associated particles are accepted in $|\eta| < 2.5$ (with $|\Delta\eta| < 5$) and in full azimuthal angle range.

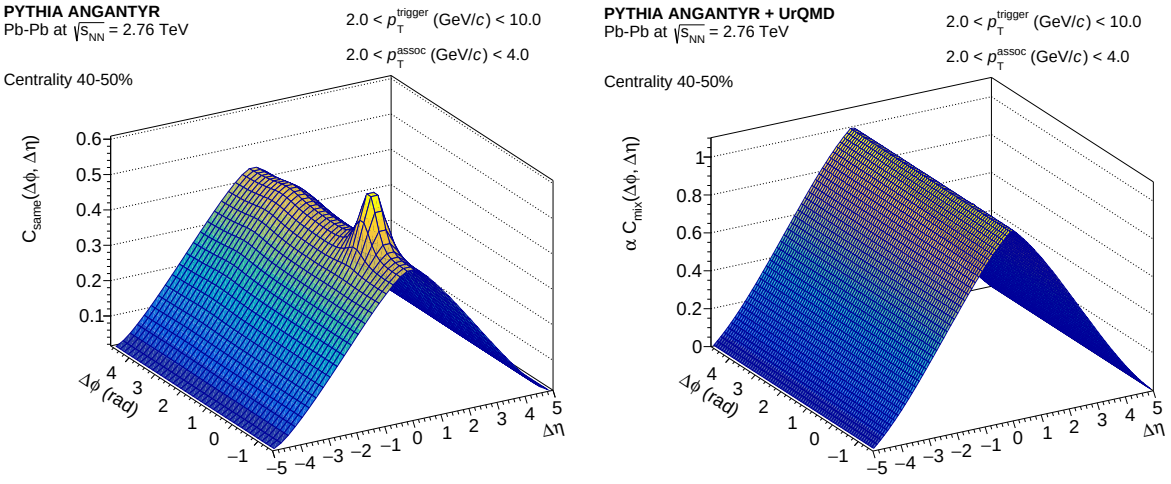

(a) **(b)**

Figure 1.14: The correlation functions same $C_{same}(\Delta\phi, \Delta\eta)$ (**a**) and mix $\alpha C_{mix}(\Delta\phi, \Delta\eta)$ (**b**) (normalized by α) calculated for $2.0 < p_T^{trigger}$ (GeV/c) < 10.0 and $2.0 < p_T^{assoc}$ (GeV/c) < 4.0 for events generated by PYTHIA/Angantyr in Pb–Pb collisions at $\sqrt{s_{NN}} = 2.76$ TeV, in the event centrality of $40 - 50\%$.

The $C_{same}(\Delta\phi, \Delta\eta)$ and $C_{mix}(\Delta\phi, \Delta\eta)$ were used to compute the correlation function correct $C_{correct}(\Delta\phi, \Delta\eta)$ represented by the Eq. (1.12) and showed in Fig. 1.15. The $C_{correct}(\Delta\phi, \Delta\eta)$ shows the correlations between the particles in the $\Delta\phi - \Delta\eta$, where we can observe a jet correlations localized around $\Delta\phi = 0$ and $\Delta\eta = 0$, named as near-side jet peak, that contain the pairs of trigger and associated particles from the fragmentation

of the same jet, and a structure localized around $\Delta\phi = \pi$ and extended in $\Delta\eta$ range, named as away-side jet peak due to the momentum conservation of jets ("back-to-back")[9].

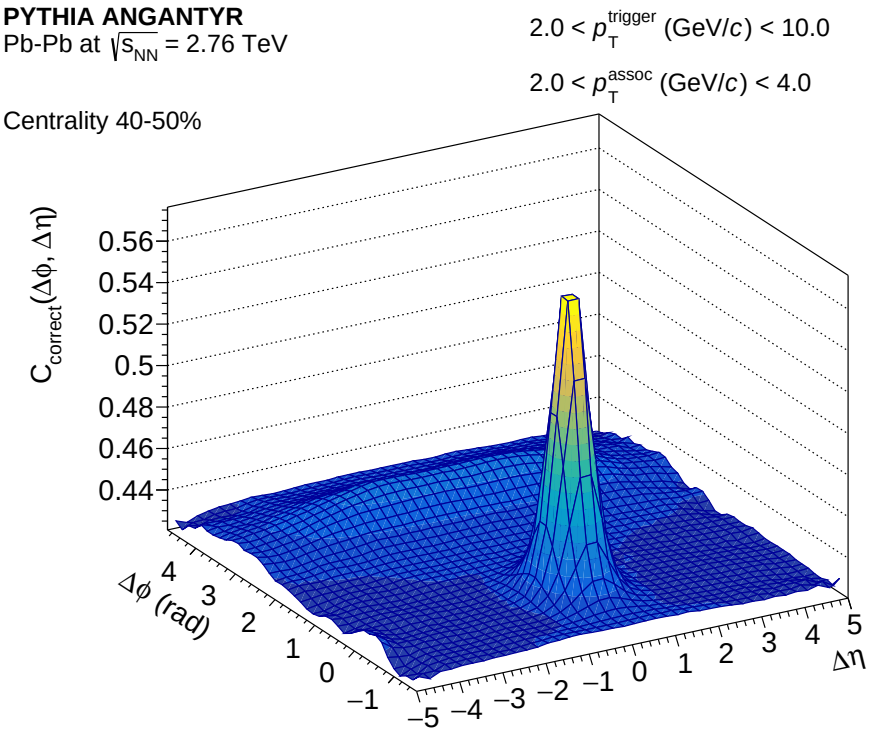

Figure 1.15: The correlation function correct $C_{\text{correct}}(\Delta\phi, \Delta\eta)$ calculated for $2.0 < p_{\text{T}}^{\text{trigger}}$ (GeV/c) < 10.0 and $2.0 < p_{\text{T}}^{\text{assoc}}$ (GeV/c) < 4.0 for events generated by PYTHIA/Angantyr in Pb–Pb collisions at $\sqrt{s_{\text{NN}}} = 2.76$ TeV.

In order to study in more details the $C_{\text{correct}}(\Delta\phi, \Delta\eta)$ is common to do the projection of $C_{\text{correct}}(\Delta\phi, \Delta\eta)$ in $\Delta\phi$, as can be seen in Fig. 1.16. In this figure we show the correlation function projected $C(\Delta\phi)$ in $|\Delta\eta| < 1.0$ for events generated by PYTHIA/Angantyr in Pb–Pb collisions at $\sqrt{s_{\text{NN}}} = 2.76$ TeV, with the p_{T} ranges of $2 < p_{\text{T}}^{\text{trigger}}$ (GeV/c) < 10 and $2 < p_{\text{T}}^{\text{assoc}}$ (GeV/c) < 4, where we highlight the near-side peak jet (light red), away-side jet (light green) and underlying event (UE) (light blue) that is classified as background.

Using the 2PC in heavy-ion experiments beyond the near-side and away-side also can be observed the structures around $\Delta\phi = 0$ and $\Delta\phi = \pi$ which extends for a long $\Delta\eta$ range, known as the "double-ridge". These large structures can be associated with collective expansion of a strongly interacting matter produced in non-central AA collisions quantified by the elliptic flow coefficient, v_2 [64]. In Fig. 1.17, we show the CMS results for two-particle correlation function measured in Pb–Pb collisions at $\sqrt{s_{\text{NN}}} = 2.76$ TeV,

[9] In the two-particle correlations analysis a widely adopted convention to divide the phase space region in two parts, one part for $\Delta\phi < \pi/2$ (near-side) and another part for $\Delta\phi > \pi/2$ (away-side).

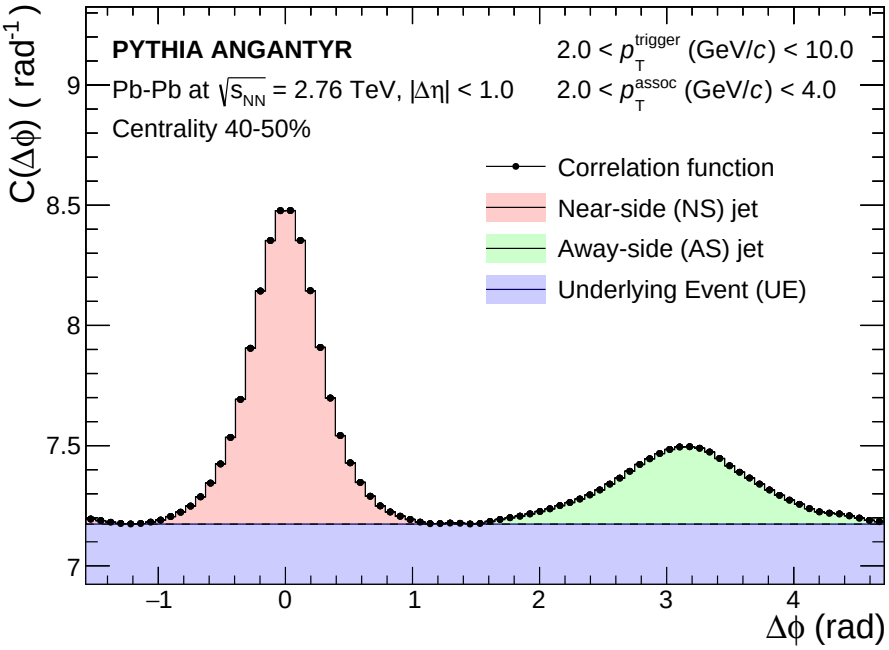

Figure 1.16: Correlation function projected in $\Delta\phi$ for events generated by PYTHIA/ Angantyr in Pb–Pb collisions at $\sqrt{s_{\rm NN}} = 2.76$ TeV and for the event centrality of $40-50\%$.

for the pair of charged-particles with the track multiplicity in the range of $220 \leq N_{\rm trk}^{\rm offline} \leq 260$ that is equivalent to in average to the centrality percentile of approximately 60% for the $p_{\rm T}$ ranges $1 < p_{\rm T}^{\rm trigger}\ ({\rm GeV}/c) < 3$ and $1 < p_{\rm T}^{\rm assoc}\ ({\rm GeV}/c) < 3$.

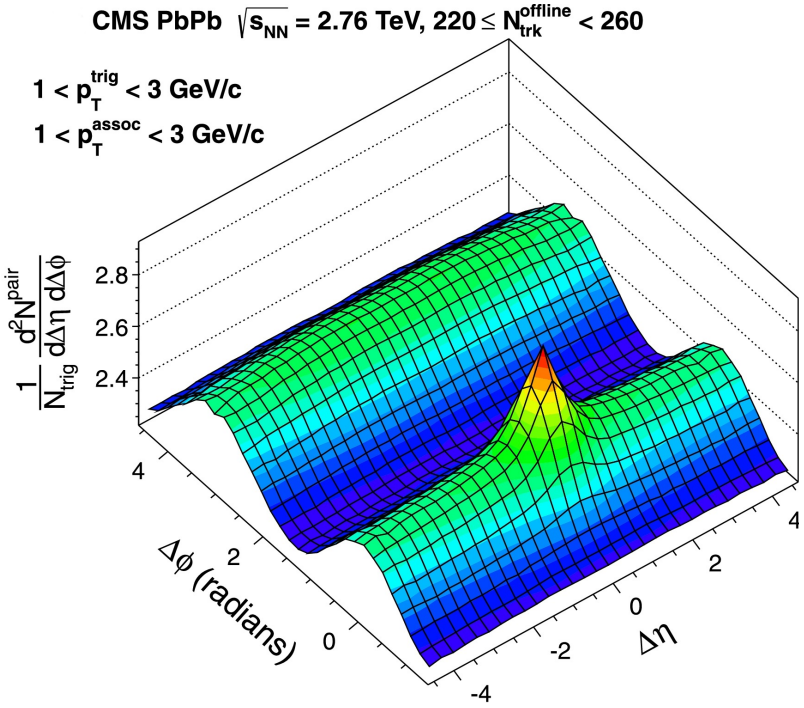

Figure 1.17: Two-particle correlation function measured by the CMS collaboration in Pb–Pb collisions at $\sqrt{s_{\rm NN}} = 2.76$ TeV for charged-particles within $220 \leq N_{\rm trk}^{\rm offline} \leq < 260$ multiplicity bin that corresponds to an average to centrality percentile of approximately 60%. Taken from [59].

In the CMS results in Fig. 1.17 show beyond the near-side and away-side jets, also is possible to see a clear long range ridge-like structure at $\Delta\phi = 0$ (near-side region) and $\Delta\phi = \pi$ (away-side region) extending in full $\Delta\eta$ range, the double-ridge. The double-ridge also was observed in different collision energies and collision systems (AA collisions) [60, 61, 65, 66]. The ridge-like structure was also observed recently in small system, for high-multiplicity in pp (at $\sqrt{s} = 7$ TeV) [67] and p–Pb (at $\sqrt{s_{\rm NN}} = 5.02$ TeV) [59, 68, 69] collisions, this unexpected long range correlation is not yet understood. In non-central AA collisions, the double-ridge is describe by the component $\cos(2\Delta\phi)$ azimuthal correlation, with origin assigned to the anisotropic expansion of the medium created in heavy-ion collisions, where these correlations are dominated by the elliptic flow coefficient v_2 in the Fourier expansion. In the next section, we are going to explore in more details the anisotropic flow observable.

1.7 Anisotropic flow

One of the most important signatures of the QGP is the appearance of strong collective behaviour, which is often simply called 'flow'. This collective behaviour is related to the fact that particles are emitted with a strong global correlation with respect to one another and is a direct consequence of the fact that hadrons are not emitted incoherently. An illustration of this reasoning can be seen in Fig. 1.18:

- Fig. 1.18 **(a)**: particles have a mean free path much larger than the typical size of the system, resulting in an emission pattern that is uncorrelated with the symmetry plane of the event, which is called 'event plane'. Any detector measuring particle emission in a single event will detect hadrons emitted fully isotropically.

- Fig. 1.18 **(b)**: the mean free path is much smaller than the typical size of the system and particles interact strongly. In this context, ultra-relativistic hydrodynamics can be used to describe the space-time evolution of the system. More importantly, the almond-shaped initial overlap region will eventually expand in an anisotropic way, since energy density gradients are larger in the direction aligned with the event plane. Any detector measuring particle emission in a single event will, as a consequence, detect a modulation in azimuth, with particles being emitted preferentially in directions that are aligned with the event plane.

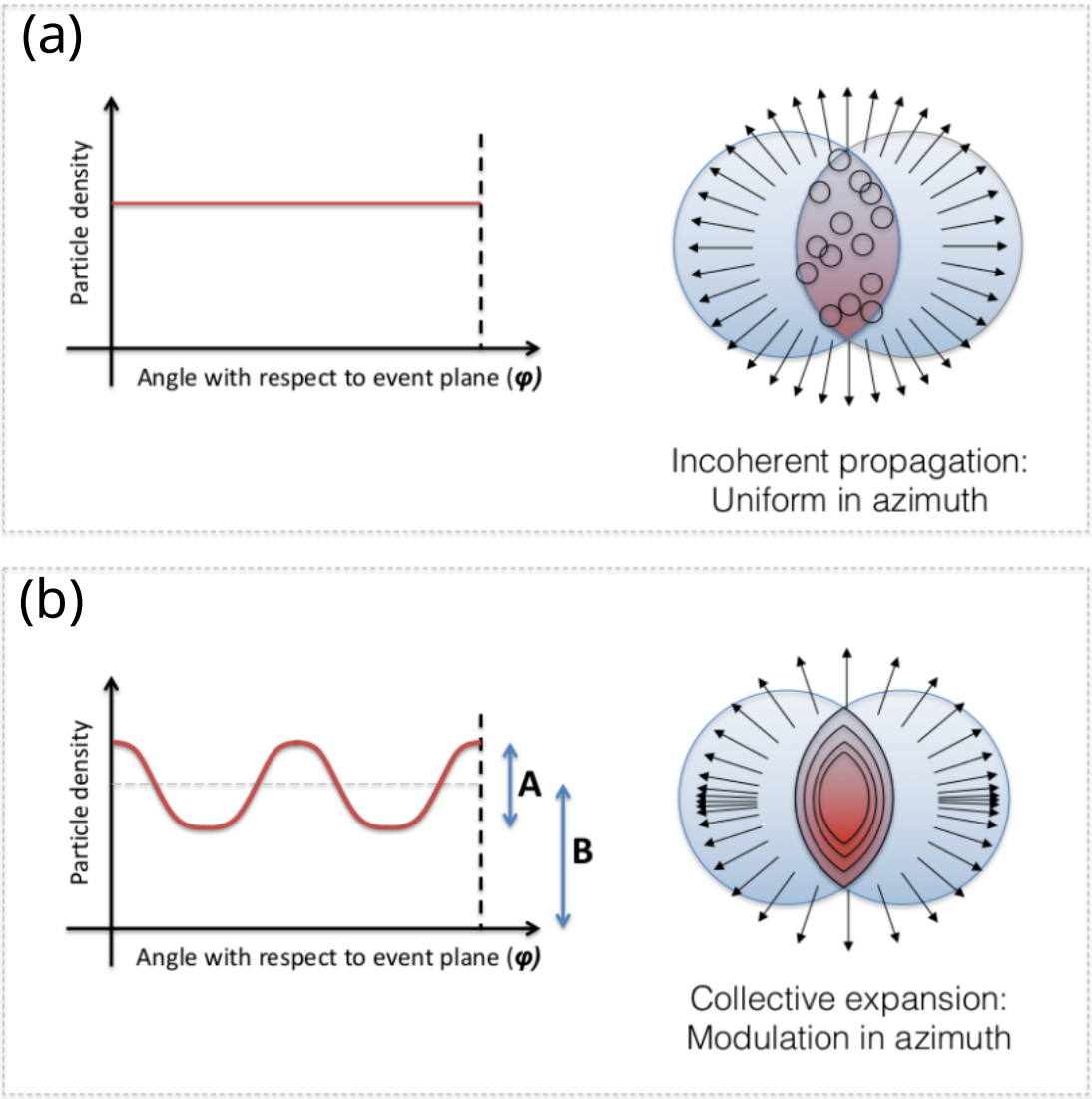

Figure 1.18: Azimuthal distribution $\mathrm{d}N/\mathrm{d}\phi$ (particle density) in non-central AA collisions, where ϕ denotes the angle with respect to the event plane. **(a)** The produced particles propagate incoherently (uncorrelated), resulting in a uniform azimuthal distribution. **(b)** The produced particles show a collective behavior, with more particles emitted in the in-plane direction than the out-of-plane direction, giving origin to a modulation in their azimuthal distribution.

The modulation of the azimuthal distribution with respect to the reaction plane shown in Fig. 1.18 **(b)** can be used to compute the magnitude of the most prominent collectivity effect, which is called 'elliptic flow' because of its symmetry. A more precise, quantitative study of this effect can be done by expanding the azimuthal particle distribution using a Fourier series. This allows us to define the coefficients v_n in the Fourier expansion of the invariant triple differential distributions [42, 43]:

$$E\frac{\mathrm{d}^3N}{\mathrm{d}^3\mathbf{p}} = \frac{1}{2\pi}\frac{\mathrm{d}^2N}{p_\mathrm{T}\mathrm{d}p_\mathrm{T}\mathrm{d}y}\left\{1+2\sum_{n=1}^{\infty}v_n\cos[n(\phi-\Psi_\mathrm{RP})]\right\}, \tag{1.15}$$

where E is the energy of the particle, $\mathbf{p}$ the momentum, p_{T} the transverse momentum, ϕ the azimuthal angle, y the rapidity and Ψ_{RP} the reaction plane (or event plane) angle. In this expansion the sine terms are zero due to the reflection symmetry with respect to the reaction plane. We can further isolate the azimuthal component of equation 1.15 by writing [70]:

$$\frac{\mathrm{d}N}{\mathrm{d}\phi} \propto 1 + 2\sum_{n=1}^{\infty} v_n \cos[n(\phi - \Psi_{\mathrm{RP}})], \tag{1.16}$$

where the flow coefficients v_n may dependent on p_{T} and rapidity y:

$$v_n(p_{\mathrm{T}}, y) = \langle \cos[n(\phi - \Psi_{\mathrm{RP}})\rangle, \quad n = 1, 2, 3, ... \tag{1.17}$$

where the angular brackets take an average over all the detected particles, summed over all events. In the expansion shown above, the coefficients v_1 and v_2 are known as directed flow and elliptic flow, respectively. Higher harmonics ($n > 2$) can also be investigated, but in this work we study only the elliptic flow, because its magnitude is much higher than the others harmonics due to the almond-shaped collision geometry in non-central heavy-ion collisions. The v_2 not only encodes information regarding this initial collision geometry but also contains crucial insight into how strongly particles must have interacted to create a certain final-state momentum anisotropy. As an example of this factorization, the v_2 is often approximated as:

$$v_2 = \kappa_2 \epsilon, \tag{1.18}$$

where ϵ is the initial state eccentricity and κ_2 is a factor that quantifies how strong the underlying interactions are and therefore how effective these are in creating a final-state momentum anisotropy. The eccentricity of the initial condition ϵ can be calculated using:

$$\epsilon = \frac{\langle y^2 - x^2 \rangle}{\langle y^2 + x^2 \rangle}, \tag{1.19}$$

where x and y are the positions of the participant nucleons in the transverse plane and the brackets denote a simple average taken over all participants [71].

Calculating v_2 is relatively easy if the event plane is known, as is the case in Monte Carlo simulations. In that case, the v_2 can be extracted immediately from the azimuthal particle distribution with respect to this event plane:

$$\frac{\mathrm{d}N}{\mathrm{d}\phi} \propto 1 + 2v_2\cos[2(\phi - \Psi_{\mathrm{RP}})]. \tag{1.20}$$

Therefore, provided Ψ_{RP} is known, a simple $A \times [1+2v_2\cos(2(\phi-\Psi_{\mathrm{RP}}))]$ fit will suffice for the calculation of v_2. Unfortunately, in the experiment Ψ_{RP} is not known, and therefore other methods are necessary for determining v_2. The most commonly used method is the multi-particle cumulant technique, which will be described in the next section.

1.7.1 Elliptic flow analysis via cumulants

Experimentally, the reaction plane angle cannot be measured directly and therefore the elliptic flow coefficient cannot be determined trivially via a fit as proposed in the previous section. The usual way to estimate the elliptic flow is using multi-particle azimuthal correlations between the observed final-state particles, which can be studied via the cumulant method. This method is rather general, but in this work we will focus on two- and four-particle azimuthal correlations, denoted by $v_2\{2\}$ and $v_2\{4\}$, respectively. First of all, we need to calculate the two-particle cumulant $\mathrm{c}_2\{2\}$ and four-particle cumulant $\mathrm{c}_2\{4\}$ as defined in Refs. [64, 72]:

$$\mathrm{c}_2\{2\} \equiv \langle\langle \mathrm{e}^{i2(\phi_1-\phi_2)}\rangle\rangle = \langle v_2^2 + \delta_2\rangle \tag{1.21}$$

and

$$\begin{aligned}\mathrm{c}_2\{4\} \equiv& \langle\langle \mathrm{e}^{i2(\phi_1+\phi_2-\phi_3-\phi_4)}\rangle\rangle - 2\langle\langle \mathrm{e}^{i2(\phi_1-\phi_2)}\rangle\rangle^2,\\ =& \langle v_2^4 + \delta_4 + 4v_2^2\delta_2 + 2\delta_2^2\rangle - 2\langle v_2^2 + \delta_2\rangle^2,\\ =& \langle -v_2^4 + \delta_4\rangle,\end{aligned} \tag{1.22}$$

where δ_2 and δ_4 represent the non-flow contributions from sources like resonance decays or jets. The v_2, δ_2 and δ_4 can also be affected by the event-by-event fluctuations, it is believed that the flow fluctuations can originate mostly from fluctuations in the initial geometry of the collision. The nucleon distribution event-by-event fluctuates and this can introduce deformations into the initial overlap region, where the fluctuations of the eccentricity ϵ will result in fluctuations in v_2, because that $v_2 \propto \epsilon$, as we see in Eq. (1.18).

One way to estimate theses fluctuations is by using the Monte Carlo Glauber simulation [73]. The non-flow contribution is practically negligible for higher-order cumulants, i.e. δ_m can be neglected for m $>$ 2. The actual v_2 can then be calculated from Eq. (1.21) and Eq. (1.22) via:

$$v_2\{2\} = \sqrt{\mathrm{c}_2\{2\}}, \tag{1.23}$$

$$v_2\{4\} = \sqrt[4]{-\mathrm{c}_2\{4\}}, \tag{1.24}$$

where we have denoted the v_2 obtained via two-particle cumulants and via four-particle cumulants by $v_2\{2\}$ and $v_2\{4\}$, respectively, being sensitive to non-flow and fluctuations.

The elliptic flow depends very strongly on centrality, as can be seen in the integrated elliptic flow as a function of centrality measured by the ALICE collaboration shown in Fig. 1.19. In these results the integrated v_2 increases from central to peripheral collisions, exhibiting a maximum value at a centrality of about $40-50\%$ and $50-60\%$. This clearly supports the geometric interpretation, according to which v_2 would be largest whenever the almond shape of the nuclear overlap region is most pronounced. These measurements also clearly indicate a hierarchy between $v_2\{2\}$ and $v_2\{4\}$, with the former having a larger magnitude due to non-flow effects. Systematic studies of the four-particle cumulant method has also shown that its estimate for the v_2 is essentially unaffected by non-flow effects [74].

As mentioned before, the v_2 coefficient can also be calculated in transverse momentum intervals. In Fig. 1.20 we show the ALICE and STAR results for the p_{T}-differential $v_2\{2\}$ and $v_2\{4\}$ for central and mid-central collisions.

The hierarchy between $v_2\{2\}$ and $v_2\{4\}$ can also be observed in the p_{T}-differential v_2, again supporting the fact that $v_2\{2\}$ is more sensitive to non-flow contributions (resonance decays and jets) compared to $v_2\{4\}$. Finally, it is also noteworthy that the p_{T}-differential v_2 in specific centrality intervals is approximately the same at RHIC and at LHC energies, meaning that elliptic flow is mostly driven by collision geometry.

In this chapter, we have laid out the foundations of heavy-ion physics and the basic signatures associated to the appearance of a QGP in these collisions. The next chapter will first explain how a QGP is usually modeled in the literature and will then expand on

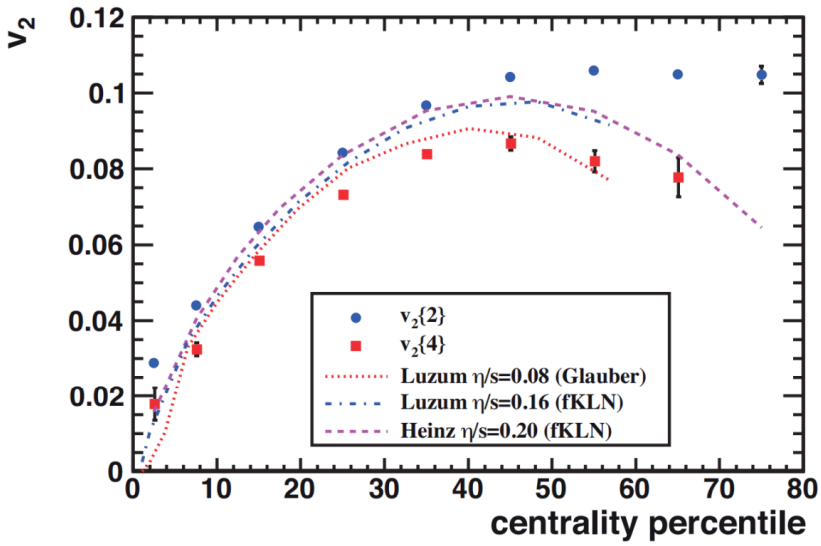

Figure 1.19: Elliptic flow integrated (v_2) over $0.2 < p_{\mathrm{T}}$ (GeV/c) < 5.0 as a function of event centrality, in Pb–Pb collisions at $\sqrt{s_{\mathrm{NN}}} = 2.76$ TeV for charged-particles at midrapidity ($|\eta| < 0.8$). The data points are the elliptic flow was calculated by the ALICE collaboration using two- and four- particle cumulant method ($v_2\{2\}$ and $v_2\{4\}$) compared to hydrodynamic simulation (dashed lines). Figure taken from [64].

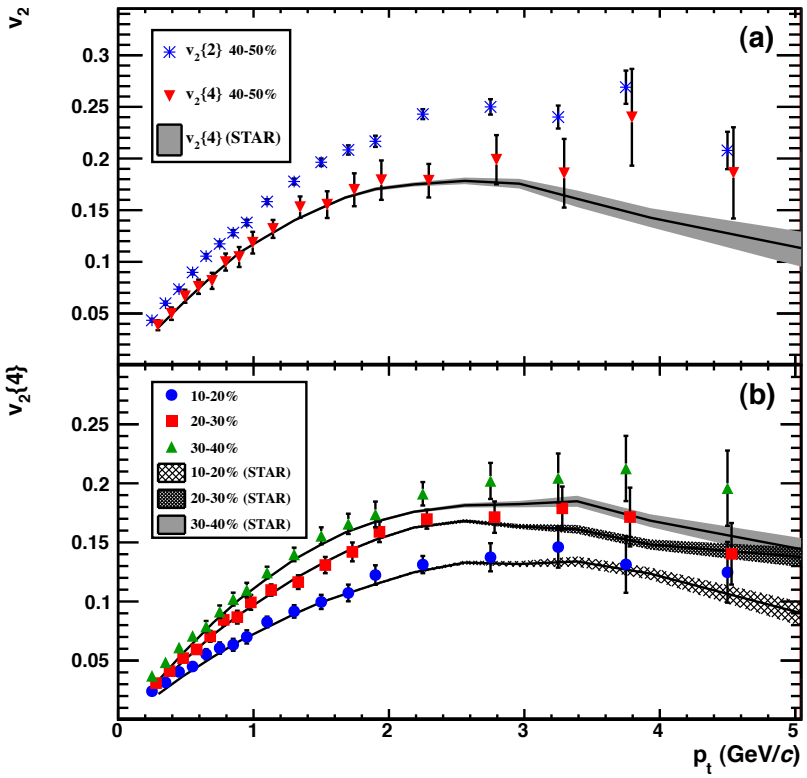

Figure 1.20: Differential elliptic flow as a function of p_{T} calculated using the two- and four- cumulant method in Pb–Pb collisions at $\sqrt{s_{\mathrm{NN}}} = 2.76$ TeV. The data points represent the values measured by the ALICE collaboration and the curves are the STAR measurements in the centrality classes (a) $40 - 50\%$, (b) $10 - 20\%$, $20 - 30\%$ and $30 - 40\%$. Taken from [75].

the proposal of this project, which is to be able to create a QGP-free baseline model for heavy-ion collisions.

Chapter 2

Heavy-ion collision model setup

2.1 Hybrid approaches

Heavy-ion physics has been a prominent field of study for several decades and, as mentioned before, is meant to explore QCD matter in extreme conditions. The QGP formed in heavy-ion ccollisions has been confirmed to behave like a perfect fluid [4–7, 76]. Its theoretical description is traditionally done using hybrid approaches based on viscous hydrodynamics [77, 78] and a hadronic cascade afterburner to simulate the hadronic phase [79, 80]. Such techniques have generally been very successful in describing the final-state observables at low-p_{T} in heavy-ion collisions.

The implementation of a hybrid model is essentially a simulation chain that is composed of simulators for each step of the system evolution in heavy-ion collision. The main components of a typical hybrid model implementation are:

- An initial condition generator such as $\mathrm{T_R}$ENTo [81] is used to generate the initial energy distribution to be passed on to a hydrodynamics simulator.
- A hydrodynamics simulator such as MUSIC [77] receives the initial energy distribution and then evolves the system using an equation of state provided by lattice QCD.
- Once the hydrodynamic evolution has cooled down sufficiently, a 'particlizer' code such as iSS [82] transforms the continuous matter/energy distribution into particles such as pions, kaons, protons and many more.

- To simulate the inelastic and elastic interactions of the resulting hadrons as well as resonance decays, a hadronic cascade simulator such as UrQMD [83] is used.

This standard hybrid approach is represented schematically in the right-hand side of Fig. 2.1, where each stage of the system evolution is portrayed explicitly, including a QGP / liquid phase. A pertinent question at this stage is: what would happen if no local equilibration was reached and the system would evolve without a QGP but still following state-of-the-art QCD-inspired modeling? Answering to this question is what we set out to do in this work.

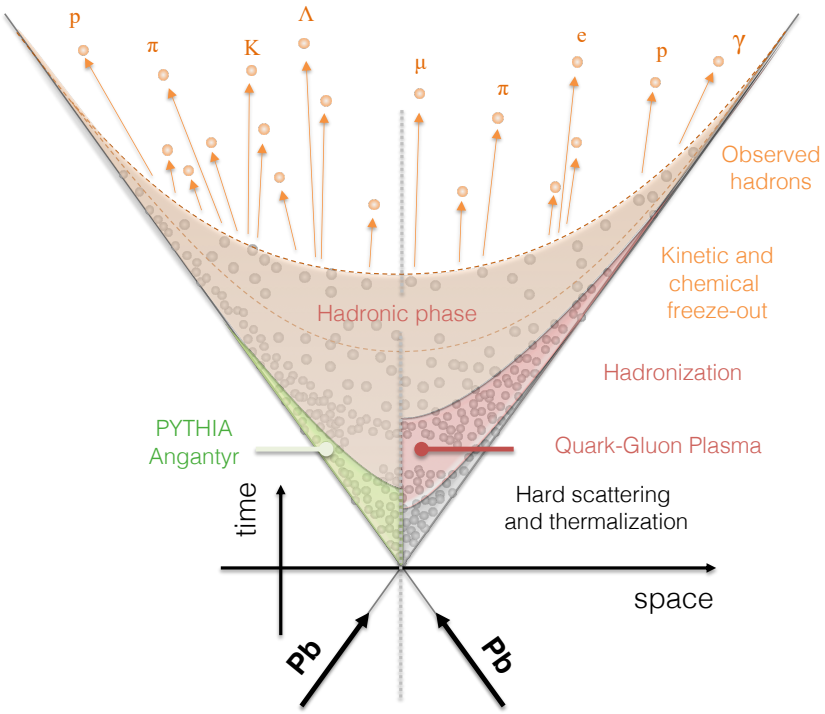

Figure 2.1: A schematic space-time diagram of the evolution of matter created in heavy-ion collisions comparing two phenomenological approaches based on: the macroscopic treatment using hydrodynamic models (right side of the figure) and the microscopic treatment using a no-QGP baseline PYTHIA/Angantyr coupling to UrQMD (left side of the figure). Taken from [84].

2.2 Objectives of this work

In this work, we will use a new alternative phenomenological approach for a heavy-ion collisions by coupling two models: the PYTHIA/Angantyr [62, 63] event generator, an improved no-QGP baseline for a heavy-ion collisions with no thermal equilibrium, and the UrQMD simulator, a hadron cascade simulator [83]. A schematic representation of this approach can be seen in the left-hand side of Fig. 2.1. Contrary to the usual hybrid

approaches, our model will not treat the system as if it were a locally-equilibrated liquid being described effectively, but we will, rather, follow each and every interaction using the best QCD models available at this time to do so. The results coming from this model will allow us to uniquely isolate signatures of the QGP from any other spurious phenomena that may appear in a QGP-free physical scenario.

The next few sections of this chapter will be dedicated to explaining how this QGP-free model was constructed, while results will be presented in chapter 3.

2.3 The PYTHIA/Angantyr model

The PYTHIA/Angantyr [62, 63] event generator is a Monte Carlo simulator for a heavy-ion collisions. It is based on the PYTHIA generator [85], a program very commonly used to simulate a high-energy collisions, e.g. proton-proton collisions. The term 'Angantyr' marks an implementation in which the PYTHIA framework is used to generalize the model to describe also pA and AA collisions. The PYTHIA model is made up of several components derived from QCD theory and is basically a leading order pQCD calculation tool that includes higher-order corrections phenomenologically and does fragmentation and hadronization via the Lund string model.

The PYTHIA event generator is able to simulate several collision systems, including lepton-lepton or hadron-hadron collisions. In this work, special emphasis will be given to the proton-proton (pp) collision system because it serves as the basic ingredient when constructing heavy-ion collisions. A pp interaction generated by PYTHIA can be divided into the following parts: Hard interaction, parton showers (Initial and Final State Radiation, ISR and FSR, respectively), multi-partonic interactions (MPI), beam remnants, hadronization and hadron decays. Below we will do a brief description of these steps.

Hard Interaction. The incoming protons are composed of quarks and gluons, each carrying a fraction (x) of the total proton momentum. The momentum fraction carried by partons of each species can be determined by experiments that use the Deep Inelastic Scattering (DIS), resulting in Parton Distribution Functions (PDFs) that are the probability densities to find a parton flavour (quark or gluon) carrying a fraction of the proton momentum. The PDFs are used to determine the partons participating in the initial hard

process characterized by the inelastic scattering at short distance with a high transferred momentum. In PYTHIA, this process is calculated to leading order in perturbative QCD.

Parton Showers. Higher-order corrections to the scattering amplitude are not calculated exactly in PYTHIA. Instead, the possibility of having e.g. a gluon radiated by the partons involved in the initial or final state is considered empirically. In PYTHIA machinery, these are called Initial State Radiation (ISR) and Final State Radiation (FSR), respectively.

Multi-Parton Interactions. One hard-parton interaction with corrections (ISR and FSR) is not enough to describe the charged-particle multiplicity observed in hadron-hadron colliders. To solve this inconsistency in the model a treatment called Multiple Parton Interactions (MPIs) [86] was proposed as a natural consequence of the composite structure of the hadrons. The MPI model allows more than one parton-parton interaction in hadron-hadron collisions and plays an important role in describing the measumerents of particle production and cross sections [87].

Beam Remnants. In hadron-hadron scattering we can have partons that do not interact and carry the remnant of the beam energy, contributing to the so-called called 'underlying event' (UE) of the collision. Another relevant contribution to the UE of a collision is the possibility of having other, semi-hard scatterings in addition to a hard scattering[1].

Hadronization and Decays. After all parton-parton interactions took place, it is necessary to describe how hadrons are produced. This is the stage known as hadronization and it is an intrinsically non-perturbative process in which the final, colorless hadrons have to be produced from a set of outgoing partons. In PYTHIA, this is done using the Lund string model, which draws inspiration from QCD and, more specifically, relies on the concept of an effective QCD potential that is $V_{\mathrm{QCD}} \approx \kappa r$ in the non-perturbative regime, as discussed in Sec.1.2 [88–91]. In the Lund string model, hadronization takes place whenever a 'string', a color flux tube that represents the basic QCD interaction between a quark and an antiquark pair, is fragmented into multiple pieces. This takes place because the effective potential increases for large values of r, and given enough energy a string may break and create a new $\mathrm{q}'\bar{\mathrm{q}}'$ pair, i.e. the string is then divided into two colour

[1]Here it is important to note that, depending on context, 'underlying event' may be defined somewhat differently and - perhaps more importantly - more operationally than theoretically. In jet studies, for instance, it may refer to anything that is not strictly correlated to jet production.

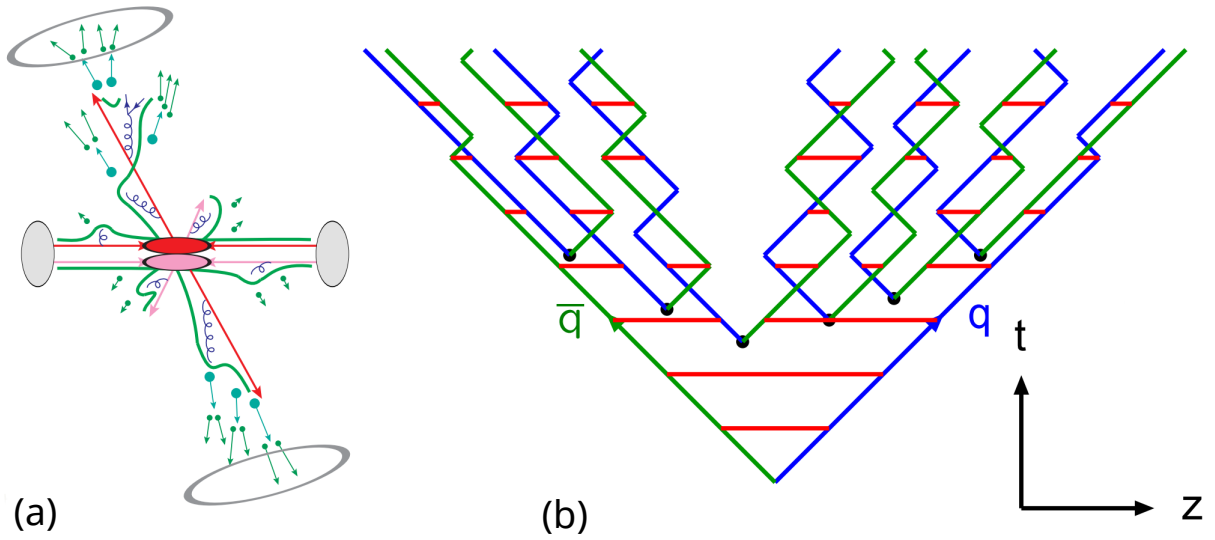

Figure 2.2: (a) The general structure of the PYTHIA event generator: Hard interaction, Radiative cascade (ISR and FSR), MPI, Lund string model, hadronization process and hadron decays. (b) The Lund string fragmentation framework describes hadron production in the quark-antiquark ($q\bar{q}$) system. Figure (a) taken from the talk "The Lund Hadronization Model", Stefan Prestel, NuSTEC workshop 2018 and (b) taken from the talk "Monte Carlo Event Generators", Torbjörn Sjöstrand, March 2006.

singlet systems $q\bar{q}'$ and $q'\bar{q}$, where each color singlet dipole may still have a large enough invariant mass for more break ups until the resulting system is solely build up of quark-antiquark pairs connected by strings of such low energy that these are effectively mesons. The formation of baryons takes place analogously, but in that case a diquark-antidiquark pair has to be formed when breaking up a string. After hadronization, hadrons may still be unstable and might decay into other particles.

An illustration of a hadron-hadron collision and the various steps carried out by PYTHIA can be seen in Fig. 2.2. The PYTHIA event generator described above is one of the main ingredients in Angantyr model to do the treatment for heavy-ion collisions.

The Angantyr model is an extension of PYTHIA for heavy-ion collisions in which a heavy-ion collision is described by combining multiple nucleon-nucleon (NN) collisions, with each of these being described by the PYTHIA machinery. This can be achieved by combining the Glauber model [37] with the addition of a diffractive excitation in each NN sub-collision. According to Gribov [92], this addition is a consequence of fluctuations in the nucleon partonic substructure. Below we will describe the four components used in the PYTHIA/Angantyr model to generate a heavy-ion collision:

1. The colliding nuclei are defined as projectile and target. For each nucleus, it is necessary to determine nucleon positions by using a nucleon distribution, e.g. the Wood-Saxon distribution [93].

2. The number of participating nucleons that undergo at least one collision and the number of NN binary collisions are estimated by the Glauber model. Each interacting nucleon from the projectile can undergo multiple sub-collisions with nucleons in the target and vice versa. This is the baseline for a heavy-ion collision, where one AA collision can be treated as a superposition of pp collisions that are independents. In Angantyr this baseline has the addition of diffractive excitation due to the individual fluctuations in nucleon partonic substructure from the projectile and target.

3. The Angantyr model is inspired by the Fritiof model for pA and AA collisions [94] and wounded nucleon model [95] to estimate the contribution of each interacting nucleon to the final state multiplicity distribution as:

$$\frac{dN_{ch}}{d\eta} = w_t F(\eta) + w_p F(-\eta), \tag{2.1}$$

where $w_{p|t}$ is the number of wounded (or participant) nucleons for the projectile and target, respectively, and $F(\eta)$ is a single nucleus emission function. In the Fritiof model the interacting nucleon can suffer an excited mass due to a longitudinal momentum exchange in the collision, i.e. the wounded nucleons can be diffractively and non-diffractively excited.

4. In one event with multiple NN collisions, each NN interaction in the Angantyr model can be defined as three types: elastic, diffractive and non-diffractive. When modeling successive interactions, Angantyr takes into account that energy and momenta must be conserved and chooses the type of collision according to the available energy. When a nucleon interacts for the first time in a given event, it is labelled as primary; this nucleon can still interact again if there is enough energy for a secondary interaction and so on until the nucleon does not have enough energy for other sub-collisions. This consideration breaks the independence between different NN interactions and sets this model apart from the usual baseline models for AA

collisions that consider that successive NN interactions are independent by construction. The NN parton-level event of the sub-collision is generated with the full PYTHIA 8.2 machinery with diffractive and non-diffractive interactions. After calculating all the NN sub-collisions between projectile and target, Angantyr generates a complete hadronic final state in pA or AA collisions using the Lund string model.

The current version of the Angantyr model does not include any effects associated to the formation of a QGP. Still, the model is capable of reproducing the final-state charged particle multiplicity distributions in pA and AA collisions fairly well [63].

Once PYTHIA/Angantyr generates final-state hadrons, these may in principle still interact inelastically and elastically in a hadronic phase. In order to simulate this further step in the system evolution via the UrQMD hadronic cascade simulator, it is necessary to know where in space and time each individual hadron is created in the Lund string model. In order to do so, we have employed a brand new implementation of the hadron vertex model [96] in PYTHIA/Angantyr + UrQMD that was done by Christian Bierlich, the main author of the Angantyr extension to PYTHIA. The hadron vertex model will be described in the next section.

2.3.1 Hadron vertex model

As described before, hadron creation in PYTHIA is done using the Lund string model. However, it is important to note that the fragmentation process is worked out entirely in the energy-momentum picture, i.e., PYTHIA actually tracks the energies contained in each string as opposed to positions. To study the configuration of hadrons created after hadronization, it is necessary to translate energy-momentum to space-time information. This translation was recently incorporated in PYTHIA 8.235 by Silvia Ferreres-Solé and Torbjörn Sjöstrand [96] and can be done taking advantage of the fact that the confinement potential $V_{\mathrm{QCD}} \approx \kappa r$ establishes a linear relation between energy-momentum and space-time, where the vertex (v) location of the string breakup for the simple $\mathrm{q_0\bar{q}_0}$ system can be defined as:

$$v = \frac{x^+ p^+ + x^- p^-}{\kappa}, \tag{2.2}$$

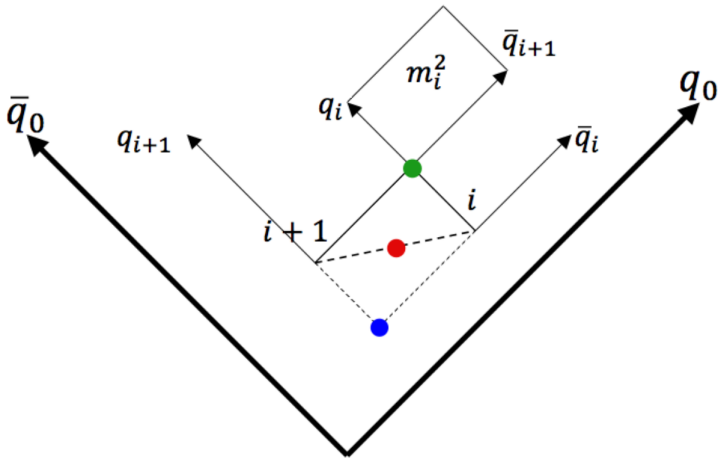

Figure 2.3: Hadron creation in a $q_0\bar{q}_0$ system in the Lund string model. The points are definitions for the hadron production labeled as "early" (blue), "middle" (red) and late (green). The meson created is formed by a quark (q_i) and an antiquark ($\bar{q}_{i+1}$) system with an invariant mass m_i. Figure taken from [96].

where $x^{\pm}$ are the light-cone coordinates of the breakup point ($0 \leq x^{\pm} \leq 1$), $p^{\pm}$ are the four-momenta for the quark and antiquark and κ is the string tension. The hadron is created in the string by two adjacent breaks and the hadron production vertex (v^h) is defined as the average between the break point i and $i+1$:

$$v_i^h = \frac{v_i + v_{i+1}}{2}. \tag{2.3}$$

This hadron vertex (v_i^h) is represented by the red point in Fig. 2.3 defined as "middle". The middle definition is not the unique choice to the hadron production point: two other alternatives, called "late" and "early", are represented as the green and blue points, respectively, in Fig. 2.3. These can be defined as:

$$v_{l,i}^h = \frac{v_i + v_{i+1}}{2} + \frac{p_h}{2\kappa}, \tag{2.4}$$

$$v_{e,i}^h = \frac{v_i + v_{i+1}}{2} - \frac{p_h}{2\kappa}, \tag{2.5}$$

where $v_{l,i}^h$ and $v_{e,i}^h$ are the definitions for the late and early options, respectively, and p_h is the hadron four-momentum. Some other, more complex string topologies are also considered in the hadron vertex model and more details about those can be found in Ref. [96].

These three possibilities of placing hadrons in a space-time picture can be used as a measurement of the uncertainty of the model, as discussed in Ref. [96]. We will study this model uncertainty for the nuclear modification factor (R_{AA}) and the result will be show in section 3.2.1. Unless otherwise stated, we have used the default middle option that is the default configuration of PYTHIA 8.2 for all main results in this thesis.

The space-time information of the produced hadrons allow us to couple the output of PYTHIA/Angantyr to UrQMD. All hadronic positions at hadronization are stored in an intermediate output file and are then passed along to UrQMD, which then is able to calculate inelastic and elastic interactions as well as particle decays. As an example, in Fig. 2.4 we show two Pb–Pb collisions at $\sqrt{s_{\rm NN}} = 2.76$ TeV generated by PYTHIA/Angantyr in the centrality classes of $0-5\%$ and $30-40\%$. In this figure we can also see the nuclei of Pb illustrated with red circles to mark the region in the transverse plane in which nucleon-nucleon interactions actually took place in the model.

The hadron creation position $(x-y)$ distributions for some events generated by PYTHIA/Angantyr in Pb–Pb collisions at $\sqrt{s_{\rm NN}} = 2.76$ TeV are exemplified in Fig. 2.5 to characterize the system size created for the most central $(0-5\%)$ and mid-central $(40-50\%)$ collisions, where the core size and system size are approximately 5 fm and 10 fm, respectively. The initial geometry in heavy-ion collision has a clear influence in the hadron position distributions for the final state particles, as we can see in Fig. 2.5, where Fig. 2.5a shows a distribution almost symmetric for the most central collision and Fig. 2.5b shows a distribution with the form of an almond-like shape for a non-central collision.

Using the space-time information of hadron production it is possible to study the implications of this new model and one good start is to look in the transverse Radius (R) distribution of the hadron produced as a function of transverse momentum ($p_{\rm T}$), as we can see in Fig. 2.6, for events generated by PYTHIA/Angantyr in Pb–Pb collisions at $\sqrt{s_{\rm NN}} = 2.76$ TeV. By inspecting the transverse Radius (R) distribution for five $p_{\rm T}$ ranges in Fig. 2.6, we can see a linear relation between $p_{\rm T}$ and hadron positions, where low-$p_{\rm T}$ particles are produced close to the center of the system and high-$p_{\rm T}$ particles are created close to the surface of the system produced in heavy-ion collisions, e.g. the low- and high-$p_{\rm T}$ particles in the ranges of $0 < p_{\rm T}$ (GeV/c) < 2 and $12 < p_{\rm T}$ (GeV/c) < 100 are around of $R \approx 3$ fm and $R \approx 10$ fm, respectively. This linear relationship between momentum

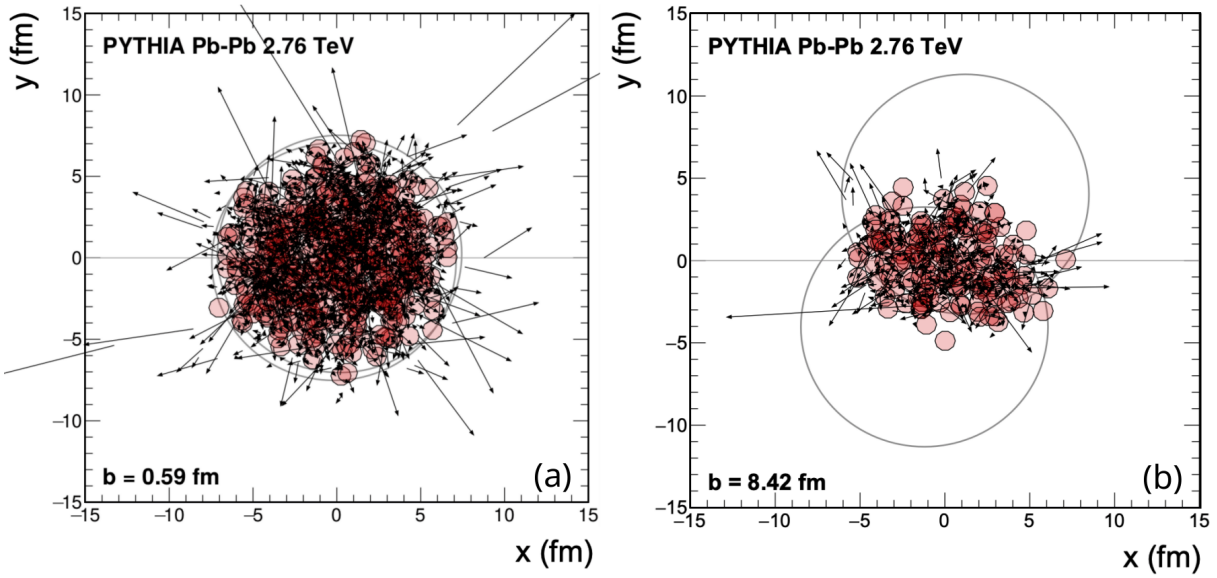

Figure 2.4: Hadron position $(x - y)$ distributions of one event generated by PYTHIA/ Angantyr + UrQMD in Pb–Pb collision at $\sqrt{s_{\rm NN}} = 2.76$ TeV after hadronization process. Arrows are placed starting at a hadron creation position and point in the direction of the velocity of the outgoing hadron, while circles mark the positions of the initial nucleons that interacted in the collision. The left plot (a) shows a central collision and the right plot (b) shows a mid-central collision example.

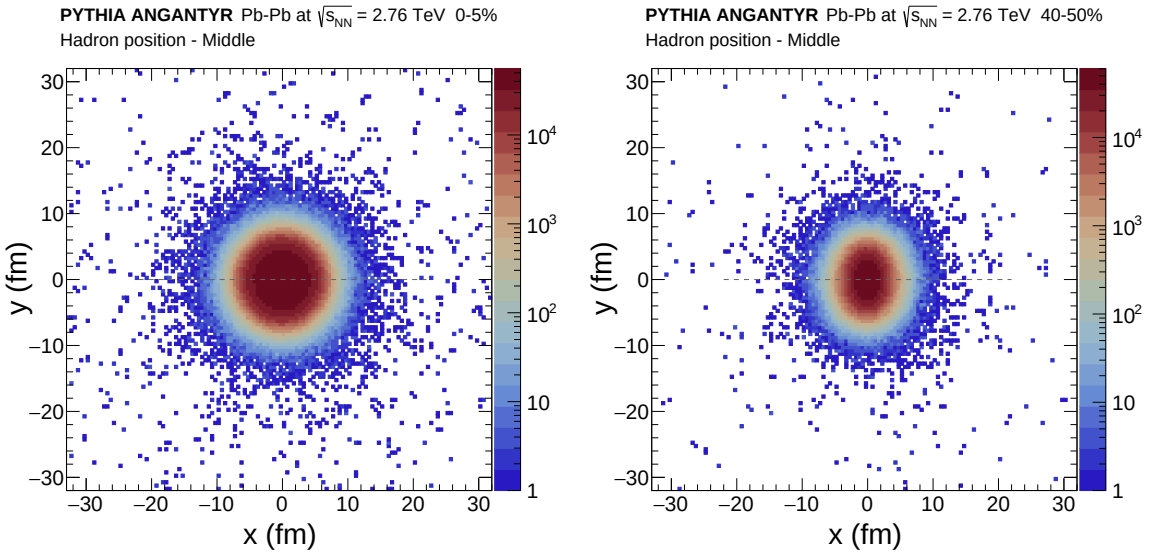

Figure 2.5: Hadron position $(x - y)$ distributions of charged particles from PYTHIA/ Angantyr + UrQMD in 0-5 % (**a**) and 40-50 % (**b**) centralities for Pb–Pb collisions at $\sqrt{s_{\rm NN}} = 2.76$ TeV. For both distributions, we rotate each event with respect to the reaction plane angle ($\Psi_{\rm RP}$) provided by PYTHIA/ Angantyr.

and position is important to understand the nuclear modification factor (R_{AA}) predicted by our simulations that will be shown in the results.

We will now proceed and describe how we simulated a full Pb–Pb event including a hadronic phase by first explaining the software we used for modeling this hadronic phase and then explaining the coupling between PYTHIA/Angantyr and UrQMD.

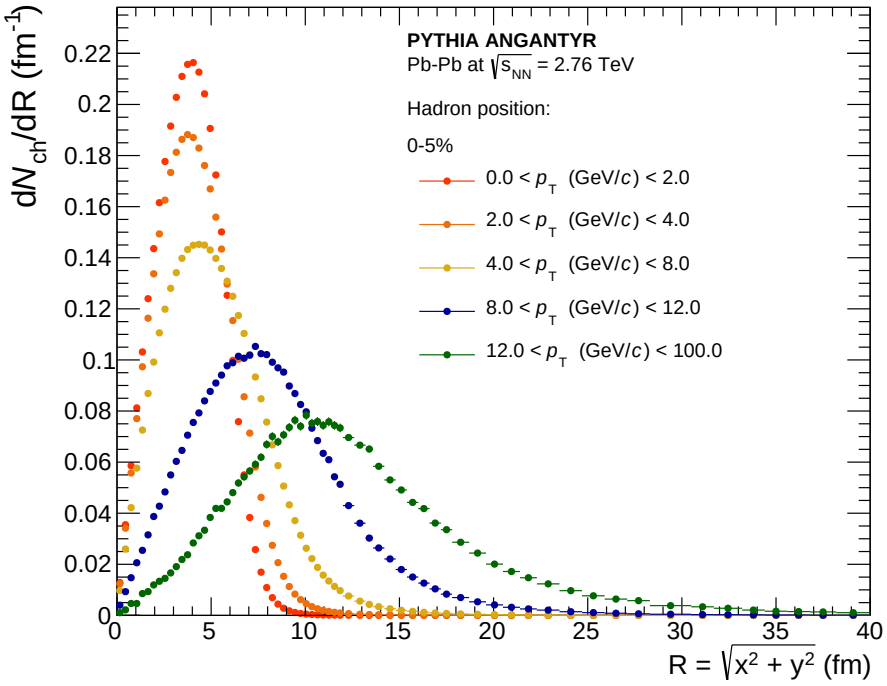

Figure 2.6: Transverse radius R distribution of hadrons created (charged-particles) for five ranges of transverse momentum (p_{T}) from PYTHIA/Angantyr in 0-5 % centrality for Pb–Pb collisions at $\sqrt{s_{\mathrm{NN}}} =$ 2.76 TeV.

2.4 The UrQMD model – hadronic cascade simulator

The Ultra-relativistic Quantum-Molecular-Dynamics (UrQMD 3.4) [83, 97] model is a microscopic transport simulator that describes the propagation of hadrons based on classical trajectories and performs hadron-hadron scatterings, string excitation (Lund string model) and resonance decays. The simulator is able to evolve the system of particles in the hadronic phase by using the four-momenta to calculate the total cross section (σ_{tot}) of hadron-hadron collisions. The total cross-sections (σ_{tot}) of hadron-hadron interactions are purely geometrical, and a given collision of two hadrons will happen if the impact parameter (d) between them follows $\mathrm{d} < \sqrt{\sigma_{\mathrm{tot}}/\pi}$. Hadrons can undergo multiple inelastic or elastic rescatterings with other particles in the system and particles produced in inelastic collisions can continue interacting with others hadrons. The system will evolve until it reaches the final stages of chemical and kinetic freeze-out, at which point particles stop interacting inelastically and elastically, respectively. In the next section we will describe the coupling of PYTHIA/Angantyr to UrQMD.

2.5 PYTHIA/Angantyr + UrQMD setup

We now describe the details that had to be taken care of to couple the PYTHIA/ Angantyr event generator to the UrQMD hadronic cascade simulator. The first challenge we encountered while doing this coupling is that UrQMD is unable to handle all particle species and restrictions had to be made to avoid difficulties. In this context, the first study we had to do was to classify the particle abundances by particle species from PYTHIA/Angantyr and separate these into particles that UrQMD can and cannot handle, as can be seen in Fig. 2.7. The figure shows the fraction of total particle types from events generated by PYTHIA/Angantyr for Pb–Pb collisions at $\sqrt{s_{\mathrm{NN}}} = 2.76$ TeV until after hadronization with decays off. We were able to determine that 99.81% of all particles can be handled by UrQMD 3.4 to perform the rescatterings and decays of unstable hadrons, while the other 0.19% are particles such as hadrons with heavy flavour quarks, leptons and photons that are not treated by UrQMD 3.4. To make this coupling work, the hadrons with heavy flavours quarks are decayed by PYTHIA and the decay products are directly passed to UrQMD, while leptons and photons are removed from the event record altogether.

Once these special actions are taken to correct for technical limitations of UrQMD, we now structure the simulation output for convenient analysis at the post-processing level. Three different outputs are generated simultaneously for later study:

- **output1**: This output typen stores all information generated by PYTHIA/Angantyr in AA collisions at the moment of hadronization and therefore prior to any particle decays (except for heavy flavour hadrons). In addition to particle-level information, this output already contains event properties such as the impact parameter (b), the number of NN binary collisions (N_{coll}), the number of participating nucleons (N_{part}) and the position of the colliding nuclei centers. In this work, this output is always denoted as 'after hadronization' when presented in a plot. This output also serves as input for UrQMD to generate the other two types of output.

- **output2**: This output stores the four-momenta and particle species information of all hadrons after a UrQMD simulation in which unstable hadrons decayed but no hadronic interactions took place. While physically not very reasonable, this is an

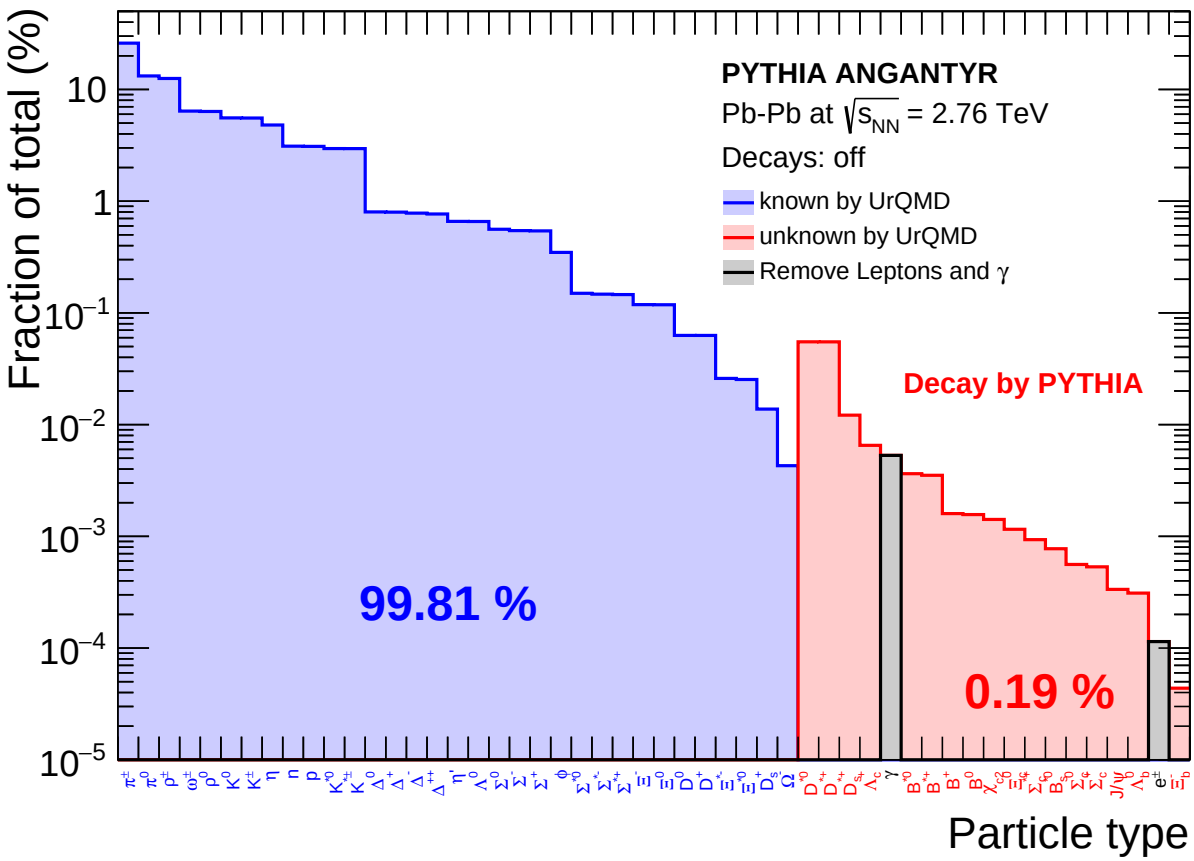

Figure 2.7: Fraction of total (%) of particle types produced after hadronization by the PYTHIA/Angantyr event generator in Pb–Pb at $\sqrt{s_{\rm NN}}$ = 2.76 TeV. The blue distribution shows the 99.81% of all the particle species that are known by the UrQMD model and the red distribution shows the 0.19% of all particles that are unknown to the UrQMD simulator, such as hadrons with heavy flavour quarks, leptons and photons.

important tool in understand the exact effects hadronic interactions. This type of output will be referenced as 'decays only' in this work.

- **output3**: This output stores the four-momenta, particle species information and number of hadronic collisions of the hadrons after a UrQMD simulation in which both decays and hadronic interactions are allowed to take place. This output will be called 'decays and interactions' in what follows.

As part of the studies in this thesis, we have generated approximately 14 million events for each stage with the PYTHIA/Angantyr + UrQMD simulation chain for Pb–Pb collisions at $\sqrt{s_{\rm NN}}$ = 2.76 TeV. As a first test of the simulation chain, we have studied the characteristics of the events generated by our simulations by calculating the invariant time $\tau = \sqrt{t^2 - z^2}$ distribution for hadron creation vertices as well as for the hadronic interactions that were simulated by UrQMD, as can be seen in Fig. 2.8.

We can understand that after hadronization a significant fraction of all hadrons are created around 1-2 fm/c, which is significantly different compared to hydrodynamics-based simulations, in which the system evolves as a continuous medium until $\mathcal{O}(10$ fm/$c)$. As PYTHIA/Angantyr generates almost all hadrons in the beginning of the system evolution, this will also lead to a rather dense hadronic medium, which may, in turn, mean that

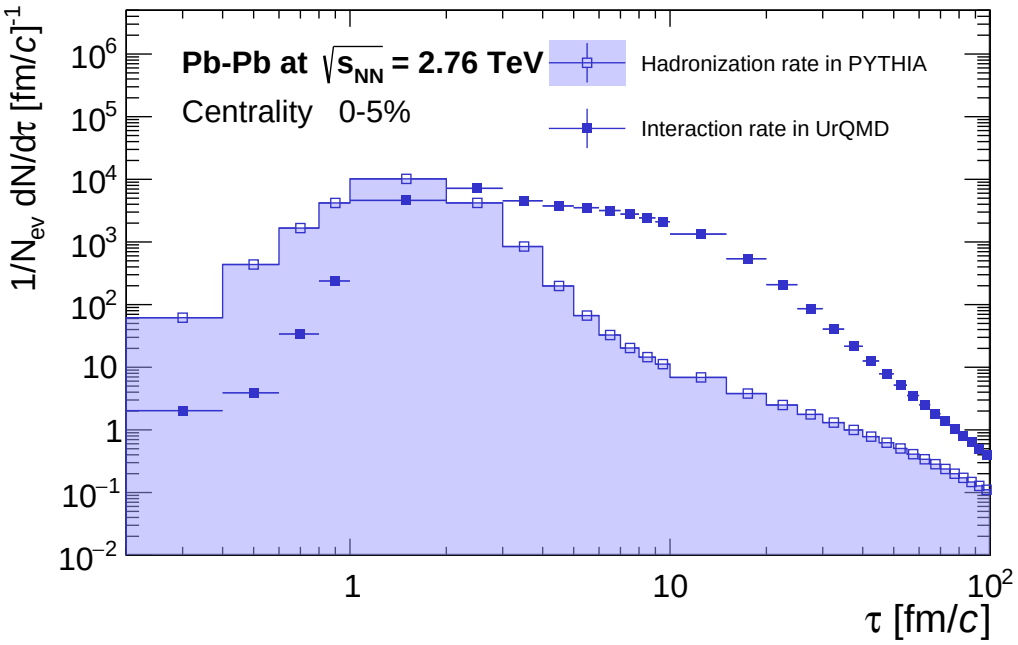

(a)

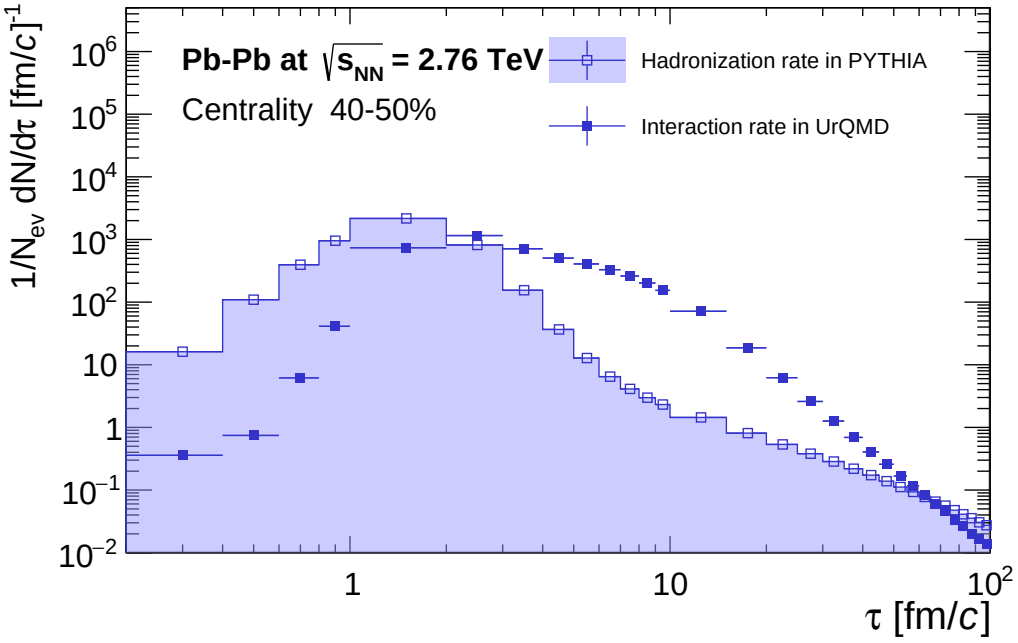

(b)

Figure 2.8: Invariant time $\tau = \sqrt{t^2 - z^2}$ distribution of hadrons created by PYTHIA/ Angantyr + UrQMD and time distribution of rescattering rate of the UrQMD in the hadronic phase for Pb–Pb collisions at $\sqrt{s_{\mathrm{NN}}} = 2.76$ TeV for the 0-5 % (**a**) and 40-50 % (**b**) centralities. Figure taken from [84].

hadronc phase effects are more significant than in traditional hybrid models. A clear explanation for the long-lasting interaction rate is also that the majority of particles have low p_{T} and will therefore be produced close to the core of the system, as shown in Fig. 2.6, and their close proximity in both time and space will mean a significant interaction rate until the system has expanded significantly. In the next section we will describe the centrality determination for events generated by PYTHIA/Angantyr + UrQMD with different options to do the centrality calibration.

2.6 Centrality determination

This section describes in details how the centrality classes was selected for the data analysis of the events generated by the PYTHIA/Angantyr + UrQMD hybrid model. In heavy-ion physics, the nucleus-nucleus (AA) collisions are extended objects and the multiplicity of particles produced depends on the impact parameter (b) of the collision. In Fig. 2.9(**a**) we show the longitudinal view before the collision, where the nuclei (AA) are moving in opposite directions, with R_A being the nuclear radius of the nucleus A and the impact parameter (b) is defined as the distance between the center of the nucleus with respect to the beam z-axis, in transverse plane $(x-y)$. The Fig. 2.9(**b**) shows the transverse view $(x-y)$ of the collision with the overlap region between the nuclei represented by the almond-like shape. To study heavy-ion collision is convenient to introduce the definition of centrality of the collision (as defined in Sec.1.4.2) that is directly related with the impact parameter (b) as showed in Fig. 2.9(**c**), where we can classify the centrality of the collision, as a central collision with b $\rightarrow 0$ and peripheral collision with b $\rightarrow 2R_A$.

The geometrical quantities such as impact parameter (b), the number of participating (nucleon who has undergone at least one collision) (N_{part}) and spectators (nucleons that do not participate in the collision) (N_{spec}) defined as $N_{spec} = 2A - N_{part}$, where A is the total number of nucleons inside the nuclei and the number of binary nucleon-nucleon (NN) collisions (N_{coll}) cannot be measured directly by heavy-ion experiments. In this context, the Glauber model [36, 37, 98] is widely used to calculate geometric quantities.

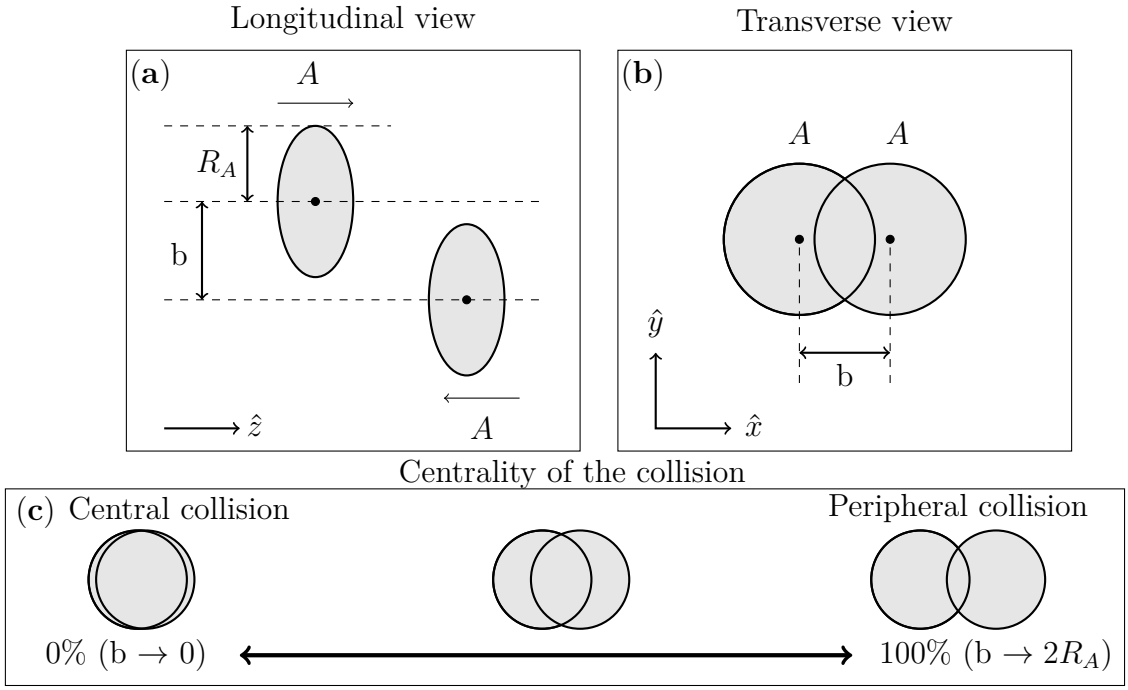

Figure 2.9: Initial geometry of the heavy-ion collision.

2.7 The Glauber model

The purpose of Monte Carlo approach of the Glauber model is to calculate geometric quantities in heavy-ion collisions. Basically, the Glauber model describes a nuclear collision of two nuclei as a superposition of independent NN collisions on an event-by-event basis.

2.7.1 Inputs

To calculate all the geometric quantities, the Glauber model needs two inputs: the nuclear charge densities ($\rho(r)$) and the inelastic (NN) cross section σ_{NN}^{inel} as a function of center-of-mass energy:

- **Nuclear charge densities**

  In the Glauber model, the first step is to determine the nucleons positions in each nucleus using the nuclear charge density function. The most widely used nuclear charge density is the Wood-Saxon distribution [93]:

$$\rho(r) = \rho_0 \frac{1 + w(\mathrm{r/R})^2}{1 + \exp\left(\frac{\mathrm{r-R}}{a}\right)} \tag{2.6}$$

where ρ_0 is the nucleon density in the center of the nucleus, a is the skin depth and w refers to deviations of a uniformly dense core. The parameters of the nuclear charge densities are based on measurements in low-energy electron-nucleus scattering experiments [99]. The parameters for the Xenon (Xe) and Lead (Pb) nuclei used in the nuclear charge density function in the Fig. 2.10 are listed in Table 2.1.

Table 2.1: The parameters for the nuclear charge density function (Woods-Saxon density distributions) for the nucleus Xenon (Xe) and Lead (Pb). Data taken from [99]:

Nucleus	A	R_A (fm)	a (fm)	w
Xe	129	5.420	0.570	0.000
Pb	208	6.620	0.546	0.000

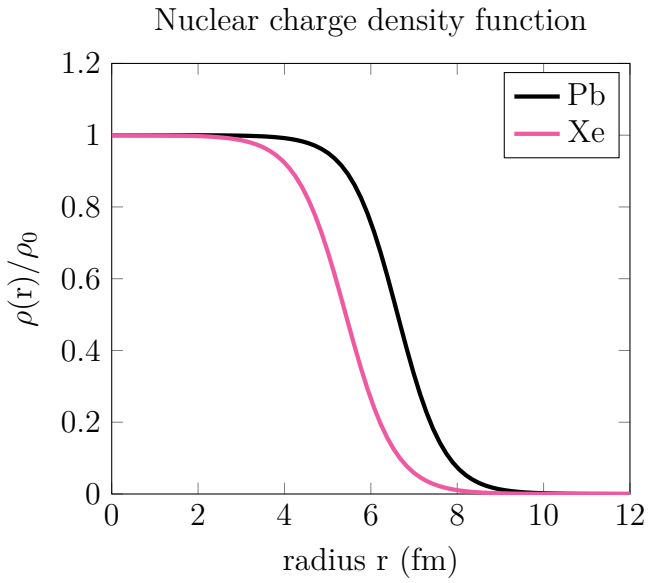

Figure 2.10: Nuclear charge density function for Lead (Pb) and Xenon (Xe). The parameters are based on data from [99].

The second step is to generate the impact parameter (b) distribution randomly based on the geometrical distribution to simulate a nuclear collision:

$$\frac{\mathrm{d}P}{\mathrm{db}} \propto \mathrm{b}. \tag{2.7}$$

- **Inelastic nucleon-nucleon cross section**

In high energy nuclear collisions, the inelastic NN cross section (σ_{NN}^{inel}) is associated to the diffractive and non-diffractive processes. At RHIC and LHC energies the

diffractive processes are expected to be a large fraction of the inelastic cross section [100, 101]. For the Glauber model, the (AA) collision is described as a sequence of independent NN collisions, where the nucleons move in straight-line trajectories and the inelastic cross section is considered to be independent of the number of collisions a nucleon underwent previously, as can be seen in Fig. 2.11). A binary NN collision will happen when the distance (d_{ij}) in the transverse plane $(x-y)$ is less than or equal to d, as shown in Fig. 2.11 by the geometric cross-sectional area that can be directly interpreted as the probability of an NN interaction.

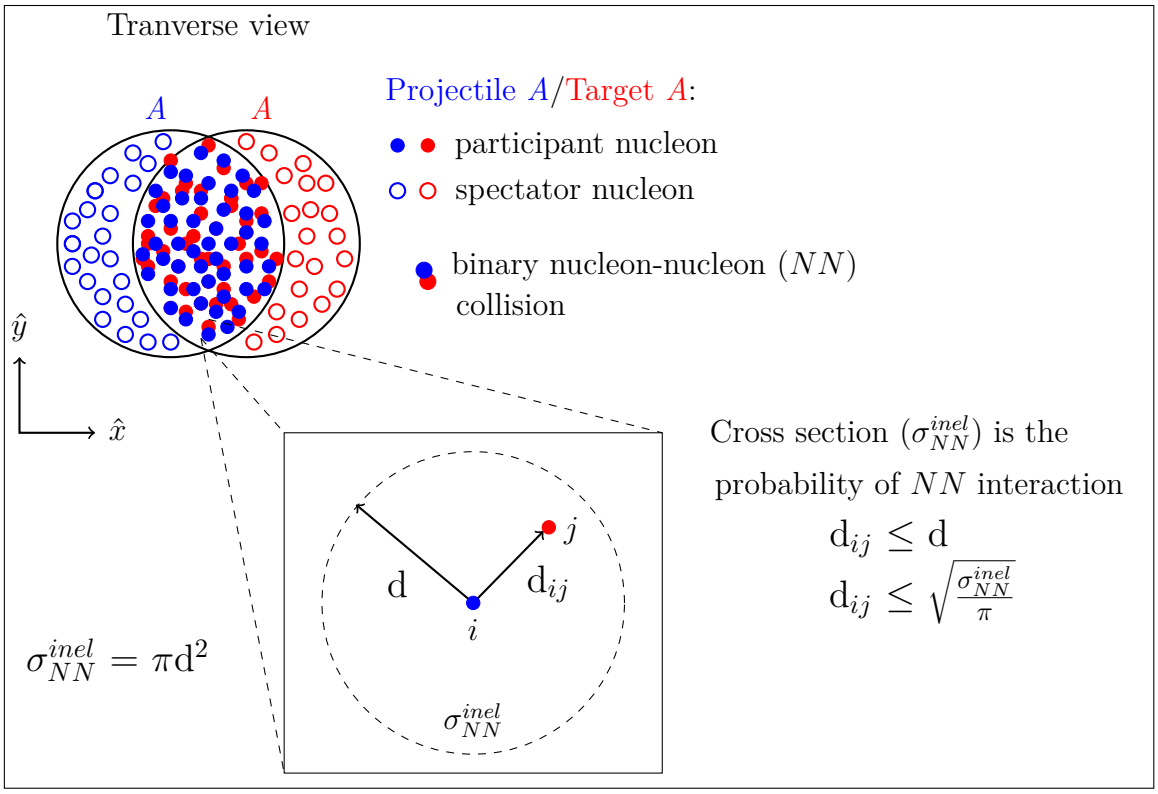

Figure 2.11: The transverse view of a heavy-ion collision describe by the Glauber model.

As the geometry of the collision is necessary to study a heavy-ion collision, in the next section we will describe the different options for centrality calibration by selecting on b, N_{ch} at midrapidity ($|\eta| < 0.5$) or N_{ch} at forward rapidities of $-3.7 < \eta < -1.7$ and $2.8 < \eta < 5.1$, corresponding to the acceptance of the V0M detectors of the ALICE experiment.

2.8 Centrality calibration

In our simulations we have three variables that allow us to select on event centrality: impact parameter (b), N_{ch} midrapidity and N_{ch} at forward rapidity. We generate events with PYTHIA/Angantyr + UrQMD in Pb–Pb collisions at $\sqrt{s_{\mathrm{NN}}} = 2.76$ TeV to show the different options to do the centrality calibration. We start selecting the impact parameter b to determine the event centrality by using the distribution of impact parameter generated by PYTHIA/Angantyr, as can be seen in Fig. 2.12. In this figure, we use the impact parameters minimum ($\mathrm{b_{min}}$) and maximum ($\mathrm{b_{max}}$) to classify the centrality in percentiles ranging from 0% to 100%, respectively. In this way we can divide the centrality in classes, e.g. the centrality bin of $0-5\%$ stands for the 5% of all events with the lowest impact parameters, also called the most central collisions, and $90-100\%$ is the 10% of all events with the highest impact parameters.

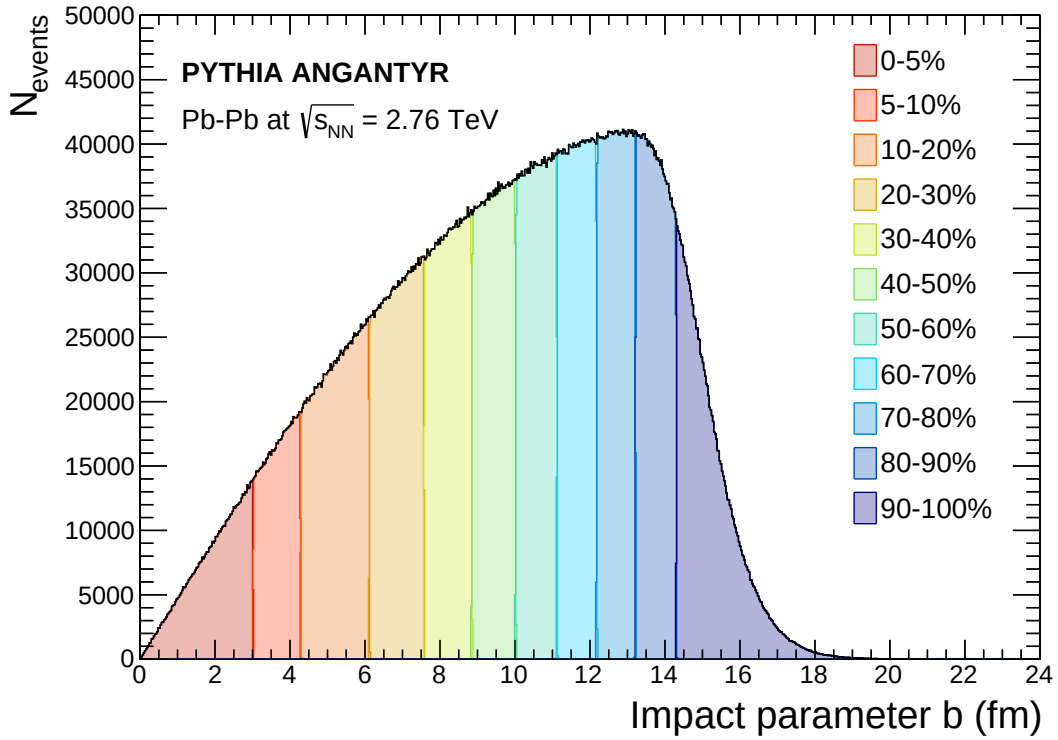

Figure 2.12: Distribution of impact parameter (b) generated by PYTHIA/Angantyr in Pb–Pb collisions at $\sqrt{s_{\mathrm{NN}}} = 2.76$ TeV with the classification of centrality based on b, where the centrality is divide in classes represented by the color bands, as described by subtitle in the right side of the figure.

Using the impact parameter to classify the event centrality is only possible in Monte Carlo simulations. As we know that the impact parameter cannot be measured directly by experiments in heavy-ion collisions, so one way to determine the event centrality is to use the N_{ch} multiplicity because has a correlation with the impact parameter. From our

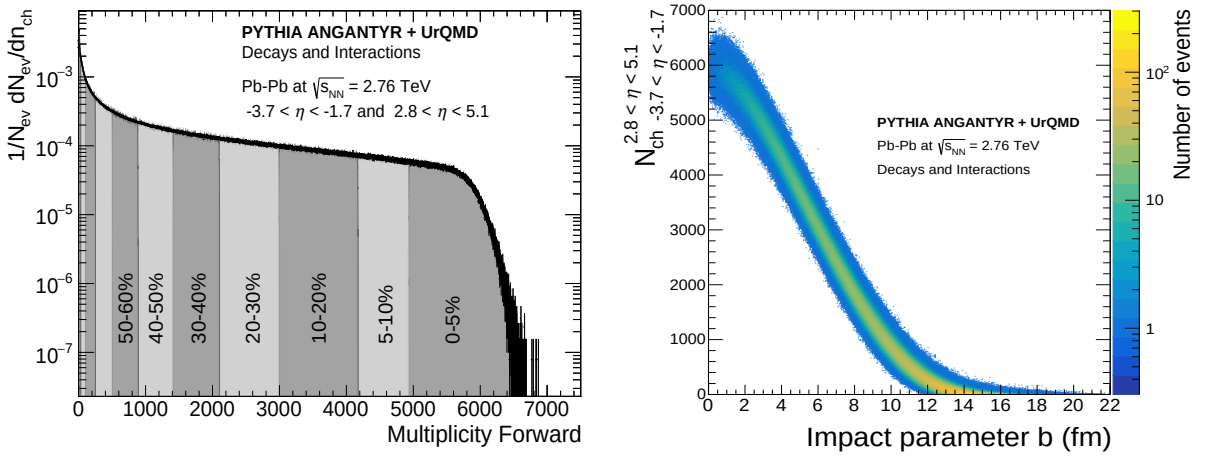

(a) **(b)**

Figure 2.13: (a) Charged-particle multiplicity $N_{\rm ch}$ forward distribution generated by PYTHIA/Angantyr + UrQMD in Pb–Pb collisions at $\sqrt{s_{\rm NN}}$ = 2.76 TeV for $N_{\rm ch}$ forward region ($-3.7 < \eta < -1.7$ and $2.8 < \eta < 5.1$), with the centrality classes represented by the gray bands below the distribution. The figure (b) shows the correlation between the $N_{\rm ch}$ forward and impact parameter (b) from PYTHIA/Angantyr + UrQMD in Pb–Pb collisions at $\sqrt{s_{\rm NN}} = 2.76$ TeV for charged-particles at forward region.

simulations we also compute the $N_{\rm ch}$ multiplicity distribution at $-3.7 < \eta < -1.7$ and $2.8 < \eta < 5.1$ to determine the event centrality by using the $N_{\rm ch}$ forward, as can be seen in Fig. 2.13a, where the centrality classes are classified as described in Sec. 1.4.2 using Eq. (1.8). Fig. 2.13b shows the correlation between the $N_{\rm ch}$ forward with the impact parameter b, i.e. for lower values of b more particles are produced and for higher values of b less particles are created. To do a fair comparison of the model predictions with real data, we use the centrality calibration based on $N_{\rm ch}$ forward in the results shown in Chapter 3.

In Fig. 2.14, we compare the three different options of centrality calibration (b, $N_{\rm ch}$ midrapidity and $N_{\rm ch}$ forward) in our simulations for the $N_{\rm ch}$ multiplicity density distribution at midrapidity versus the event centrality. The comparison between the three options of calibration does not show a significant difference from central $(0-5\%)$ to peripheral $(70-80\%)$ collisions, but there is a difference for UPC $(80-90\%$ and $90-100\%)$.

Now that our new hybrid, QCD-inspired, QGP-free model for a heavy-ion collision has been set up and explained, we will proceed to study the consequences of this approach by comparing the predictions from this model to published experimental data for various observables.

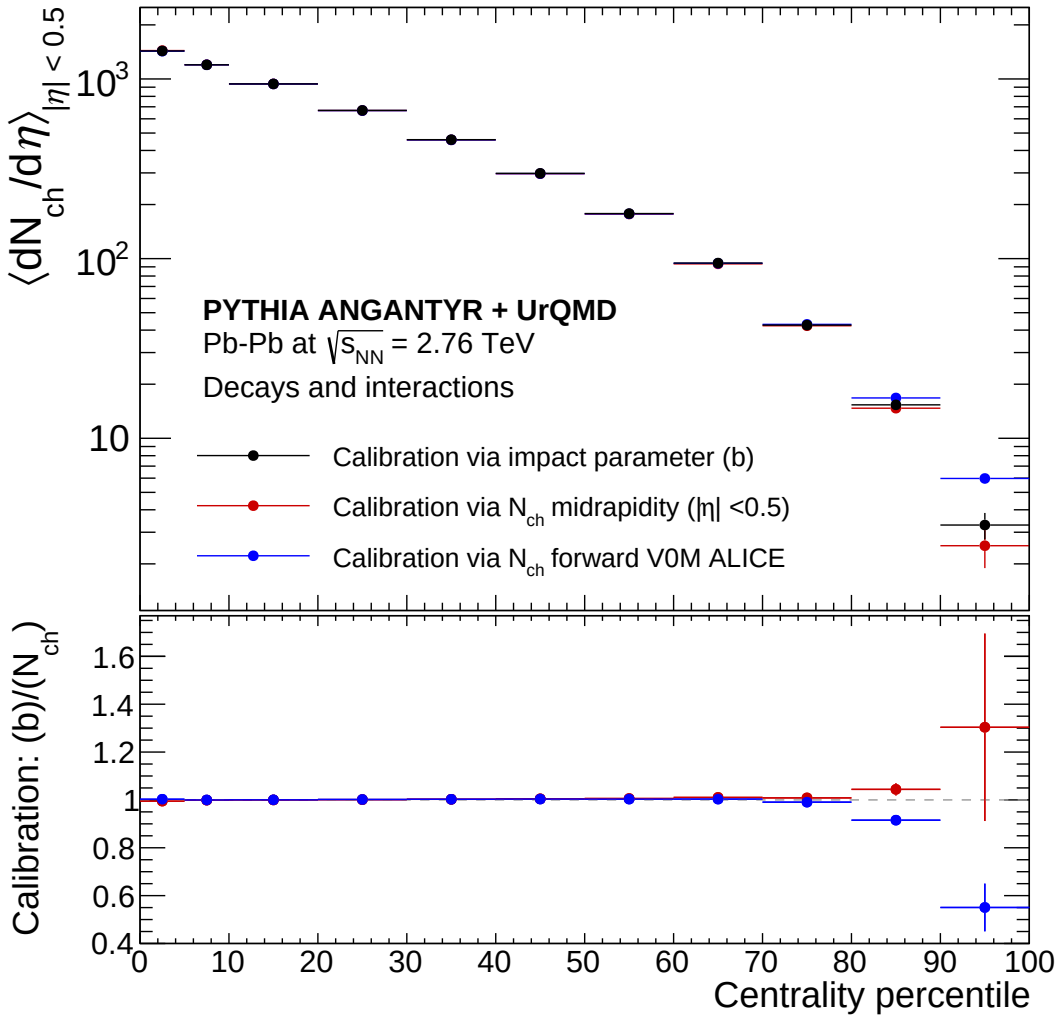

Figure 2.14: Charged-particle multiplicity density distribution at midrapidity ($|\eta| < 0.5$) as a function of event centrality, for Pb-Pb collisions at $\sqrt{s_{\rm NN}} = 2.76$ TeV generated by PYTHIA/Angantyr + UrQMD for decays and interactions. We calculate the distribution for different options of centrality calibration by using the impact parameter (b), charged-particle multiplicities $N_{\rm ch}$ at midrapidity and $N_{\rm ch}$ forward V0M ALICE ($-3.7 < \eta < -1.7$ and $2.8 < \eta < 5.1$), on top of the figure. In the bottom the ratio to compare the distributions: calibration via b with respect to via $N_{\rm ch}$ midrapidity or $N_{\rm ch}$ forward. The vertical lines are the statistical uncertainties in the model.

Chapter 3

Results and discussion

In this chapter, we present the results from the PYTHIA/Angantyr + UrQMD hybrid model for heavy-ion collisions. We are now in a position to check multiple observables such as charged-particle multiplicity densities, transverse momentum (p_{T}) distributions, anisotropic flow and others. In the next few sections we will proceed by systematically going from the simpler observables, such as multiplicities, to the more intricate and specific. This will allow us to see how our hybrid model that does not assume QGP matter describes the main observables in heavy-ion collisions.

3.1 Global event properties

The charged-particle multiplicity density is a basic observable to quantify the particle production that is directly related to the initial geometry and total energy in heavy-ion collisions. The charged-particle multiplicity density ($\langle\, \mathrm{dN_{ch}}/\mathrm{d}\eta \,\rangle_{|\eta|<0.5}$) generated by the PYTHIA/Angantyr + UrQMD hybrid model is shown in Fig. 3.1. These predictions are within 20% of the ALICE measurements [102]. To study the effect of rescattering in the hadronic phase, we also ran simulations with hadronic interactions disabled in UrQMD, which led to a difference of no more than 2-3% in charged-particle multiplicity densities. Therefore, it can be concluded that rescattering does not significantly impact this basic observable. The charged-particle multiplicity densities obtained in these simulations are all reproduced in Tab. 3.1.

Another basic observable is the average transverse momentum $\langle p_{\mathrm{T}} \rangle$ and its correlation to the charged-particle multiplicity N_{ch}. This observable provides information to explore

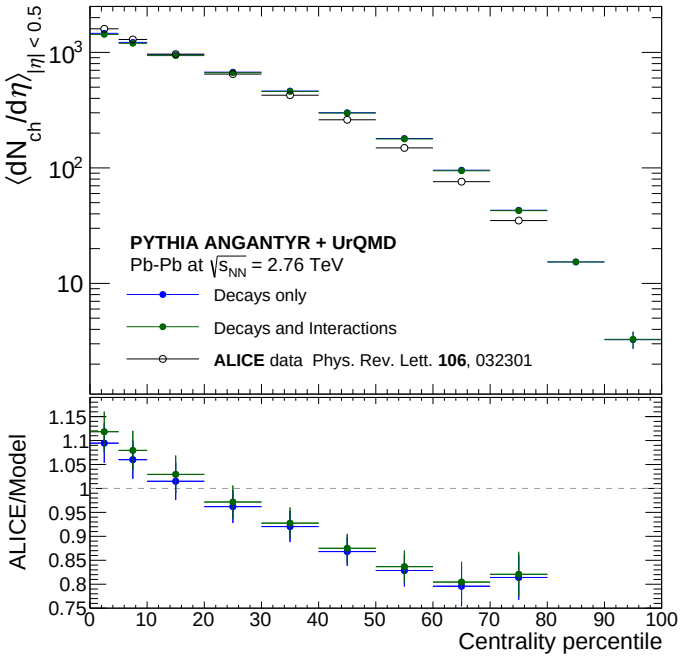

Figure 3.1: Charged-particle multiplicity density at midrapidity ($|\eta| < 0.5$) as a function of event centrality in Pb-Pb collisions at $\sqrt{s_{\rm NN}} = 2.76$ TeV from the PYTHIA/Angantyr + UrQMD simulation chain with $p_{\rm T}$ integrated over the full range for decays only or decays and interactions compared with ALICE data [102]. The vertical lines are the statistical uncertainties in the model and in the data systematic uncertainties.

Table 3.1: Charged-particle multiplicity density versus centrality from the PYTHIA/ Angantyr + UrQMD (decays only or decay and interactions) and the ALICE data with systematic uncertainties [102].

Centrality	$\langle\, {\rm dN_{ch}}/{\rm d}\eta \,\rangle_{\lvert\eta\rvert<0.5}$		
	ALICE	Decays only	Decays and Interactions
$0-5\%$	1601 ± 60	1463 ± 38	1432 ± 38
$5-10\%$	1294 ± 49	1221 ± 35	1200 ± 35
$10-20\%$	966 ± 37	951 ± 31	939 ± 31
$20-30\%$	649 ± 23	674 ± 26	668 ± 26
$30-40\%$	426 ± 15	462 ± 25	459 ± 21
$40-50\%$	261 ± 9	300 ± 17	298 ± 17
$50-60\%$	149 ± 6	179 ± 13	178 ± 13
$60-70\%$	76 ± 4	95 ± 10	94 ± 10
$70-80\%$	35 ± 2	43 ± 7	42 ± 7
$80-90\%$	-	15 ± 4	15 ± 4
$90-100\%$	-	3 ± 2	3 ± 2

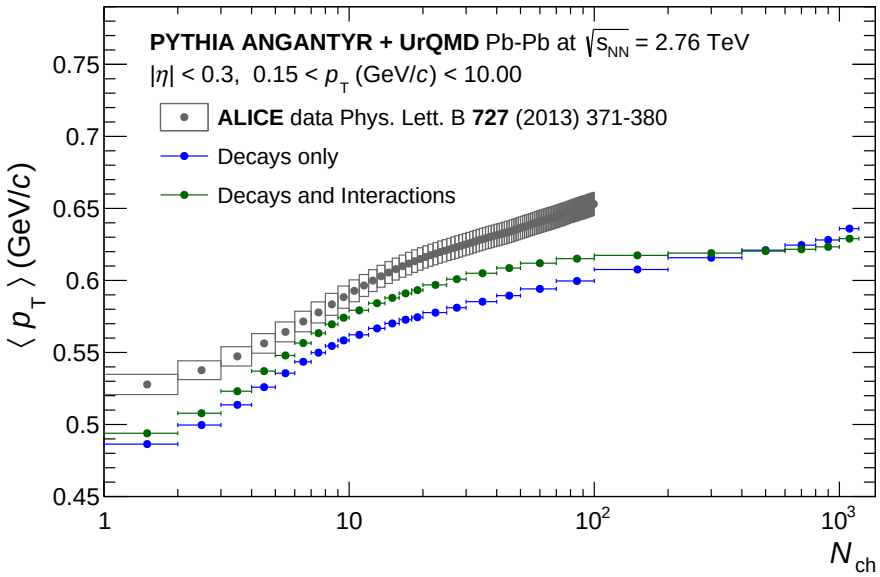

Figure 3.2: Average transverse momentum $\langle p_{\mathrm{T}} \rangle$ at the range $0.15 < p_{\mathrm{T}}$ (GeV/c) 10.00 as a function of the charged-particle multiplicity N_{ch} at midrapidity ($|\eta| < 0.3$) from the PYTHIA/Angantyr + UrQMD hybrid model in Pb–Pb collisions at $\sqrt{s_{\mathrm{NN}}} = 2.76$ TeV compared with the measurements by the ALICE collaboration [103]. In the ALICE data the gray boxes are the systematic uncertainties and statistical uncertainties are negligible, only statistical uncertainties are shown for the model.

the underlying physics phenomena of particle production in small systems and heavy-ion collisions [103]. In proton-proton (pp) collisions, many experiments observed an increase of $\langle p_{\mathrm{T}} \rangle$ with N_{ch} in the mid-rapidity region [35, 104–110]. Mechanisms such as Color Reconnection (CR) [111–113] have been implemented recently in event generators like PYTHIA to reproduce this observable in pp collisions, but these developments have yet to be put in place in the heavy-ion machinery contained in PYTHIA/Angantyr.

We compute the N_{ch}-dependence of the $\langle p_{\mathrm{T}} \rangle$ in the PYTHIA/Angantyr + UrQMD model and obtain the results shown in Fig. 3.2. The model does not really reproduce data well, predicting a smaller $\langle p_{\mathrm{T}} \rangle$ than the measured one. This is likely a consequence of the fact that CR is not fully implemented in PYTHIA/Angantyr. Before comparing to experimental data, I would also mention that the addition of hadronic interactions actually increase the $\langle p_{\mathrm{T}} \rangle$ for peripheral collisions. For completeness, we did $\langle p_{\mathrm{T}} \rangle$ versus event centrality and the results from the PYTHIA/Angantyr + UrQMD are shown in Fig. 3.3 agrees with the results from the hybrid model in Fig. 3.2.

In Tab. 3.2 below, we summarize the $\langle p_{\mathrm{T}} \rangle$ measured by the ALICE collaboration for pp, p–Pb and Pb–Pb collisions at the LHC energies compared with hybrid model predictions for Pb–Pb collisions, i.e., this table allow us to analysis how the $\langle p_{\mathrm{T}} \rangle$ behaviour for small systems and heavy-ion collisions at differents energies. We can conclude that $\langle p_{\mathrm{T}} \rangle$ of

final state particles have a small increase in pp collisions as a function of the energy. An increase is observed from pp to p–Pb to minimum bias Pb–Pb collisions by the ALICE collaboration.

Table 3.2: Average transverse momentum $\langle p_{\mathrm{T}} \rangle$ in pp, p–Pb and Pb–Pb collisions at $\sqrt{s_{\mathrm{NN}}} = 2.76$ TeV with at least one charged-particle with $0.15 < p_{\mathrm{T}}$ (GeV/c) < 10.00 in $|\eta| < 0.3$ for the ALICE data [103] and the PYTHIA/Angantyr + UrQMD hybrid model in Pb–Pb for decays only or decays and Interactions. For the hybrid model we have the statistical uncertainties and for the data are systematic uncertainties.

	collision system	$\sqrt{s_{\mathrm{NN}}}$	$\langle N_{\mathrm{ch}} \rangle$	$\langle p_{\mathrm{T}} \rangle$ (GeV/c)
ALICE	pp	0.9	3.14 ± 0.16	0.540 ± 0.020
	pp	2.76	3.82 ± 0.19	0.584 ± 0.020
	pp	7	4.42 ± 0.22	0.622 ± 0.021
	p–Pb	5.02	11.9 ± 0.5	0.696 ± 0.024
	Pb–Pb	2.76	259.9 ± 5.9	0.678 ± 0.007
Decays only	Pb–Pb	2.76	484.69 ± 0.01	0.61838 ± 0.00002
Decays and Interactions	Pb–Pb	2.76	475.39 ± 0.01	0.61949 ± 0.00002

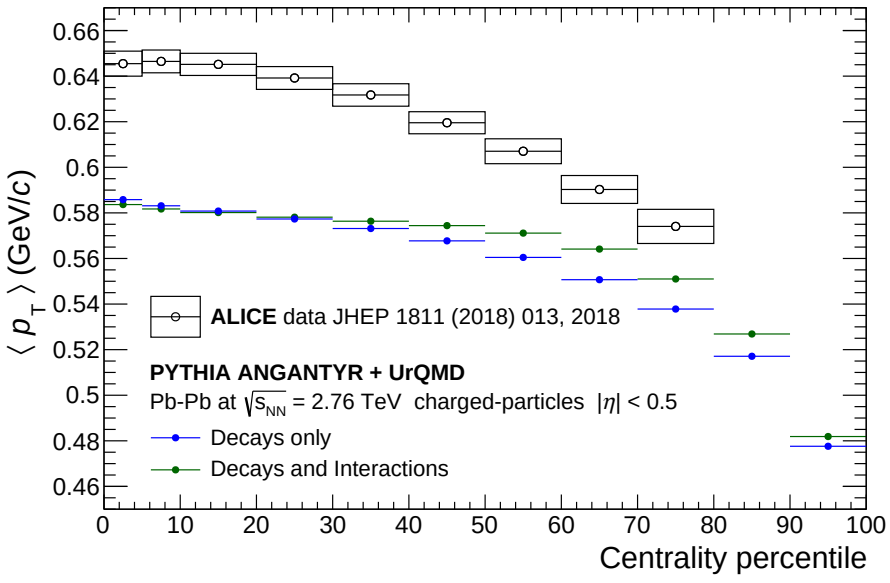

Figure 3.3: Average transverse momentum $\langle p_{\mathrm{T}} \rangle$ for charged-particles at midrapidity $|\eta| < 0.5$ as a function of the event centrality from the PYTHIA/Angantyr + UrQMD hybrid model in Pb–Pb collisions at $\sqrt{s_{\mathrm{NN}}} = 2.76$ TeV and in $|\eta| < 0.5$ compared with the measurements by the ALICE collaboration [114]. In the ALICE data the black boxes are the systematic uncertainties and statistical uncertainties are negligible, only statistical uncertainties are shown for the model.

In conclusion the hybrid model reproduces N_{ch} within 20% and does not describe $\langle p_{\mathrm{T}} \rangle$ fully satisfactorily for known reasons, i.e. the Angantyr model does not include any

effect associated to an isotropic expansion known as 'radial flow' [115]. This effect can build up the mean p_{T}, where heavier particles get a larger boost from the common flow velocity. This will be studied in greater detail in the next section, in which the actual p_{T} distributions will be investigated.

3.2 Transverse momentum distributions

To investigate the effect of rescattering in the hadronic phase we calculate p_{T} distributions as a function of the event centrality with hadronic interactions enabled and disabled, as can be seen in Fig. 3.4. A comparison of the two p_{T} distributions shows that interactions modify the high-p_{T} yields, reducing them with respect to simulations in which interactions are not allowed to happen. This suppression is observed to be significant starting at about $p_{\mathrm{T}} = 4$ GeV/c. The physical interpretation is that high-p_{T} particles lose momentum when interacting with the more abundant low-p_{T} particles created in Pb–Pb collisions.

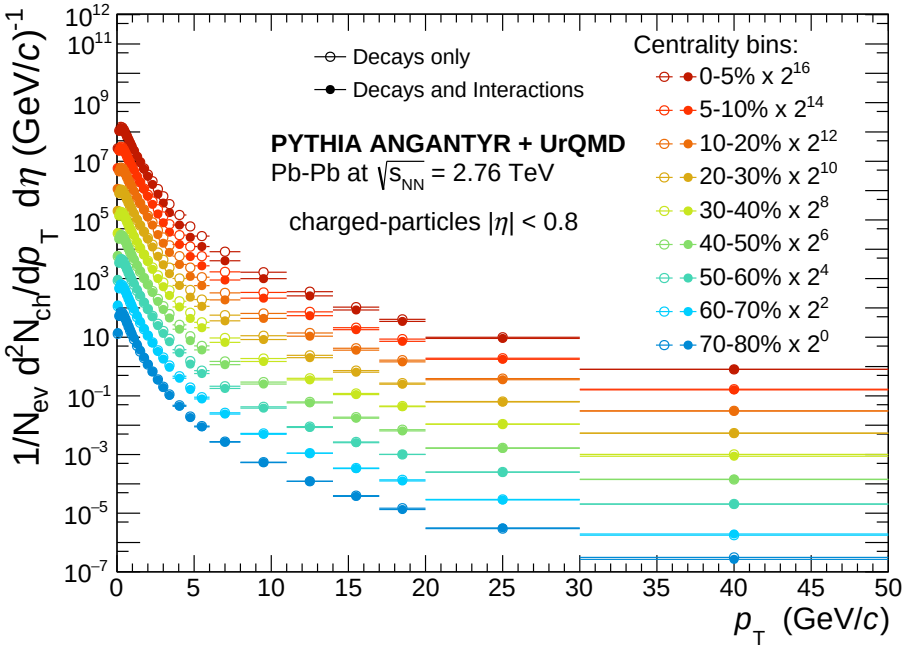

Figure 3.4: Transverse momentum (p_{T}) distributions of charged-particles at midrapidity ($|\eta| < 0.8$) in Pb–Pb collisions at $\sqrt{s_{\mathrm{NN}}} = 2.76$ TeV from the PYTHIA/Angantyr + UrQMD hybrid model for nine centrality classes and with the statistical uncertainties. We use a scale factor for each p_{T} distribution for just separate the curves for better visibility.

The modification of p_{T} spectra can be further studied by calculating the ratio of p_{T} distributions obtained with hadronic interactions to those obtained without interactions,

as shown in Fig. 3.5. In this figure, we can see that the yields are modified by no more than 10-15 % for $p_{\mathrm{T}} < 2$ GeV/c, but the effect of hadronic scattering is more significant at mid- to high-p_{T}, reaching a maximum of to 60% suppression around a $p_{\mathrm{T}} \approx 5$ GeV/c for the $0-5\%$ centrality class.

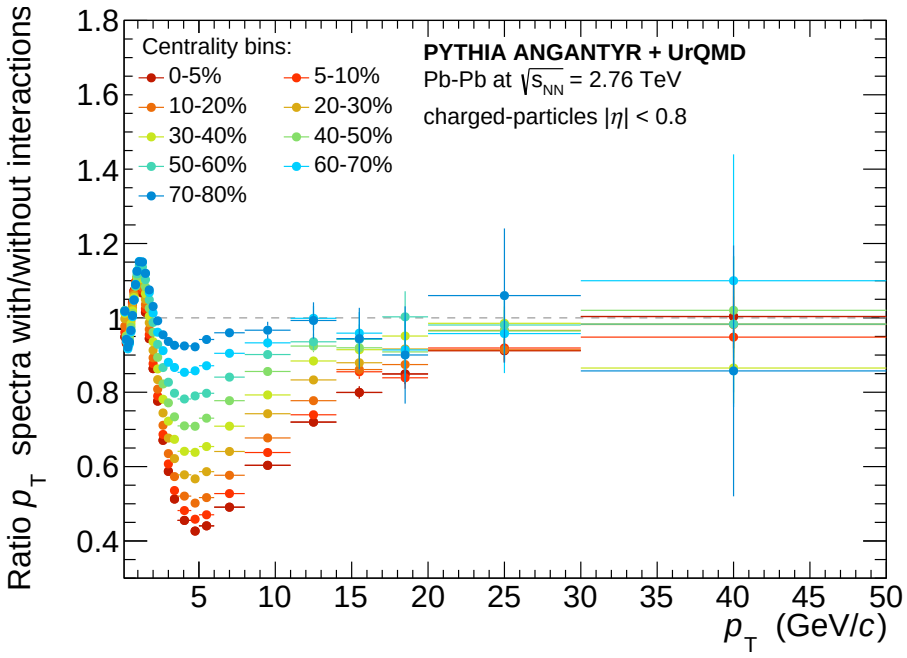

Figure 3.5: Ratio of charged-particle p_{T} distributions at midrapidity ($|\eta| < 0.8$) for decays only and decays and interactions in Pb–Pb collisions at $\sqrt{s_{\mathrm{NN}}} = 2.76$ TeV from the PYTHIA/Angantyr + UrQMD hybrid model for nine centrality classes and the vertical lines for the model are the statistical uncertainties.

The suppression pattern observed in Fig. 3.5 has a momentum dependence that is reminiscent of the nuclear modification factor[1] (R_{AA}), a quantity commonly used to study the spectra of Pb–Pb collisions. We will dedicate the next section to the discussion this observable.

3.2.1 Nuclear modification factor

The suppression of the yields of high-p_{T} particles is quantified by the nuclear modification factor (R_{AA}). The R_{AA} is defined as the ratio of the charged-particle p_{T} spectra in AA collisions compared to pp collisions scaling by the average number of binary nucleon-nucleon (NN) collisions $\langle N_{\mathrm{coll}} \rangle$ which dependence on the centrality.

We calculate the R_{AA} for Pb–Pb collisions at $\sqrt{s_{\mathrm{NN}}} = 2.76$ TeV for the PYTHIA/ Angantyr hybrid model with and without interactions to compare with the ALICE measurements [114], as can be seen in Fig. 3.6. To compute the R_{AA} from the hybrid model, we

[1]For a more detailed explanation of the nuclear modification factor, please refer to section 1.6.1.

generated pp collisions with the same configuration used for Pb–Pb. As a scaling variable, we use the $\langle N_{\rm coll} \rangle$ as a function of the centrality calculated by the ALICE collaboration using the Glauber model [116].

While the R_{AA} obtained without any hadronic interactions does not really reproduce experimental data from ALICE, the addition of hadronic rescattering leads to a proper description of the nuclear modification factor in the intermediate momentum range between 5 – 15 GeV/c for both central and mid-central collision classes.

To verify if the successful description of the measured R_{AA} at high-$p_{\rm T}$ is not accidental, we also calculate the R_{AA} for Xe–Xe collisions at $\sqrt{s_{\rm NN}} = 5.44$ TeV, as shown in Fig. 3.7. The results from the PYTHIA/Angantyr + UrQMD for decays and interactions are within experimental uncertainties for $p_{\rm T} > 6$ GeV/c, in both centralities.

The good agreement of the nuclear modification factor for high-$p_{\rm T}$ particles ($p_{\rm T} > 6$ GeV/c) from the hybrid model is a remarkable result for a model that does not assume QGP formation or a hot and dense thermalized medium, as we discussed in the section 2.3. This is especially notable because in the literature R_{AA} values below unity are one of the key signatures of QGP formation in heavy-ion collisions.

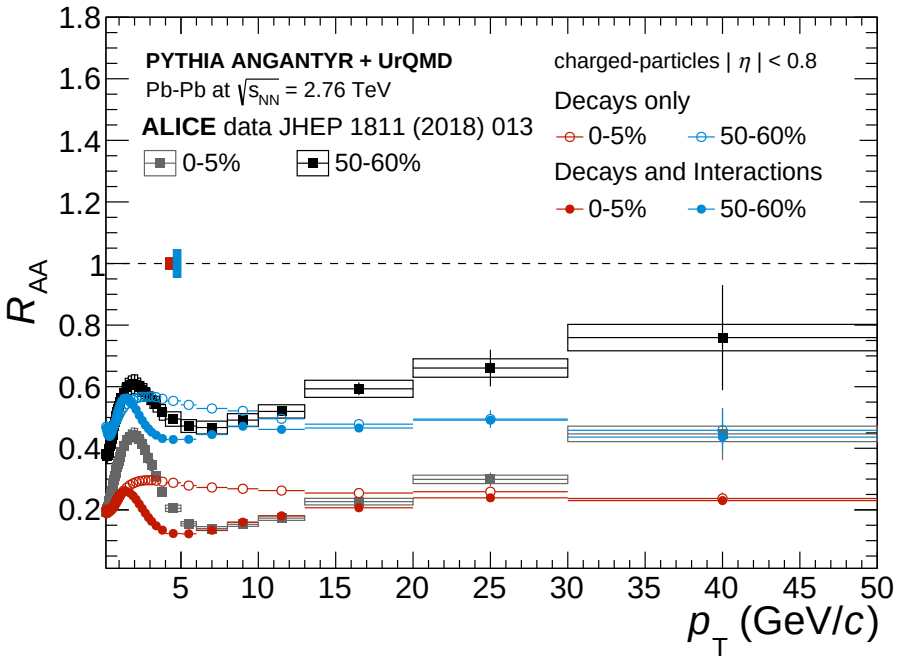

Figure 3.6: Nuclear modification factor R_{AA} in Pb–Pb collisions at $\sqrt{s_{\rm NN}} = 2.76$ TeV for the PYTHIA/Angantyr + UrQMD with decay only or decays and interactions compared to measured by the ALICE collaboration [114], in two centrality classes $0-5\%$ and $50-60\%$. The vertical lines for the hybrid model and the ALICE data are the statistical uncertainties. The gray and black boxes are the systematic uncertainties. The overall normalization uncertainties for the R_{AA} are shown with the red and light blue boxes around unity in both centralities.

It is interesting to note that even without interactions the nuclear modification factor is not at unity for high-p_{T}, which is a consequence of the fact the PYTHIA/Angantyr does not follow binary collision scaling that is in general assumed to hold in the literature [37]. From the model perspective, this is because each subsequent binary collision is not independent from the preceding one, as described in section 2.3.

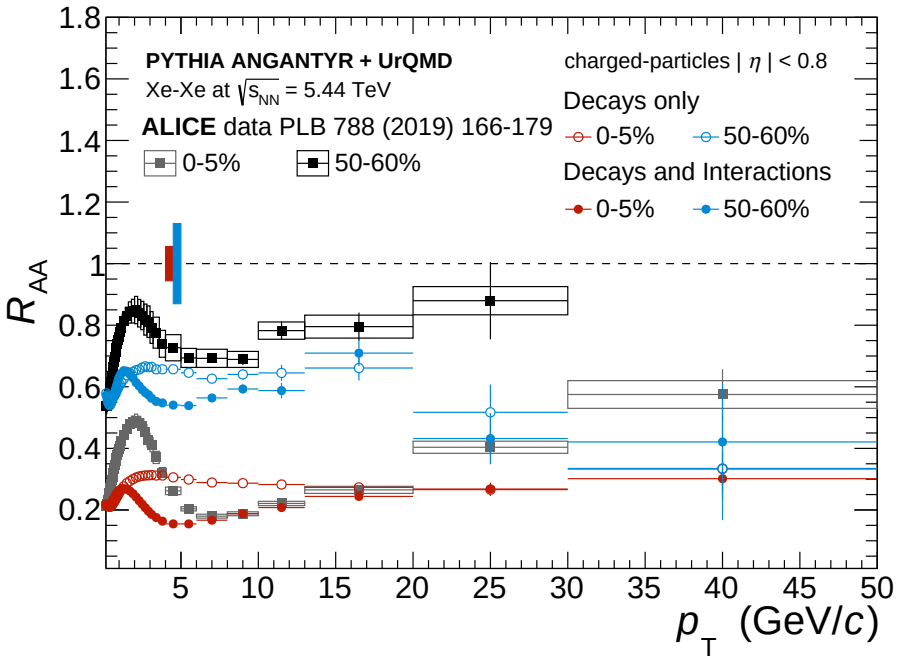

Figure 3.7: Nuclear modification factor R_{AA} in Xe–Xe collisions at $\sqrt{s_{\mathrm{NN}}}$ = 2.76 TeV for the PYTHIA/Angantyr + UrQMD with decay only or decays and interactions compared to measured by the ALICE collaboration [117], in two centrality classes $0-5\%$ and 50-60%. The vertical lines for the hybrid model and the ALICE data are the statistical uncertainties. The gray and black boxes are the systematic uncertainties. The overall normalization uncertainties for the R_{AA} are shown with the red and light blue boxes around unity in both centralities.

Heavy-ion collisions are treated as a superposition of NN binary collisions that are not independent in Angantyr model. Instead, collisions can be classified as elastic, diffractive and non-diffractive inelastic (absorptive), depending on the available energy, and each subcollision will be generated using the standard PYTHIA 8.2 minimum bias machinery. Given that subsequent interactions will have less energy, these will not contribute equally to the high-p_{T} yields, which will, in turn, generate an R_{AA} that is less than unity at high-p_{T}.

However, it is not just the violation of binary scaling that ensures a successful description of the nuclear modification factor: the addition of hadronic rescattering also plays an important role. To better understand the suppression dynamics introduced at high-p_{T}, a deeper look into the hadron vertex is required. In this model, as described in the sections

2.3.1, we know that the medium created in AA collisions is very dense and this fact really influence the high-p_{T} minimum and subsequent rise.

The main suppression effect at around 5 GeV/c comes about because particles having a relatively high momentum are stopped in interactions with other particles produced in the nuclear collision, which on the average carry less than 1 GeV/c. However, at progressively larger p_{T}, yields are less modified: this is because very large momentum particles are produced with a large displacement with respect to the collision region, as can be seen in Fig. 2.6.

In the section 2.3.1 we discussed that, in the hadron vertex model, there is a model uncertainty related to the hadron production position, as cited in Ref. [96]. There are three alternatives to define the hadron creation position denoted as "early", "middle" and "late", with the default setting being "middle". In order to study the effect of this uncertainly, we calculated the R_{AA} also with the early and late options. The light red band shown in Fig. 3.8 marks the region covered if this model ambiguity is to be considered in full. The R_{AA} results with light red band show that the model uncertainty is not within experimental uncertainties for high-p_{T}.

It is important to note that the mechanism leading to high-p_{T} yield suppression in this work is fundamentally different than the one traditionally used to explain the nuclear modification factor. In the usual approach, energy loss and jet quenching [118] take place mostly in the partonic, rather than hadronic, phase. In order to study the effect seen in this work further, the next section will elaborate on the study of jet quenching using two-particle angular correlations [45].

3.3 Jet quenching in the hadronic phase

The jet quenching is one experimental signature for QGP formation by the strong suppression of high-p_{T} jets with energy loss traversing a hot and dense QCD matter created in heavy-ion collisions. In the literature, the jet quenching phenomenology has focused especially in modelling the strong interaction of partons with deconfined matter of quarks and gluons, the QGP medium [119–121]. After the initial stage, we know that the system created evolves and cools down until it reaches a temperature that is sufficiently low for a transition to hadronic matter to occur. The hadronic phase has been successfully

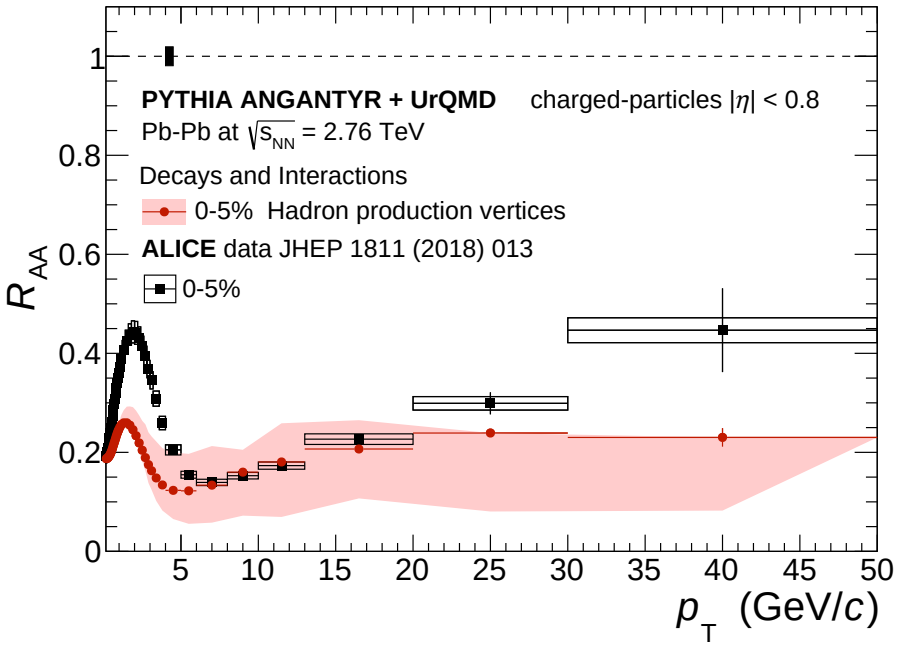

Figure 3.8: Nuclear modification factor R_{AA} in Pb–Pb collisions at $\sqrt{s_{\rm NN}}$ = 2.76 TeV for the PYTHIA/Angantyr + UrQMD with decays and interactions compared to measured by the ALICE collaboration [114] in the centrality class $0-5\%$. The vertical lines for the hybrid model and the ALICE data are the statistical uncertainties, and the black box is the systematic uncertainties for the ALICE measurements. The light red band shown around the R_{AA} (red points) is an uncertainty from the hadron vertex model due to the three different options to calculate hadron production vertices in the Lund string model, known as early, middle (default) and late. The overall normalization uncertainty for R_{AA} is shown as a vertical black box around unity.

described by the dynamics of hadron gas using a hadronic transport approach, e.g., the UrQMD model. So far, a significant part of the jet quenching studies does not include the effect of rescattering in the hadronic phase.

In the following, we are going to apply the two-particle correlations technique to events generated with PYTHIA/Angantyr + UrQMD to study how the jets interact with the hadronic phase in Pb–Pb collisions.

3.3.1 Two-particle correlation analysis

The use of the two-particle correlations (2PC) method allows us to study in more details the high-$p_{\rm T}$ yield suppression observed in our hybrid model. We calculate the correlation function C($\Delta\phi$, $\Delta\eta$) for a high-$p_{\rm T}$ trigger and associated particles to investigate the maximum suppression observed in Fig. 3.5 and therefore choose the $p_{\rm T}$ ranges of $6 < p_{\rm T}^{\rm trigger}$ (GeV/c) < 8 and $4 < p_{\rm T}^{\rm assoc}$ (GeV/c) < 6 for this study. The $C_{\rm correct}(\Delta\phi, \Delta\eta)$ was calculated as discussed in Sec.1.6.2, where the events are mixed only if the difference in centrality is of no more than 2%, with approximately 2000 events being used for the

mixing. The uncorrelated background was estimated by using the event mixing technique within $|\eta| < 2.5$. To estimate the uncorrelated background (bkg) for the $C_{\rm correct}(\Delta\phi, \Delta\eta)$ we use the event mixing method but consider all angles to be relative to the event plane (EPs), i.e. the particles are aligned to the EPs to calculate the $C_{\rm mix}^{\rm aligned\ EP}(\Delta\phi, \Delta\eta)$ and also compute the $C_{\rm mix}(\Delta\phi, \Delta\eta)$ to correct the limitation for the pair acceptance. The $C_{\rm bkg}(\Delta\phi, \Delta\eta)$ can be defined as:

$$C_{\rm bkg}(\Delta\phi, \Delta\eta) = \frac{\beta \times C_{\rm mix}^{\rm aligned\ EP}(\Delta\phi, \Delta\eta)}{\alpha \times C_{\rm mix}(\Delta\phi, \Delta\eta)}, \tag{3.1}$$

where the α is used to normalize the $C_{\rm mix}(\Delta\phi, \Delta\eta)$ to be unity at $\Delta\eta = 0$. The β is a normalisation to adjust imperfections in the background estimated by the event mixed method. We calculate the factor β for the particle yields from $C_{\rm bkg}(\Delta\phi, \Delta\eta)$ and $C_{\rm correct}(\Delta\phi, \Delta\eta)$ to match in the near-side region away from the peak in the ranges $1.0 < \Delta\eta < 4.0$ and $|\Delta\phi| < \pi/2$. Now the final correlation function with the subtraction of the background can be written as:

$$C(\Delta\phi, \Delta\eta) = C_{\rm correct}(\Delta\phi, \Delta\eta) - C_{\rm bkg}(\Delta\phi, \Delta\eta). \tag{3.2}$$

This subtraction effectively removes the entire uncorrelated background in the associated particle distribution $C_{\rm correct}(\Delta\phi, \Delta\eta)$. High-order corrections to this subtraction technique were tested and are negligible for this study. We apply this method to calculate the correlation function projected $C(\Delta\phi)$ for three centrality classes, as can be seen in Fig. 3.9. From this result we can see a significant small suppression of the away-side jet structure when hadronic interactions are enabled for the most central collisions and the near-side peak is less affected from central to peripheral collisions. We understand that the trigger particles are more likely to be close to the edge of the system leaving with less interactions, while the away-side jet will undergo multiple interactions with the hadronic medium.

This effect observed in our hybrid model remember the measurements realized by STAR collaboration at RHIC, where was observed a full away-side jet suppression in central Au–Au collisions [46] by using the two-particle correlation to study dijets, as showed in Sec. 1.6. The STAR result was interpreted that the trigger particles are far away from the center of the collision and the away-side jet are suppressed due to

multiple partonic interactions in the travel through the QGP medium more than hadronic interactions. Our hybrid model is capable to reach a small away-side jet suppression, but it is important to note that model shows a significant result considering an improved no-QGP baseline.

We calculate the magnitude of the yield modification in the away-side as a function of centrality by integrating the correlation function C($\Delta\phi$, $\Delta\eta$) with the background-subtracted, as showed in Eq. (3.2), with hadronic interactions disabled and enabled to do the ratio between them that are show in Fig. 3.10. We can see that the near-side jet does not show a centrality dependence, but the away-side jet does with a maximum suppression of approximately 30% for the most central Pb–Pb collisions, centrality of $0-5\%$.

In our hybrid model we also can explore the average number of hadronic collisions $\langle N_{coll}^{hadronic} \rangle$ as a function of $\Delta\phi$ as shown in Fig. 3.11. From this result we understand that the $\langle N_{coll}^{hadronic} \rangle$ is much smaller in the near-side around $\Delta\phi = 0$ with jets leaving the system practically without interacting compared to jets in the away-side region around $\Delta\phi = \pi$,in which case outgoing particles have a significant probability to interact with the hadronic medium produced in our simulations.

In Fig. 3.12, we show the correlation function calculated for PYTHIA/Angantyr + UrQMD in Pb–Pb collisions at $\sqrt{s_{NN}} = 2.76$ TeV, with hadronic interactions disabled and enabled by the UrQMD model in the Fig. 3.12a and Fig. 3.12b, respectively. We select charged-particles for the trigger and associated with p_T ranges of $2.0 < p_T^{trigger}$ (GeV/c) < 10.0 and $2.0 < p_T^{assoc}$ (GeV/c) < 4.0, with these p_T ranges we can investigate one source of long-range angular correlation known as "elliptic flow". The correlation function for PYTHIA/Angantyr + UrQMD allows us to study the model predictions for the observables associated to correlations in heavy-ion collisions. The results in Fig. 3.12b show that when hadronic interactions are enabled we can observe a double-ridge structure that is not present without interactions in Fig. 3.12a. This source contributes with a term cos(2$\Delta\phi$) to the two-particle correlation function over a long $\Delta\eta$ range [65]. The observable elliptic flow have been extensively studied over a wide range of energies and collision system by the experiments at RHIC [4, 7, 122] and LHC [59, 75, 123].

In a following section, we are going to explore in more details the elliptic flow observed in the PYTHIA/Angantyr + UrQMD hybrid model.

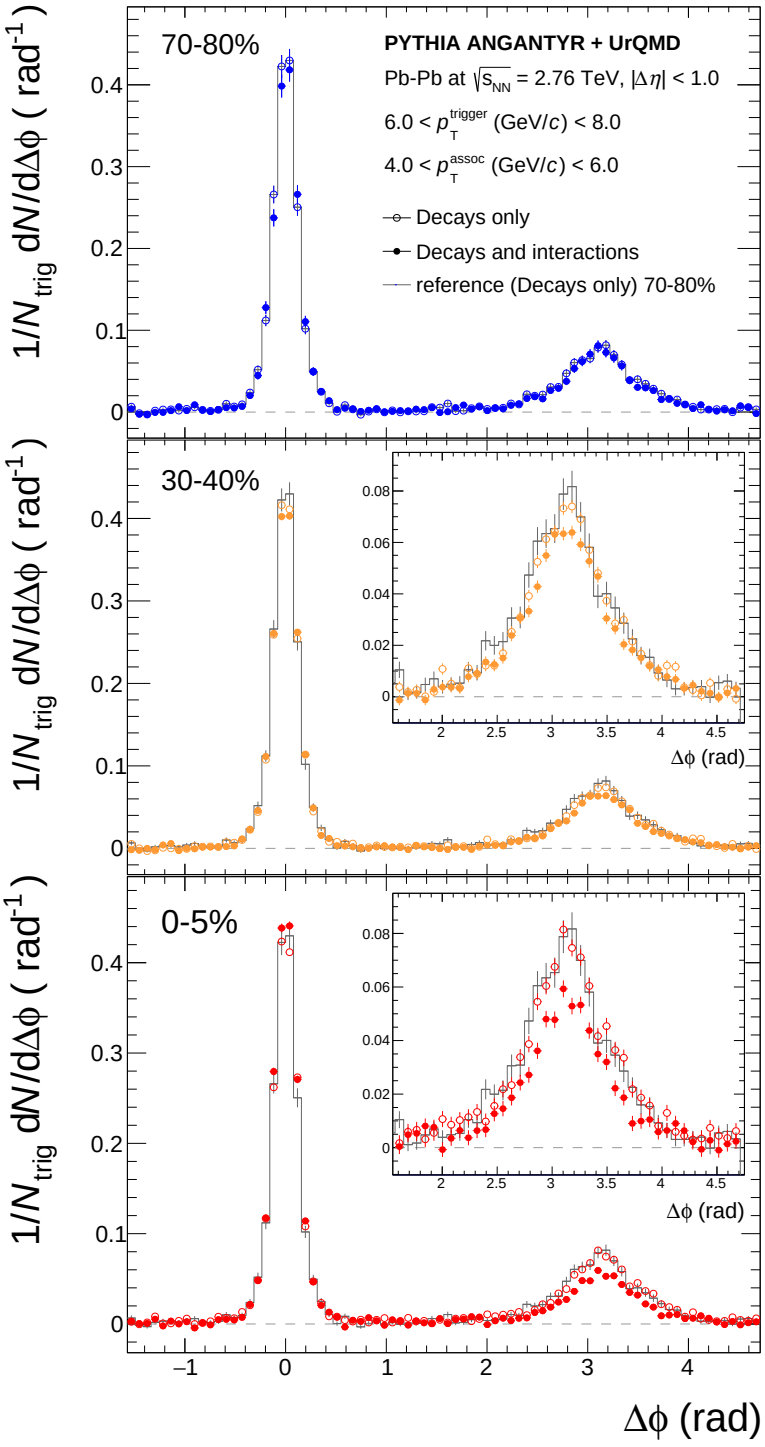

Figure 3.9: Correlation function projected in $\Delta\phi$ with $|\Delta\eta| < 1.0$ for the PYTHIA/ Angantyr hybrid model in Pb–Pb collisions at $\sqrt{s_{\rm NN}} = 2.76$ TeV, selecting the $p_{\rm T}$ ranges of $6 < p_{\rm T}^{\rm trigger}$ (GeV/c) < 8 and $4 < p_{\rm T}^{\rm assoc}$ (GeV/c) < 6 to the trigger and associated charged-particles, respectively. The figures are for three centrality classes on (Bottom) $0-5\%$ (most central collisions), $30-40\%$ (mid-central collisions) and $70-80\%$ (peripheral collisions) for decays only and decays and interactions. The gray distributions are the same in the top, middle and bottom of the figure, being a reference $(70-80\%)$ with interactions disabled. The vertical lines are statistical uncertainties in the points from our simulations.

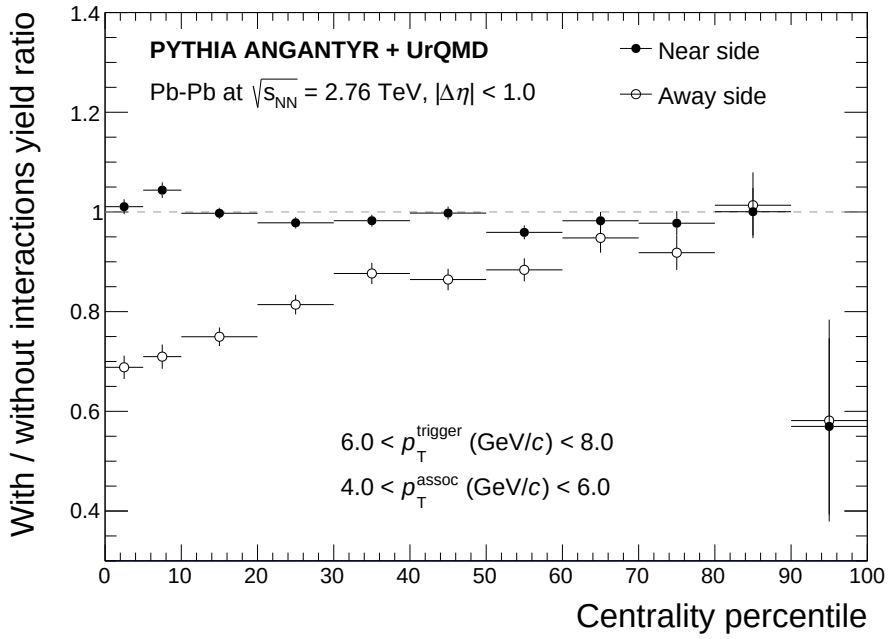

Figure 3.10: Ratio yield with/without interactions for the near and away side as a function of centrality for the PYTHIA/Angantyr + UrQMD in Pb–Pb collisions at $\sqrt{s_{\rm NN}} = 2.76$ TeV. The vertical lines are statistical uncertainties.

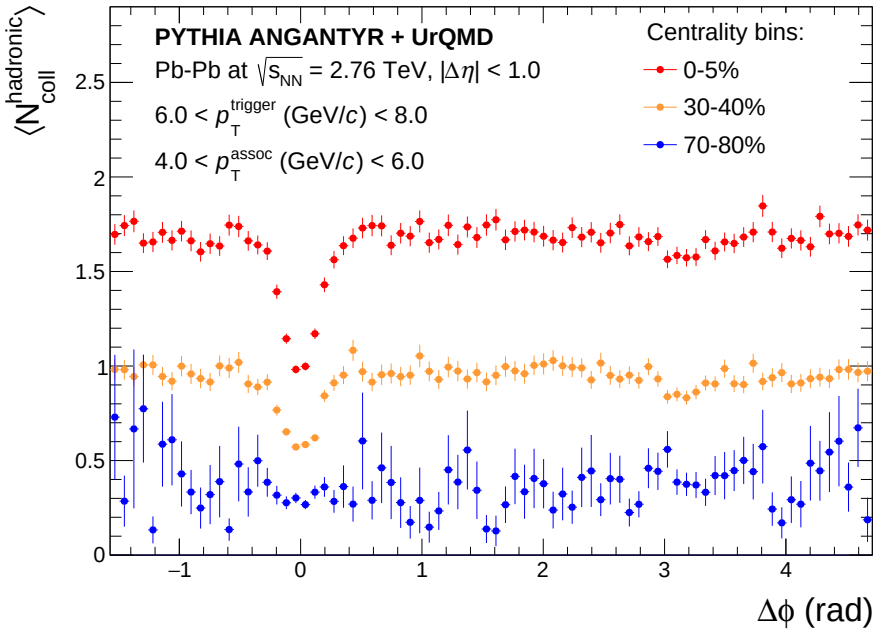

Figure 3.11: Average number of hadronic interactions as a function of $\Delta\phi$ for PYTHIA/ Angantyr + UrQMD in Pb–Pb collisions at $\sqrt{s_{\rm NN}} = 2.76$ TeV in three centrality classes. The vertical lines are statistical uncertainties.

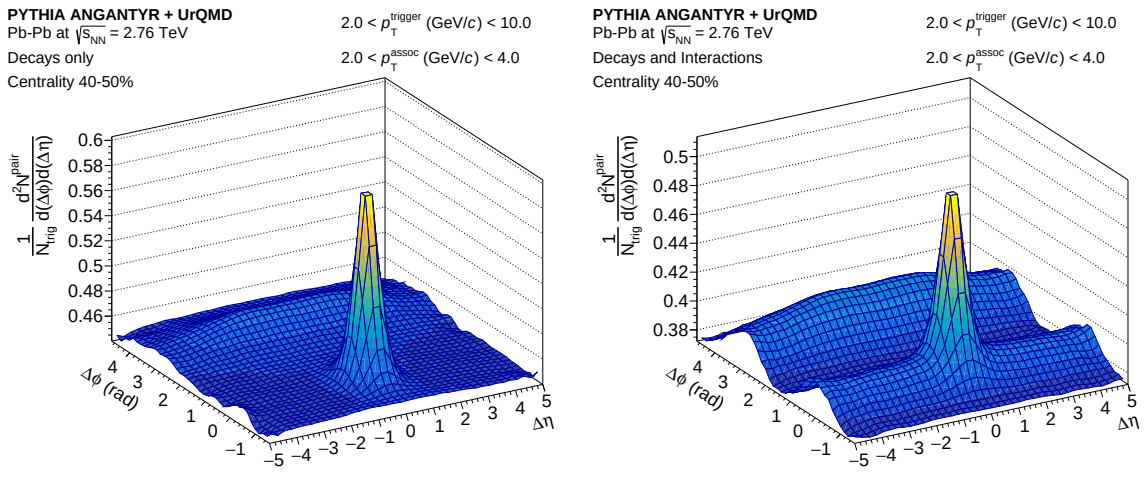

(a) **(b)**

Figure 3.12: The two-particle correlation function calculated for the PYTHIA/Angantyr + UrQMD in Pb–Pb collisions at $\sqrt{s_{\rm NN}} = 2.76$ TeV, selecting the trigger and associated charged-particles for the centrality bin $40 - 50\%$ in the figures **(a)** and **(b)** for decay only and decays and interactions, respectively.

3.4 Elliptic flow

In practice, the v_2 cannot be measured directly by the experiments because the reaction plane angle is not a direct observable. The usually way to estimate the flow coefficients are using azimuthal correlations between the observed particles known as cumulants method [72, 124]. We know that elliptic flow is related with the initial geometry of the collision, this fact suggests to investigate the dependence with event centrality.

3.4.1 Centrality dependence

The current version of the PYTHIA/Angantyr model [63] does not include collective flow in the final state. In the absence of initial hadronic flow, this model serves as a very important baseline in which there was no QGP. To calculate the elliptic flow, we did the azimuthal distribution of charged-particles with respect to the event plane shown in Fig. 3.13, for events generated by the PYTHIA/Angantyr + UrQMD in Pb–Pb collisions at $\sqrt{s_{\rm NN}} = 2.76$ TeV. Curves for simulations in which hadronic interactions are disabled and enabled are both shown in this figure.

Analyzing the plots shown in the Fig. 3.13, we can observe that the distribution for decays only does not show a modulation, but this is different for decays and interactions, with a clear modulation, where more particles are emitted in the direction of the reaction plane, in $\Delta\phi = 0$ and $\Delta\phi = \pi$. This modulation is the elliptic flow in this hybrid model.

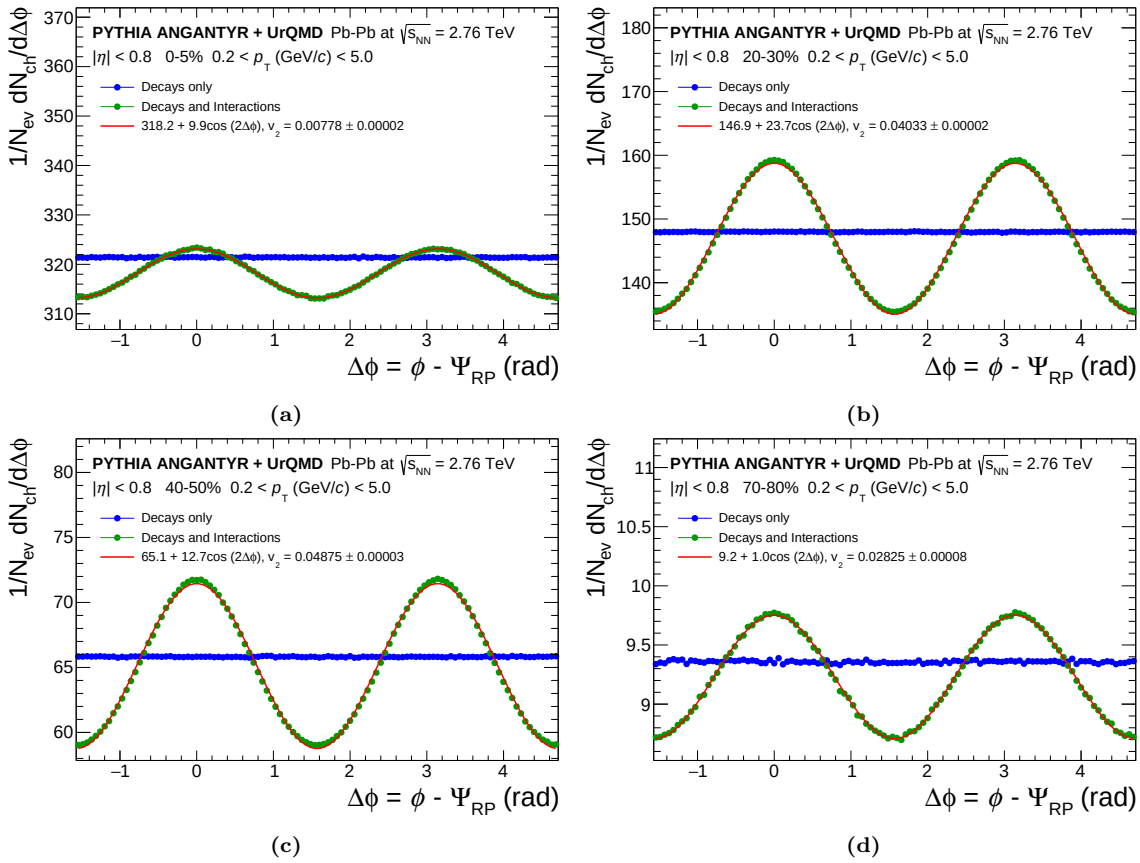

Figure 3.13: Azimuthal distribution of charged-particles $(1/\mathrm{N_{ev}})\mathrm{dN_{ch}}/\mathrm{d}\Delta\phi$, where $\Delta\phi = \phi - \Psi_{\mathrm{RP}}$ is the azimuth angle (ϕ) with respect to reaction plane angle (Ψ_{RP}), in $|\eta| < 0.8$ and $0.2 < p_{\mathrm{T}}$ (GeV/c) < 5.0. These distributions are events generated by the PYTHIA/Angantyr + UrQMD in Pb–Pb collisions at $\sqrt{s_{\mathrm{NN}}} = 2.76$ TeV, normalized by the number of events ($\mathrm{N_{ev}}$) for decay only and decay and interactions. Each figure for one centrality: $0-5\%$ **(a)**, $20-30\%$ **(b)**, $40-50\%$ **(c)** and $70-80\%$ **(d)**. The red curve represent the fit by one function $\cos(2\Delta\phi)$ that is used to calculate v_2.

When we add the UrQMD model to simulate the rescattering in the hadronic phase, we can see the effect known as elliptic flow (v_2) that would be one signature for the QGP formation, but this effect in the model is associated with initial geometry. In this case, the initial geometry of the collision is converted to elliptic flow not via partonic but rather via hadronic interactions.

To establish the centrality dependence of v_2, we calculate the v_2 as a function of collision centrality for the PYTHIA/Angantyr + UrQMD event generator in Pb–Pb collisions at $\sqrt{s_{\mathrm{NN}}} = 2.76$ TeV with rescattering disabled and enabled. We compare the model predictions with measurements by the ALICE collaboration, as can be seen in Fig. 3.14. The elliptic flow was calculated by two different methods for the model, the first method v_2 by fitting (v_2^{Fit}) the azimuthal distribution and the second method by the multi-particle correlation, denoted as $v_2\{2\}$ and $v_2\{4\}$, for the 2- and 4- particle correlations, respectively. For more details about 2- and 4- particle correlations see the section 1.7.1.

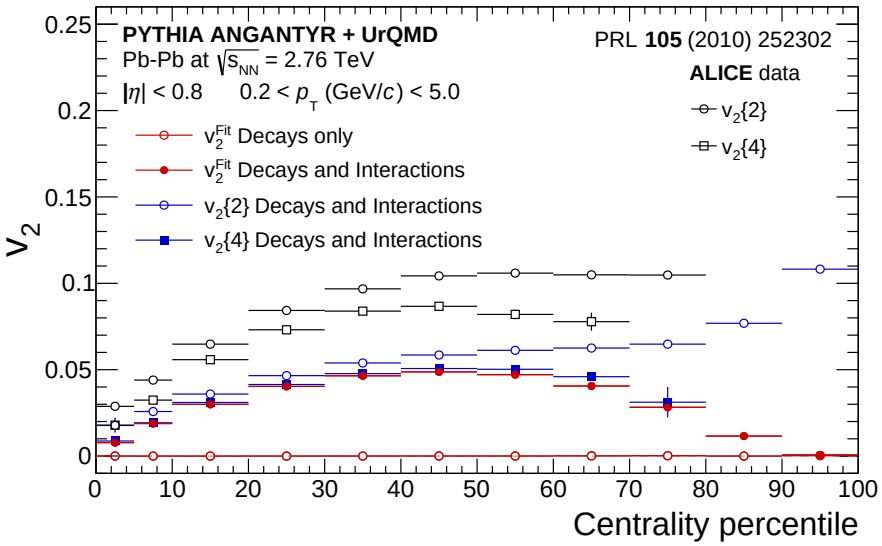

Figure 3.14: Elliptic flow v_2 integrated over p_{T} range $0.2 < p_{\mathrm{T}}$ (GeV/c) < 5.0, as a function of event centrality for the PYTHIA/Angantyr + UrQMD in Pb–Pb collisions at $\sqrt{s_{\mathrm{NN}}} = 2.76$ TeV. For the model we calculate v_2^{Fit} with decays only or decays and interactions, and also using 2- and 4- particle cumulants [42], $v_2\{2\}$ and $v_2\{4\}$, respectively, for charged-particles in $|\eta| < 0.8$. We compare the predictions for v_2 from the hybrid model with ALICE data [75].

From the results shown in Fig. 3.14, the v_2^{Fit} with hadronic interaction enabled can reproduce around 60% of magnitude the one measured by the ALICE collaboration. The v_2 found is consistent with simulation results obtained before, at lower energies [125]. We also found similar results for $v_2\{2\}$ and $v_2\{4\}$ compared with the ALICE data. The $v_2\{2\}$ is greater than $v_2\{4\}$ because it is more affected by the non-flow contributions like resonance decays and jet correlations. See v_2 values from our hybrid model compared to the ALICE data in Tab. 3.3.

The v_2^{Fit} calculated with hadronic interactions disabled is practically zero, as can be seen in Fig. 3.14. In the next section, we calculate the p_{T} dependence of elliptic flow using the two methods described above and compared with experimental data.

3.4.2 Transverse momentum dependence

We compute the p_{T}-differential elliptic flow $v_2(p_{\mathrm{T}})$ for the PYTHIA/Angantyr + UrQMD hybrid model in Pb–Pb collisions at $\sqrt{s_{\mathrm{NN}}} = 2.76$ TeV. From this we compare the $v_2^{\mathrm{Fit}}(p_{\mathrm{T}})$ from model with and without hadronic interactions to the measured by the ALICE collaboration, as can be seen in Fig. 3.15. As observed, the $v_2^{\mathrm{Fit}}(p_{\mathrm{T}})$ calculated increases with transverse momentum until reach a maximum at $p_{\mathrm{T}} = 3$ GeV/c and after this point start to decrease at high-p_{T}, in both centrality classes. We also calculate the

Table 3.3: Elliptic flow as a function of event centrality from the PYTHIA/Angantyr + UrQMD hybrid model in Pb–Pb collisions at $\sqrt{s_{\mathrm{NN}}} = 2.76$ TeV compared with ALICE data [75]. The values for v_2 in this table are from the plot in Fig. 3.14.

	ALICE		Model		
Centrality	$v_2\{2\}$	$v_2\{4\}$	$v_2\{2\}$	$v_2\{4\}$	v_2^{Fit}
$0-5\%$	0.0288 ± 0.0005	0.0179 ± 0.0043	0.01767 ± 0.00003	0.0085 ± 0.0008	0.0077
$5-10\%$	0.0440 ± 0.0005	0.0324 ± 0.0017	0.02577 ± 0.00003	0.0192 ± 0.0001	0.0188
$10-20\%$	0.0648 ± 0.0004	0.0557 ± 0.0009	0.03589 ± 0.00002	0.0310 ± 0.0001	0.0299
$20-30\%$	0.0843 ± 0.0005	0.0731 ± 0.0011	0.04651 ± 0.00003	0.0414 ± 0.0001	0.0403
$30-40\%$	0.0968 ± 0.0006	0.0839 ± 0.0012	0.05388 ± 0.00003	0.0477 ± 0.0001	0.0464
$40-50\%$	0.1043 ± 0.0008	0.0867 ± 0.0018	0.05854 ± 0.00004	0.0507 ± 0.0001	0.0487
$50-60\%$	0.106 ± 0.001	0.082 ± 0.003	0.06113 ± 0.00006	0.0502 ± 0.0003	0.0471
$60-70\%$	0.1049 ± 0.0013	0.0778 ± 0.0052	0.06240 ± 0.00009	0.0456 ± 0.0009	0.0406
$70-80\%$	0.1048 ± 0.0023	-	0.0645 ± 0.0002	0.035 ± 0.007	0.0282
$80-90\%$	-	-	0.0765 ± 0.0004	-	0.0115
$90-100\%$	-	-	0.1082 ± 0.0013	-	0.0009

$v_2\{2\}$ and $v_2\{4\}$ (see Fig. 3.15) shown the same dynamic of v_2^{Fit} at low-p_{T}, but comparing v_2^{Fit} and $v_2\{2\}$ the distributions start to diverge around $p_{\mathrm{T}} \approx 1$ GeV/c. As previously observed with the integrated flow, $v_2\{4\}$ mirrors v_2^{Fit} very closely, while $v_2\{2\}$ is higher than $v_2\{4\}$. This is because also in this case non-flow contributions affect the $v_2\{2\}$, but $v_2\{4\}$ is less affected. The fact that $v_2\{4\}$ matches v_2^{Fit} means that $v_2\{4\}$ show one possible correlation with the event plane.

In the results shown in Fig. 3.15, we observed that p_{T}-differential v_2^{Fit} and $v_2\{4\}$ from the model can describe approximately 60% of magnitude of the v_2 measured by the ALICE collaboration. For completeness, the $v_2(p_{\mathrm{T}})$ calculated from fit with hadronic interactions disabled is practically zero, as we found before for the integrated v_2.

Therefore, we found a strong signal for collective effects in this new hybrid model, more specifically the elliptic flow v_2 in the hadronic phase. The question that remains at this point is how much flow would have to be present at the hadronization stage to lead to the measured flow, given that UrQMD is capable of adding extra flow post-hadronization. This question will be investigated in the next section.

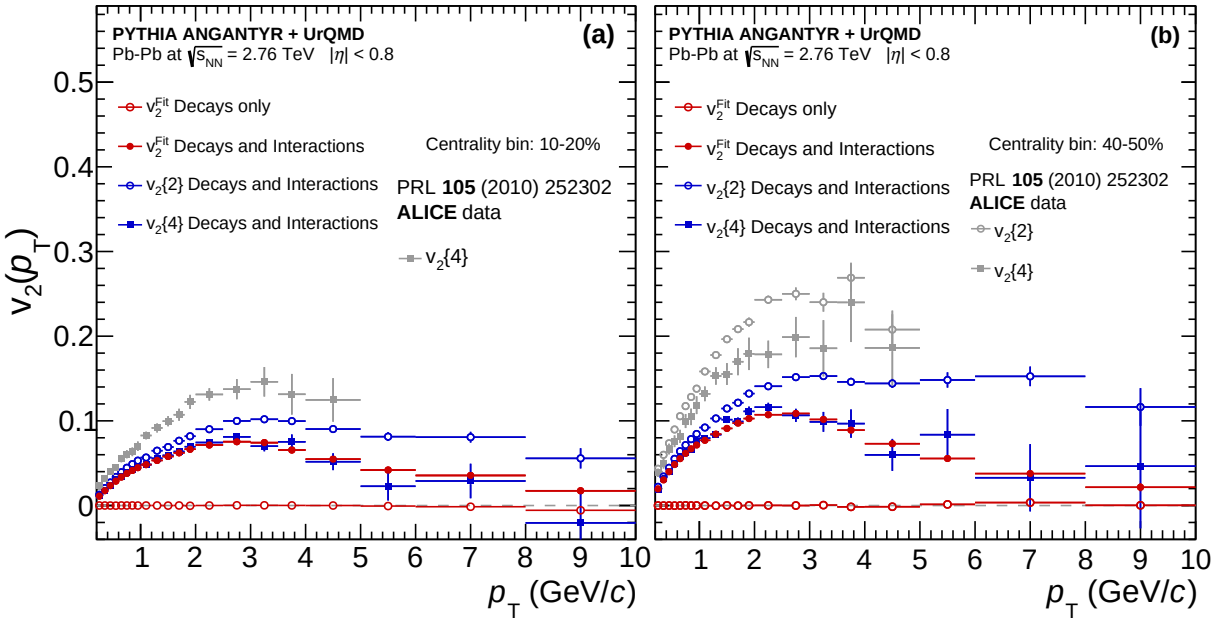

Figure 3.15: p_{T}-differential elliptic flow v_2 as a function of transverse momentum p_{T} for the PYTHIA/Angantyr + UrQMD in Pb–Pb collisions at $\sqrt{s_{\mathrm{NN}}} = 2.76$ TeV. For the model we calculate v_2^{Fit} with decays only or decays and interactions, and also using 2- and 4-particle cumulants [42], $v_2\{2\}$ and $v_2\{4\}$, respectively, for charged-particles in $|\eta| < 0.8$. We compare the predictions for v_2 from the model with the ALICE data for two centrality classes, $10-20\%$ **(a)** and $40-50\%$ **(b)** [75].

3.4.3 Toy model

Now we present a simple toy model to introduce an initial hadronic flow (v_2^{initial}) to the PYTHIA/Angantyr event generator after hadronization. The results shown in the sections 3.4.1 and 3.4.2 our hybrid model is capable to describe approximately 60% of the v_2 measured by the ALICE collaboration [75]. Given that we know that UrQMD has the ability to add flow and that we are missing 40% of the measured v_2, it might be that the v_2 immediately after hadronization need not be as large as the one measured by ALICE. In this section, we investigate how UrQMD responds to various conditions of post-hadronization flow to explore this question in more detail.

The basic idea to introduce v_2^{initial} to PYTHIA/Angantyr is to do the rotation of the transverse momentum (p_{T}) of the particles in the transverse plane ($x-y$) immediately after hadronization. We describe this idea in Fig. 3.16, where we have the distribution of hadron positions for one Pb–Pb collision event generated by PYTHIA/Angantyr at $\sqrt{s_{\mathrm{NN}}} = 2.76$ TeV for the centrality of $40-50\%$. It is important to note that the point here is really not about hacking the PYTHIA/Angantyr event generator, but rather to explore UrQMD response quantitatively.

To generate the v_2^{initial} we need to do the parametrization for $v_2(p_T)$ with respect to reaction plane. Using this parametrization we can manually set the $v_2(p_T)$ with the p_T-dependence times a 'flow parameter A' that can be changed systematically to increase the $v_2(p_T)$. We did the parametrization based on the result from v_2^{Fit} shown in Fig. 3.15(b) with hadronic interactions enabled in the hybrid model, and we can see the parametrization in Fig. 3.17. The parameterized function chosen for this is:

$$v_2(p_T) = \text{A}\frac{0.100p_T}{1 + 0.315p_T(1 + 0.112p_T^2)}. \tag{3.3}$$

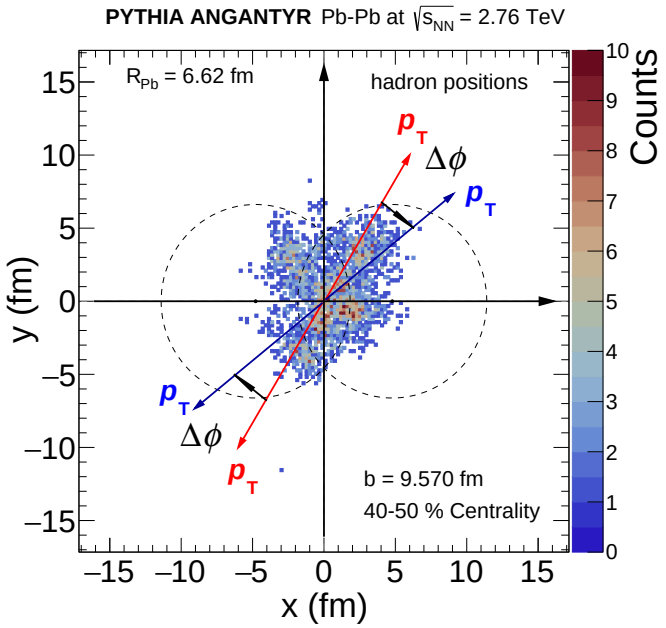

Figure 3.16: Distribution of hadron positions in $x - y$ for one event generated by PYTHIA/ Angantyr in Pb–Pb collisions at $\sqrt{s_{\text{NN}}} = 2.76$ TeV after hadronisation for the centrality bin $40 - 50\%$ (Impact parameter b = 9.570 fm). In non-central collisions, the interaction region in the transverse plane turns out to be almond-shaped where the two nuclei overlap and each nucleus is represented by the dash circle (with Radius of the nucleus Lead (Pb) $R_{\text{Pb}} = 6.62$ fm), with the reaction plane rotated to y = 0. In figure we describe the rotate of p_T from red arrow to the blue arrow to introduce an initial hadronic flow.

We use the Eq. (3.3) with an *inverse transform sampling* [2], Basically, we perform the transformation of the uniform azimuthal distribution generated by PYTHIA/Angantyr after hadronization to an azimuthal distribution with the modulation, so that we introduce v_2^{initial}. In Fig. 3.18 we show the modulation of the azimuthal distribution for four values of the flow parameter A and we can see how v_2^{initial} scales up as intended, with a realistic momentum dependence when we change the parameter A manually.

[2] This is a method to transform any probability distribution by using random number sampling by the inverse of the cumulative distribution function [126].

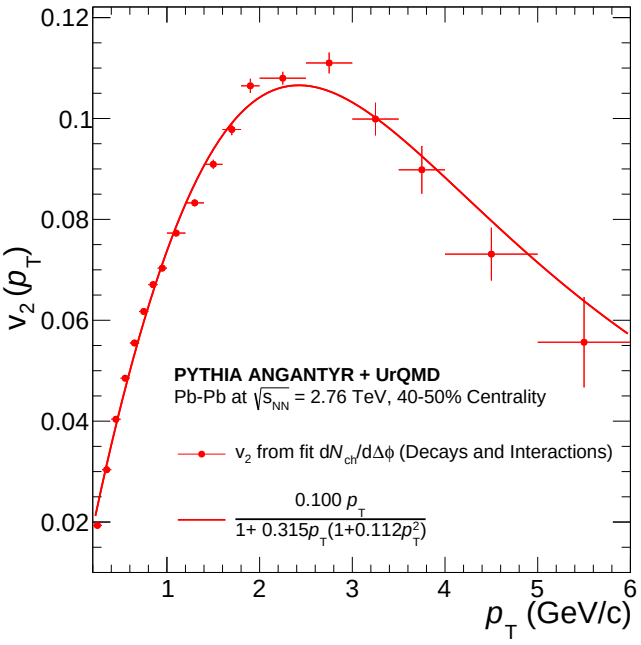

Figure 3.17: p_{T}-differential elliptic flow v_2 as a function of transverse momentum p_{T}, for the PYTHIA/Angantyr + UrQMD in Pb–Pb collisions at $\sqrt{s_{\mathrm{NN}}} = 2.76$ TeV, calculated from fit of the azimuthal distribution $\mathrm{d}N_{\mathrm{ch}}/\mathrm{d}\Delta\phi$ for decays and interactions in the centrality bin $40-50\%$. We fitting one function to $v_2(p_{\mathrm{T}})$ points given by the Eq. (3.3).

Now we are in a position to study systematically what happens with the final hadronic flow (v_2^{final}) when we change the v_2^{initial} using the toy model. The idea is to increase the v_2^{initial} by changing the flow parameter A until the v_2^{final} reaches the value measured by the ALICE collaboration. A schematic representation of this idea can be seen in Fig. 3.19. For this study we did 11 configurations (or 11 values for the flow parameter A) for the v_2^{initial}. We feed the 11 initial flow configurations to UrQMD with hadronic rescattering enabled to generate 11 final flow configurations and then study how the v_2^{final} correlates to v_2^{initial}.

From the results shown in Fig. 3.20 we can understand that the UrQMD essentially always adds more flow to the $v_2^{\mathrm{final}}\{4\}$ with the increase of v_2^{initial}, but the $v_2^{\mathrm{final}}\{4\}$ is non-additive at low-p_{T} and intermediate-p_{T}. For a smaller v_2^{initial} values the UrQMD adds flow to the $v_2^{\mathrm{final}}\{4\}$ and for a higher v_2^{initial} values the UrQMD removes one part of the $v_2^{\mathrm{final}}\{4\}$. One interesting point in these results is that v_2^{initial} value to recover the v_2 measured by ALICE need to be about as the same v_2^{final} desired flow at low- and intermediate- p_{T} ranges. For a high-p_{T} above 2.5 GeV/c we can see a change in the behavior of the $v_2^{\mathrm{final}}\{4\}$, when we reach the v_2^{initial} around 60% of the ALICE v_2 the UrQMD continues to add more flow to the $v_2^{\mathrm{final}}\{4\}$. For completeness, we also show the v_2 predicted by the hydrodynamic

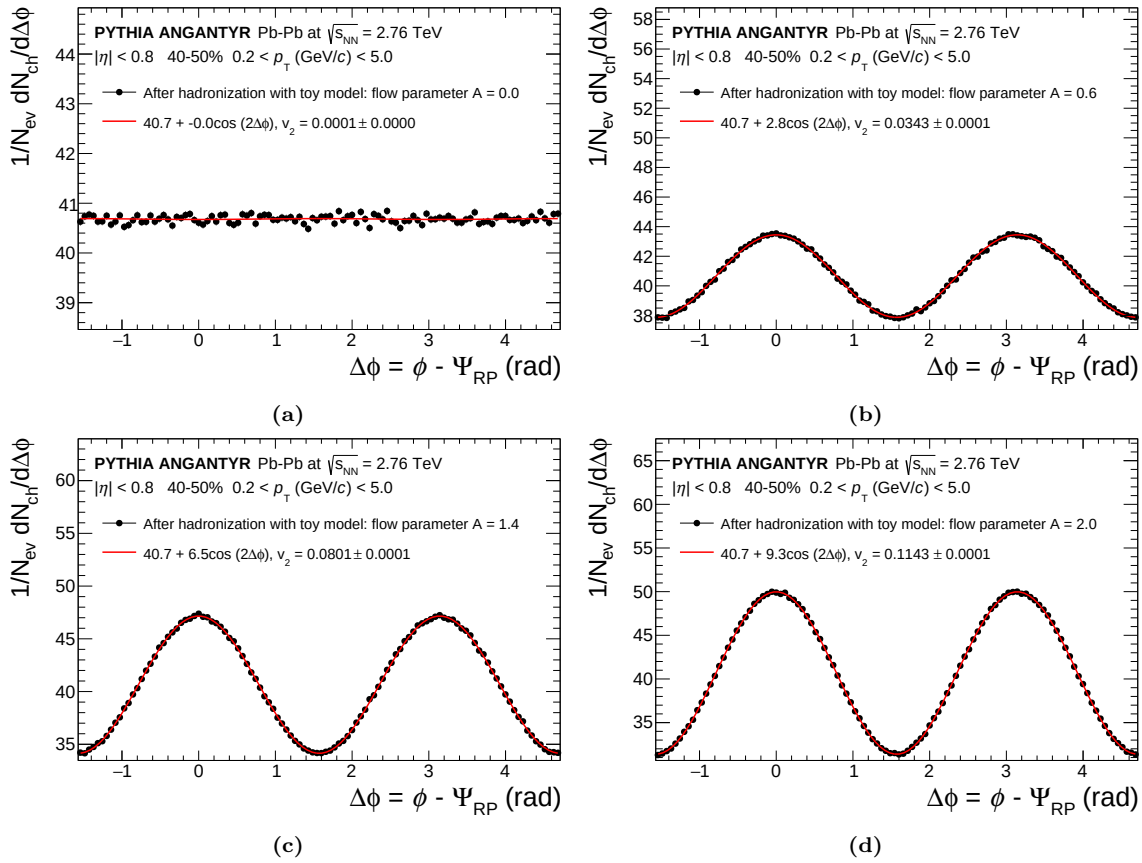

Figure 3.18: Azimuthal distribution of charged-particles $(1/\mathrm{N_{ev}})\mathrm{dN_{ch}}/\mathrm{d}\Delta\phi$, where $\Delta\phi = \phi - \Psi_{\mathrm{RP}}$ is the azimuth angle (ϕ) with respect to reaction plane angle (Ψ_{RP}), in $|\eta| < 0.8$ and $0.2 < p_{\mathrm{T}}$ (GeV/c) < 5.0. These distributions are events generated by the PYTHIA/Angantyr in Pb–Pb collisions at $\sqrt{s_{\mathrm{NN}}} = 2.76$ TeV after hadronization with the toy model implemented, normalized by the number of events ($\mathrm{N_{ev}}$). Each distribution is for one flow parameter A, the Figures **(a)** A = 0.0,**(b)** A = 0.6, **(c)** A = 1.4 and **(d)** A = 2.0, in the centrality bin $40-50\%$. The red curve represent the fit by one function $\cos(2\Delta\phi)$ that is used to calculate v_2.

simulations to have an idea about the UrQMD response in hydrodynamics simulations and we conclude that UrQMD adds a little more flow to the $v_2^{\mathrm{final}}\{4\}$ also in that case.

To determine the upper and lower limits to the acceptable initial flow as a function of p_{T}, we did linear fits to the points of $v_2^{\mathrm{final}}\{4\} \pm \sigma(\text{Error bar})$ from the toy model predictions, as shown in Fig. 3.20, where the linear fits intercept the upper and lower limits of the gray band. With this, we effectively computed the upper and lower limits to the acceptable initial flow as a function of p_{T}, as shown in Fig. 3.21. In this figure, the green band marks the region in which the initial flow has to be contained in so that the final flow is within uncertainties of the $v_2\{4\}$ measured by ALICE. It is striking that, while for low-p_{T}, the v_2^{initial} needs to be approximately the same as the $v_2^{\mathrm{final}}\{4\}$, this is not true for intermediate and high p_{T}. In that region, the acceptable initial flow is actually significantly below the desired $v_2^{\mathrm{final}}\{4\}$ by a factor of 2 or even more.

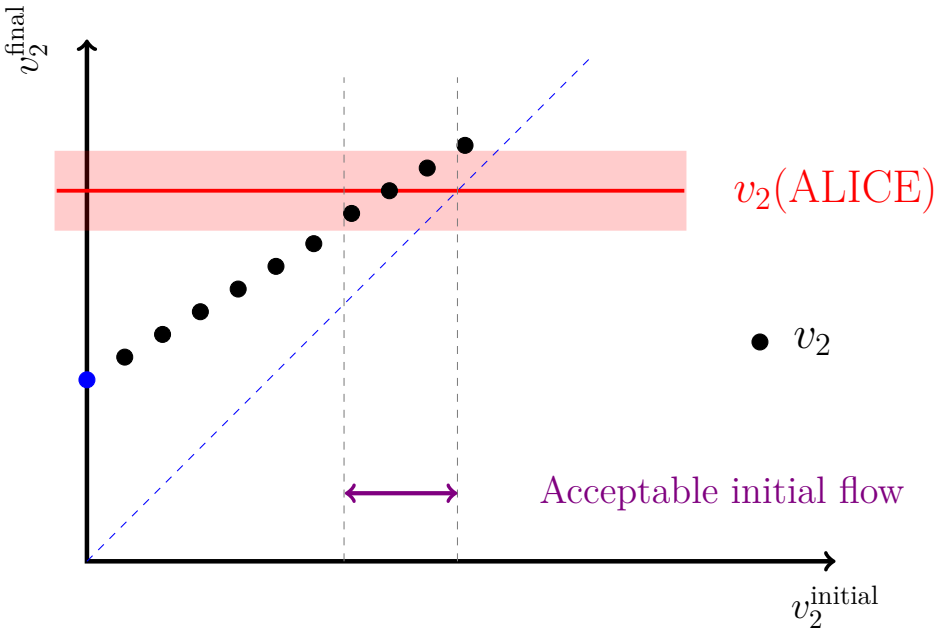

Figure 3.19: The elliptic flow v_2^{final} as a function of v_2^{initial}, where we change the initial flow until the final flow match the value measured by the ALICE collaboration [75] within experimental uncertainty represented by the red box. The black points inside the red box are the value of acceptable initial flow to recover the ALICE v_2. In the blue point we have zero for v_2^{initial} (A = 0.0) and the v_2^{final} for the hybrid model corresponds approximately 60% of the v_2 observed by ALICE.

Overall, it is now clear that the UrQMD response is not strictly additive, meaning that UrQMD does not always simply add 60% of the expected flow value. If given an initial flow, UrQMD will still add extra flow on top, but the intensity with which it does that is decreased for an increasing initial flow, especially at low-p_{T}. Despite this fact, our results demonstrate that at mid-p_{T} the v_2^{initial} required to reach ALICE measurements is significantly below the actual ALICE measurements themselves in our simulation chain. This is very important for the PYTHIA/Angantyr developers: they are currently considering models such as string shoving that may lead to an initial (to the hadronic phase) elliptic flow and our results essentially serve to point out that whatever they do in PYTHIA/Angantyr without UrQMD does not have to match the full $v_2^{\text{final}}\{4\}$ measured by ALICE except perhaps at low momenta.

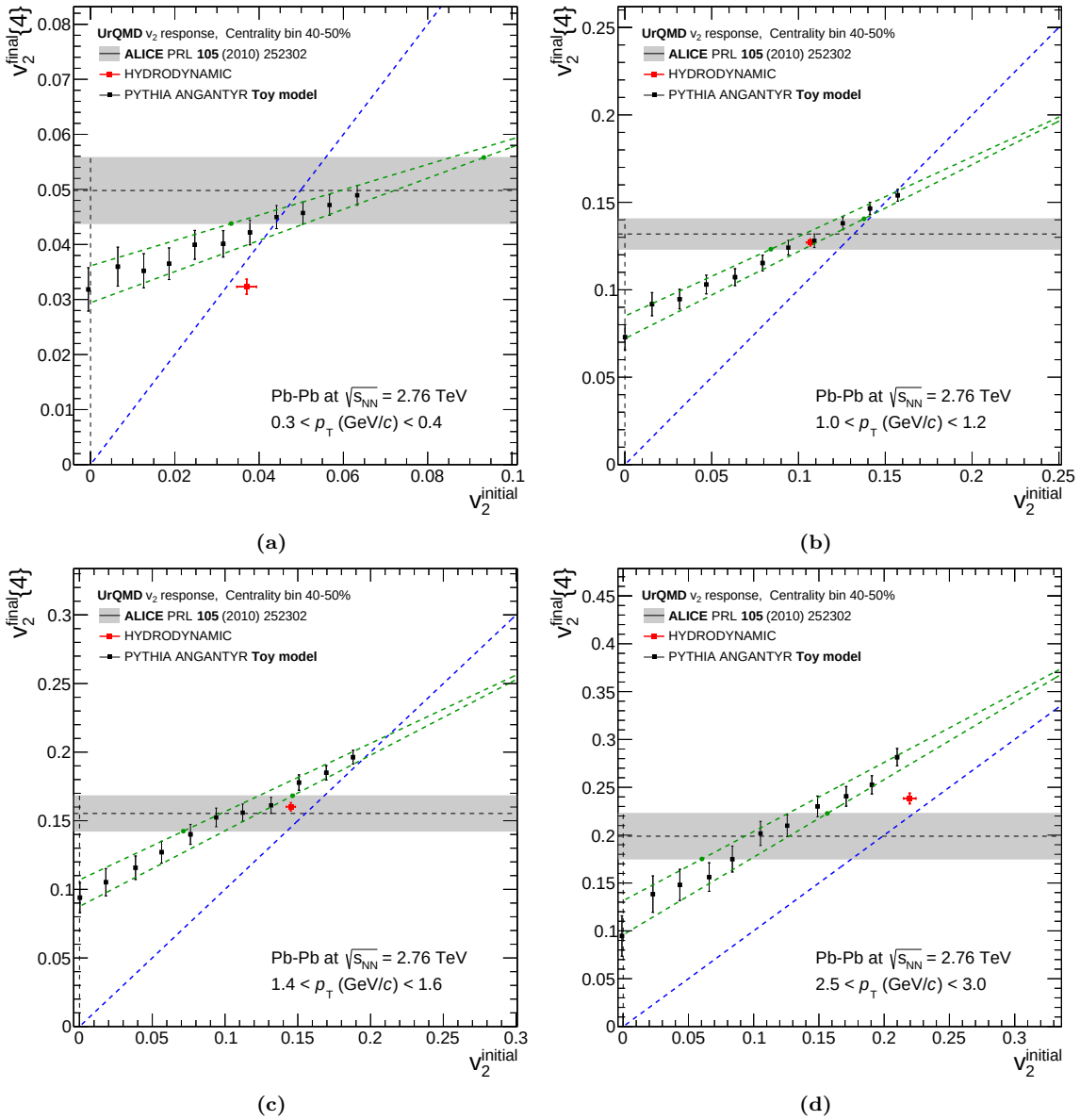

Figure 3.20: Elliptic flow $v_2^{\text{final}}\{4\}$ as a function of v_2^{initial}, where the v_2^{initial} was generated by the PYTHIA/Angantyr in Pb–Pb collisions at $\sqrt{s_{\text{NN}}} = 2.76$ TeV and the $v_2^{\text{final}}\{4\}$ generated by the UrQMD with hadronic interactions enabled. The $v_2^{\text{final}}\{4\}$ and v_2^{initial} were calculated at low-p_{T} range **(a)**, intermediate-p_{T} range **(b, c)** and high-p_{T} range **(d)** compared to the measurement by the ALICE collaboration [75]. The red points are model predictions from the hydrodynamic simulations with same p_{T} range for the centrality of $40-50\%$. The black dashed line and gray box are $v_2\{4\}$ measured and the experimental uncertainty for the ALICE data, respectively. The green dashed lines are the linear fits for the points $v_2^{\text{final}}\{4\} \pm \sigma(\text{Error bar})$ to determine the upper and lower limits to the acceptable initial flow that are represented by the green points intercepting the upper and lower limits of the gray band.

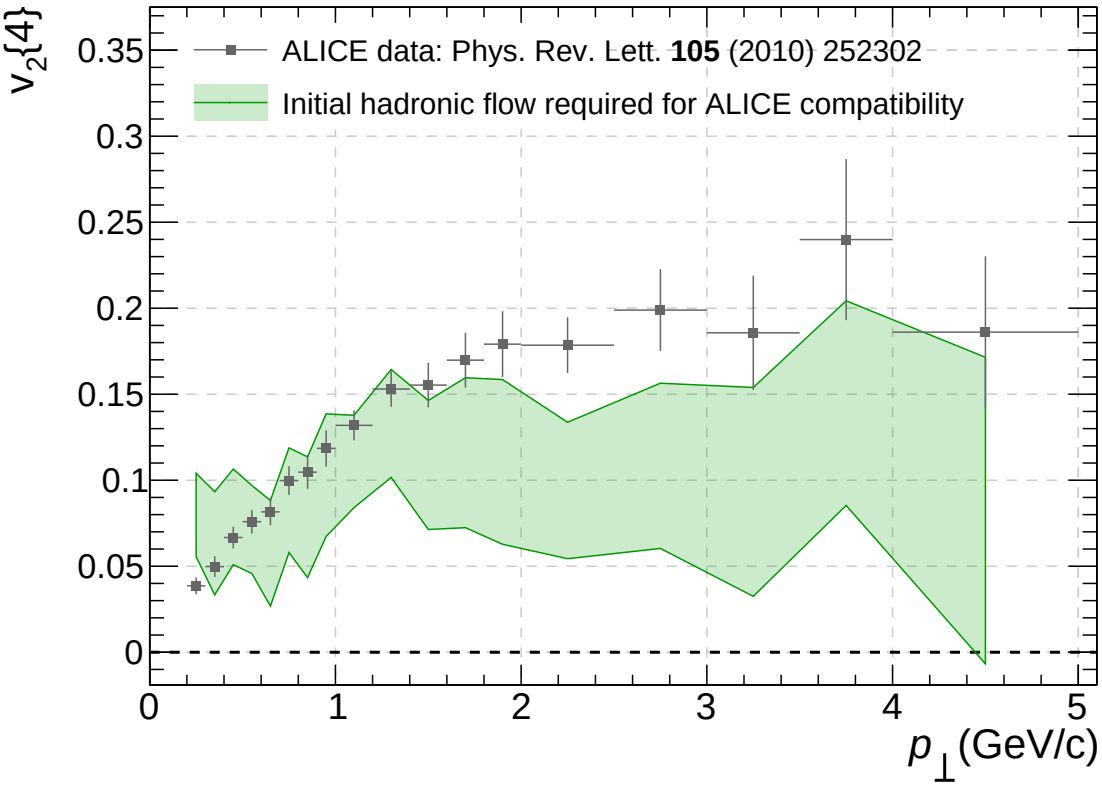

Figure 3.21: p_{T}-differential elliptic flow $v_2\{4\}$ as a function of p_{T} for the centrality of $40-50\%$, where the data points measured by the ALICE collaboration [75] and the light green band represents the region of acceptable initial hadronic flow to recover the $v_2\{4\}$ measured by ALICE.

Chapter 4

Conclusion

In this work, we have discussed three basic aspects of an improved baseline for heavy-ion collisions: the nuclear modification factor, two-particle correlations and elliptic flow. The fact that the nuclear modification factor calculated using PYTHIA/Angantyr + UrQMD simulations follows the qualitative trend of the measured R_{AA} at intermediate-p_{T} once hadronic interactions are considered is an intriguing observation in itself. As explained in the introduction, values for R_{AA} below unity are generally taken as a clear indication of QGP formation, and models incorporating QGP formation are, as a general rule, needed to describe the data. In PYTHIA/Angantyr + UrQMD there is no assumption of a QGP phase, but nevertheless several effects contribute to the description of R_{AA}.

The high-p_{T} part of the spectra generated by PYTHIA/Angantyr deviates from the simple binary scaling which is normally expected [37], as seen also in the fact that the R_{AA} is constant but below unity for high-p_{T} even without hadronic interactions. As previously explained, PYTHIA/Angantyr makes a distinction between various types of nucleon–nucleon interactions, which will contribute differently to high-p_{T} particle yields, and as a result the high-p_{T} R_{AA} does not converge to unity even if hadronic interactions are disabled. This effect is responsible for the majority of the deviation from unity, as seen in Fig. 3.6. There are, however, model uncertainties associated with this effect. While the treatment of secondary absorptive sub-collisions similar to diffractive excitations can be theoretically and numerically motivated [63], it is, as mentioned earlier, not clear that it will exactly reproduce the phenomenology of an interleaved shower plus color reconnection. An obvious next step would be to study the (absence of) nuclear modification in

p-Pb collisions within PYTHIA/Angantyr + UrQMD. However, in that case, model uncertainties are much larger than in AA collisions. It was shown in ref. [63] that secondary collisions contribute between 25-40% in Pb-Pb collisions at $\sqrt{s_{\mathrm{NN}}} = 2.76$ TeV, while for p-Pb collisions at $\sqrt{s_{\mathrm{NN}}} = 5.02$ TeV they contribute between 50-85%.

An equally important conclusion from this work is the influence from the hadronic rescattering phase on R_{AA}. Since strings have an average life-time $\langle\tau^2\rangle \approx 2$ fm/c, the hadronic phase is longer, and with a more dense initial condition, than for hydrodynamic simulations where a QGP phase lives for up to an order of magnitude longer. We have shown that a hadronic rescattering phase with such an early starting time modifies R_{AA} up to a factor 3 for intermediate-p_{T} particles in central Pb-Pb events. From this model, we can interpret that at intermediate-p_{T}, hadronic interactions lead to a suppression of particle yields as hadrons lose significant momentum to more abundant low-p_{T} particles. However, this effect subsides for very large transverse momentum, such that the R_{AA} will eventually converge to the value without hadronic interactions. This is because, in the hadron vertex model, higher-p_{T} values correlate with more displaced hadron creation vertices due to the linear relationship between space-time and momentum, visible also in Fig. 2.6. Since higher-p_{T} particles are then increasingly displaced, these are less likely to interact with the remainder of the system. While this effect is smaller in magnitude than the deviation from binary scaling, it is crucial to recover the minimum of the nuclear modification factor at around 5 GeV/c and the subsequent rise at high momenta. It should be noted here that the main model uncertainty in this part lies in the determination of the vertex position. The relation in space-time leads directly to a hadron production point as the average of two subsequent break-up points. As noted in ref. [96], this definition is not unique, but could differ from the average up to $\pm p_h/2\kappa$, where p_h is the hadron four-momentum. Taking this at face value, the uncertainty of the final value for R_{AA} would be large enough that the high-p_{T} rise is not visible within uncertainties.

It has to be noted that the intermediate to high-p_{T} suppression studied in this work is fundamentally different than the one that would result from models such as JETSCAPE or JEWEL [127]. In the work, jet quenching is a phenomenon associated to partonic energy loss, which would lead to the suppression of an entire high-momentum jet, while in the former, individual hadrons lose momentum after hadronization. Experimentally, these two scenarios can be distinguished using techniques such as two-particle correlations and dijet

asymmetry measurements. It is with this motivation that we pursued the studies shown in Fig. 3.9, which indicate that the high-momentum particle suppression from hadronic rescattering follows, in fact, again the same qualitative trend as what was observed by the STAR Collaboration at RHIC [46, 128], with the near-side jet being mostly unaltered and the away-side jet being suppressed due to a larger number of interactions with the hadronic medium. These findings are complementary to recent studies on the effect of hadronic rescattering on jet shapes [129] which also indicate that the hadronic phase does have significant impact on high-p_{T} physics observables.

As shown in Fig. 3.14, the v_2^{Fit} with hadronic interaction enabled is capable of describing approximately 60% of magnitude the one measured by the ALICE Collaboration. We also found similar results for $v_2\{2\}$ and $v_2\{4\}$ compared with the ALICE data, where $v_2\{2\}$ is greater than $v_2\{4\}$ because it is more affected by the non-flow contributions like resonance decays and jet correlations. We also calculated p_{T}-differential elliptic flow shown in Fig. 3.15, we observed that the p_{T}-differential v_2^{Fit} and $v_2\{4\}$ from the model can describe around 60% of the magnitude of the v_2 measured by the ALICE Collaboration, consistent with the results found in the integrated elliptic flow. The results from the PYTHIA/Angantyr + UrQMD hybrid model were submitted to Physical Review C and the preprint is available on ArXiv [84] already now.

An important test performed as part of this work is the toy model work, in which UrQMD response to a given initial hadronic flow was tested systematically. The results show that, in fact, the flow at hadronization level in the PYTHIA/Angantyr model does not need to be fully compatible with the measured ALICE flow at mid- to high-p_{T}, since UrQMD will add some flow on top of the existing one. This finding is also very important for model building and for the PYTHIA/Angantyr authors and will find its way into a publication in the near future.

There are several extensions of this work that are possible and will be pursued soon. One important consideration is the possibility of separating very high density regions of the PYTHIA/Angantyr hadronization profile and evolving those regions using hydrodynamics simulators instead of a hadronic transport model. This is already being pursued by a masters student in our group. In addition, a systematic extension of this work to small collision systems, such as pp and p-Pb, might also prove very interesting on its own. This is especially important because we could then compare our approach with a recent

improved PYTHIA version in which hadronic rescattering is possible in pp collisions, a new development done by the main PYTHIA author, Torbjörn Sjöstrand [130].

In conclusion, the findings of this work prompt present and future experimental studies to put more emphasis in the construction of baseline, no-QGP models, as a certain fraction of the observations normally exclusively associated with the QGP may have its origin elsewhere. Phrased differently, this work conclusively demonstrates that comparing experimental data with an incoherent superposition of proton-proton collisions is not a valid exercise to fully isolate QGP-specific equilibration signatures.

Bibliography

1. Thomson, M. *Modern particle physics* (Cambridge University Press, 2013).
2. Fritzsch, H., Gell-Mann, M. & Leutwyler, H. Advantages of the Color Octet Gluon Picture. *Phys. Lett. B* **47,** 365–368 (1973).
3. Skands, P. *Introduction to QCD* in *Proceedings, Theoretical Advanced Study Institute in Elementary Particle Physics: Searching for New Physics at Small and Large Scales (TASI 2012): Boulder, Colorado, June 4-29, 2012* (2017), 63–124. arXiv: 1207.2389 [hep-ph].
4. Adcox, K. *et al.* Formation of dense partonic matter in relativistic nucleus-nucleus collisions at RHIC: Experimental evaluation by the PHENIX collaboration. *Nucl. Phys.* **A757,** 184–283. arXiv: nucl-ex/0410003 [nucl-ex] (2005).
5. Back, B. B. *et al.* The PHOBOS perspective on discoveries at RHIC. *Nucl. Phys.* **A757,** 28–101. arXiv: nucl-ex/0410022 [nucl-ex] (2005).
6. Arsene, I. *et al.* Quark gluon plasma and color glass condensate at RHIC? The Perspective from the BRAHMS experiment. *Nucl. Phys.* **A757,** 1–27. arXiv: nucl-ex/0410020 [nucl-ex] (2005).
7. Adams, J. *et al.* Experimental and theoretical challenges in the search for the quark gluon plasma: The STAR Collaboration's critical assessment of the evidence from RHIC collisions. *Nucl. Phys.* **A757,** 102–183. arXiv: nucl-ex/0501009 [nucl-ex] (2005).
8. Hong, B. Nuclear Matter Under Extreme Conditions: from Quark-Gluon Plasma to Neutron Stars. *J. Korean Phys. Soc.* **72,** 1515–1522 (2018).
9. Trainor, T. A. A critical review of RHIC experimental results. *Int. J. Mod. Phys.* **E23,** 1430011. arXiv: 1303.4774 [hep-ph] (2014).

10. Foka, P. & Janik, M. A. An overview of experimental results from ultra-relativistic heavy-ion collisions at the CERN LHC: Bulk properties and dynamical evolution. *Reviews in Physics* **1,** 154 –171. ISSN: 2405-4283. http://www.sciencedirect.com/science/article/pii/S2405428316300156 (2016).

11. Pasechnik, R. & Šumbera, M. Phenomenological Review on Quark–Gluon Plasma: Concepts vs. Observations. *Universe* **3,** 7. arXiv: 1611.01533 [hep-ph] (2017).

12. Wilson, K. G. Confinement of Quarks (ed Taylor, J.) 45–59 (Feb. 1974).

13. Bali, G. S. QCD forces and heavy quark bound states. *Phys. Rept.* **343,** 1–136. arXiv: hep-ph/0001312 (2001).

14. Gell-Mann, M. A Schematic Model of Baryons and Mesons. *Phys. Lett.* **8,** 214–215 (1964).

15. Gross, D. J. & Wilczek, F. Ultraviolet Behavior of Nonabelian Gauge Theories. *Phys. Rev. Lett.* **30** (ed Taylor, J.) 1343–1346 (1973).

16. Bali, G. & Schilling, K. Static quark - anti-quark potential: Scaling behavior and finite size effects in SU(3) lattice gauge theory. *Phys. Rev. D* **46,** 2636–2646 (1992).

17. Feynman, R. P. *QED: The strange theory of light and matter* (Princeton University Press, 2006).

18. Deur, A., Brodsky, S. J. & de Teramond, G. F. The QCD Running Coupling. *Prog. Part. Nucl. Phys.* **90,** 1–74. arXiv: 1604.08082 [hep-ph] (2016).

19. Politzer, H. Reliable Perturbative Results for Strong Interactions? *Phys. Rev. Lett.* **30** (ed Taylor, J.) 1346–1349 (1973).

20. Tanabashi, M. *et al.* Review of Particle Physics. *Phys. Rev. D* **98,** 030001 (2018).

21. Satz, H. *Extreme States of Matter in Strong Interaction Physics: An Introduction* ISBN: 978-3-319-71893-4, 978-3-319-71894-1 (Springer, Cham, 2018).

22. Bazavov, A. *et al.* Equation of state and QCD transition at finite temperature. *Phys. Rev. D* **80,** 014504. arXiv: 0903.4379 [hep-lat] (2009).

23. Cabibbo, N. & Parisi, G. Exponential Hadronic Spectrum and Quark Liberation. *Phys. Lett. B* **59,** 67–69 (1975).

24. Bjorken, J. Highly Relativistic Nucleus-Nucleus Collisions: The Central Rapidity Region. *Phys. Rev. D* **27,** 140–151 (1983).

25. Hippolyte, B. *Heavy-ion session: a (quick) introduction* in *Proceedings, 48th Rencontres de Moriond on QCD and High Energy Interactions: La Thuile, Italy, March 9-16, 2013* (2013), 201–206.

26. Evans, L. & Bryant, P. LHC Machine. *JINST* **3,** S08001. http://iopscience.iop.org/article/10.1088/1748-0221/3/08/S08001/pdf (2008).

27. Aamodt, K. *et al.* The ALICE experiment at the CERN LHC. *JINST* **3,** S08002 (2008).

28. Aad, G. *et al.* The ATLAS Experiment at the CERN Large Hadron Collider. *JINST* **3,** S08003 (2008).

29. Aad, G. *et al.* Observation of a new particle in the search for the Standard Model Higgs boson with the ATLAS detector at the LHC. *Phys. Lett. B* **716,** 1–29. arXiv: 1207.7214 [hep-ex] (2012).

30. Chatrchyan, S. *et al.* The CMS Experiment at the CERN LHC. *JINST* **3,** S08004 (2008).

31. Chatrchyan, S. *et al.* Observation of a New Boson at a Mass of 125 GeV with the CMS Experiment at the LHC. *Phys. Lett. B* **716,** 30–61. arXiv: 1207.7235 [hep-ex] (2012).

32. Alves A.Augusto, J. *et al.* The LHCb Detector at the LHC. *JINST* **3,** S08005 (2008).

33. La Rocca, P. & Riggi, F. The upgrade programme of the major experiments at the Large Hadron Collider. *J. Phys. Conf. Ser.* **515** (eds Giardina, G., Nasirov, A. K. & Mandaglio, G.) 012012 (2014).

34. Daw, E. Lecture 7 Rapidity and Pseudorapidity. *URL http://www. hep. shef. ac. uk/edaw/PHY206/Site/2012_course_files/phy206rlec7. pdf* (2012).

35. Aamodt, K *et al.* Transverse momentum spectra of charged particles in proton-proton collisions at $\sqrt{s} = 900$ GeV with ALICE at the LHC. *Phys. Lett.* **B693,** 53–68. arXiv: 1007.0719 [hep-ex] (2010).

36. Glauber, R. Cross-sections in deuterium at high-energies. *Phys. Rev.* **100,** 242–248 (1955).

37. Miller, M. L., Reygers, K., Sanders, S. J. & Steinberg, P. Glauber modeling in high energy nuclear collisions. *Ann. Rev. Nucl. Part. Sci.* **57,** 205–243. arXiv: nucl-ex/0701025 [nucl-ex] (2007).

38. Abelev, B. *et al.* Centrality determination of Pb-Pb collisions at $\sqrt{s_{NN}} = 2.76$ TeV with ALICE. *Phys. Rev.* **C88,** 044909. arXiv: 1301.4361 [nucl-ex] (2013).

39. Busza, W., Rajagopal, K. & van der Schee, W. Heavy Ion Collisions: The Big Picture, and the Big Questions. arXiv: 1802.04801 [hep-ph] (2018).

40. Rafelski, J. & Muller, B. Strangeness Production in the Quark - Gluon Plasma. *Phys. Rev. Lett.* **48.** [Erratum: Phys. Rev. Lett.56,2334(1986)], 1066 (1982).

41. Bjorken, J. Energy Loss of Energetic Partons in Quark - Gluon Plasma: Possible Extinction of High p(t) Jets in Hadron - Hadron Collisions (Aug. 1982).

42. Bilandzic, A. *Anisotropic flow measurements in ALICE at the large hadron collider* PhD thesis (Utrecht U., 2012).

43. Zhou, Y. *Anisotropic Flow and Flow Fluctuations at the Large Hadron Collider* PhD thesis (Utrecht U., 2016).

44. Wang, X.-N. & Gyulassy, M. Gluon shadowing and jet quenching in A + A collisions at s**(1/2) = 200-GeV. *Phys. Rev. Lett.* **68,** 1480–1483 (1992).

45. Maksiak, B. *Two-particle correlations in p+p and Pb+Pb collisions at SPS energies. Korelacje dwucząstkowe w zderzeniach p+p oraz Pb+Pb przy energiach akceleratora SPS* Presented 20 Apr 2017 (Nov. 2016). https://cds.cern.ch/record/2261389.

46. Adams, J. *et al.* Evidence from d + Au measurements for final state suppression of high p(T) hadrons in Au+Au collisions at RHIC. *Phys. Rev. Lett.* **91,** 072304. arXiv: nucl-ex/0306024 [nucl-ex] (2003).

47. Afanasiev, S. *et al.* Measurement of Direct Photons in Au+Au Collisions at $\sqrt{s_{NN}} =$ 200 GeV. *Phys. Rev. Lett.* **109,** 152302. arXiv: 1205.5759 [nucl-ex] (2012).

48. Chatrchyan, S. *et al.* Measurement of isolated photon production in *pp* and PbPb collisions at $\sqrt{s_{NN}} = 2.76$ TeV. *Phys. Lett. B* **710,** 256–277. arXiv: 1201.3093 [nucl-ex] (2012).

49. Chatrchyan, S. *et al.* Study of W boson production in PbPb and *pp* collisions at $\sqrt{s_{NN}} = 2.76$ TeV. *Phys. Lett. B* **715,** 66–87. arXiv: 1205.6334 [nucl-ex] (2012).

50. Chatrchyan, S. *et al.* Study of Z production in PbPb and pp collisions at $\sqrt{s_{\mathrm{NN}}}$ = 2.76 TeV in the dimuon and dielectron decay channels. *JHEP* **03,** 022. arXiv: 1410.4825 [nucl-ex] (2015).

51. Adcox, K. *et al.* Suppression of hadrons with large transverse momentum in central Au+Au collisions at $\sqrt{s_{NN}}$ = 130-GeV. *Phys. Rev. Lett.* **88,** 022301. arXiv: nucl-ex/0109003 (2002).

52. Adler, C. *et al.* Centrality dependence of high p_T hadron suppression in Au+Au collisions at $\sqrt{s}_{NN}$ = 130-GeV. *Phys. Rev. Lett.* **89,** 202301. arXiv: nucl-ex/0206011 (2002).

53. Adare, A. *et al.* Suppression pattern of neutral pions at high transverse momentum in Au+Au collisions at $\sqrt{s_{NN}}$ = 200 GeV and constraints on medium transport coefficients. *Phys. Rev. Lett.* **101,** 232301. arXiv: 0801.4020 [nucl-ex] (2008).

54. Aamodt, K. *et al.* Suppression of Charged Particle Production at Large Transverse Momentum in Central Pb-Pb Collisions at $\sqrt{s_{NN}}$ = 2.76 TeV. *Phys. Lett. B* **696,** 30–39. arXiv: 1012.1004 [nucl-ex] (2011).

55. Abelev, B. *et al.* Centrality Dependence of Charged Particle Production at Large Transverse Momentum in Pb–Pb Collisions at $\sqrt{s_{\mathrm{NN}}}$ = 2.76 TeV. *Phys. Lett. B* **720,** 52–62. arXiv: 1208.2711 [hep-ex] (2013).

56. Chatrchyan, S. *et al.* Study of high-pT charged particle suppression in PbPb compared to *pp* collisions at $\sqrt{s_{NN}}$ = 2.76 TeV. *Eur. Phys. J. C* **72,** 1945. arXiv: 1202.2554 [nucl-ex] (2012).

57. Aad, G. *et al.* Measurement of charged-particle spectra in Pb+Pb collisions at $\sqrt{s_{\mathrm{NN}}}$ = 2.76 TeV with the ATLAS detector at the LHC. *JHEP* **09,** 050. arXiv: 1504.04337 [hep-ex] (2015).

58. Chatrchyan, S. *et al.* Observation of Long-Range Near-Side Angular Correlations in Proton-Lead Collisions at the LHC. *Phys. Lett.* **B718,** 795–814. arXiv: 1210.5482 [nucl-ex] (2013).

59. Chatrchyan, S. *et al.* Multiplicity and Transverse Momentum Dependence of Two- and Four-Particle Correlations in pPb and PbPb Collisions. *Phys. Lett.* **B724,** 213–240. arXiv: 1305.0609 [nucl-ex] (2013).

60. Chatrchyan, S. *et al.* Long-range and short-range dihadron angular correlations in central PbPb collisions at a nucleon-nucleon center of mass energy of 2.76 TeV. *JHEP* **07,** 076. arXiv: 1105.2438 [nucl-ex] (2011).

61. Chatrchyan, S. *et al.* Centrality dependence of dihadron correlations and azimuthal anisotropy harmonics in PbPb collisions at $\sqrt{s_{NN}} = 2.76$ TeV. *Eur. Phys. J. C* **72,** 2012. arXiv: 1201.3158 [nucl-ex] (2012).

62. Bierlich, C., Gustafson, G. & Lönnblad, L. Diffractive and non-diffractive wounded nucleons and final states in p**A** collisions. *JHEP* **10,** 139. arXiv: 1607.04434 [hep-ph] (2016).

63. Bierlich, C., Gustafson, G., Lönnblad, L. & Shah, H. The Angantyr model for Heavy-Ion Collisions in PYTHIA8. arXiv: 1806.10820 [hep-ph] (2018).

64. Snellings, R. Elliptic flow: a brief review. *New Journal of Physics* **13,** 055008. https://doi.org/10.1088%2F1367-2630%2F13%2F5%2F055008 (May 2011).

65. Alver, B. *et al.* System size dependence of cluster properties from two-particle angular correlations in Cu+Cu and Au+Au collisions at s(NN)**(1/2) = 200-GeV. *Phys. Rev.* **C81,** 024904. arXiv: 0812.1172 [nucl-ex] (2010).

66. Adams, J. *et al.* Distributions of charged hadrons associated with high transverse momentum particles in pp and Au + Au collisions at s(NN)**(1/2) = 200-GeV. *Phys. Rev. Lett.* **95,** 152301. arXiv: nucl-ex/0501016 [nucl-ex] (2005).

67. Khachatryan, V. *et al.* Observation of Long-Range Near-Side Angular Correlations in Proton-Proton Collisions at the LHC. *JHEP* **09,** 091. arXiv: 1009.4122 [hep-ex] (2010).

68. Abelev, B. *et al.* Long-range angular correlations on the near and away side in p-Pb collisions at $\sqrt{s_{NN}} = 5.02$ TeV. *Phys. Lett. B* **719,** 29–41. arXiv: 1212.2001 [nucl-ex] (2013).

69. Aad, G. *et al.* Observation of Associated Near-Side and Away-Side Long-Range Correlations in $\sqrt{s_{NN}}$=5.02 TeV Proton-Lead Collisions with the ATLAS Detector. *Phys. Rev. Lett.* **110,** 182302. arXiv: 1212.5198 [hep-ex] (2013).

70. Yi, L. *Study of quark gluon plasma by particle correlations in heavy ion collisions* (Springer, 2016).

71. Qiu, Z. & Heinz, U. W. Event-by-event shape and flow fluctuations of relativistic heavy-ion collision fireballs. *Phys. Rev. C* **84,** 024911. arXiv: 1104.0650 [nucl-th] (2011).

72. Bilandzic, A., Snellings, R. & Voloshin, S. Flow analysis with cumulants: Direct calculations. *Phys. Rev. C* **83,** 044913. https://link.aps.org/doi/10.1103/PhysRevC.83.044913 (4 Apr. 2011).

73. Miller, M. & Snellings, R. Eccentricity fluctuations and its possible effect on elliptic flow measurements. arXiv: nucl-ex/0312008 (Dec. 2003).

74. Adler, C. *et al.* Elliptic flow from two and four particle correlations in Au+Au collisions at s(NN)**(1/2) = 130-GeV. *Phys. Rev. C* **66,** 034904. arXiv: nucl-ex/0206001 (2002).

75. Aamodt, K *et al.* Elliptic flow of charged particles in Pb-Pb collisions at 2.76 TeV. *Phys. Rev. Lett.* **105,** 252302. arXiv: 1011.3914 [nucl-ex] (2010).

76. Derradi de Souza, R., Koide, T. & Kodama, T. Hydrodynamic Approaches in Relativistic Heavy Ion Reactions. *Prog. Part. Nucl. Phys.* **86,** 35–85. arXiv: 1506.03863 [nucl-th] (2016).

77. Schenke, B., Jeon, S. & Gale, C. (3+1)D hydrodynamic simulation of relativistic heavy-ion collisions. *Phys. Rev. C* **82,** 014903. arXiv: 1004.1408 [hep-ph] (2010).

78. Schenke, B., Jeon, S. & Gale, C. Elliptic and triangular flow in event-by-event (3+1)D viscous hydrodynamics. *Phys. Rev. Lett.* **106,** 042301. arXiv: 1009.3244 [hep-ph] (2011).

79. Petersen, H., Steinheimer, J., Burau, G., Bleicher, M. & Stocker, H. A Fully Integrated Transport Approach to Heavy Ion Reactions with an Intermediate Hydrodynamic Stage. *Phys. Rev.* **C78,** 044901. arXiv: 0806.1695 [nucl-th] (2008).

80. Ryu, S. *et al.* Effects of bulk viscosity and hadronic rescattering in heavy ion collisions at energies available at the BNL Relativistic Heavy Ion Collider and at the CERN Large Hadron Collider. *Phys. Rev. C* **97,** 034910. arXiv: 1704.04216 [nucl-th] (2018).

81. Moreland, J. S., Bernhard, J. E. & Bass, S. A. Alternative ansatz to wounded nucleon and binary collision scaling in high-energy nuclear collisions. *Phys. Rev. C* **92,** 011901. arXiv: 1412.4708 [nucl-th] (2015).

82. Shen, C. *et al.* The iEBE-VISHNU code package for relativistic heavy-ion collisions. *Comput. Phys. Commun.* **199,** 61–85. arXiv: 1409.8164 [nucl-th] (2016).

83. Bleicher, M. *et al.* Relativistic hadron hadron collisions in the ultrarelativistic quantum molecular dynamics model. *J. Phys.* **G25,** 1859–1896. arXiv: hep-ph/9909407 [hep-ph] (1999).

84. Da Silva, A. V., Serenone, W. M., Dobrigkeit Chinellato, D., Takahashi, J. & Bierlich, C. Improved heavy-ion collision baseline based on perturbative QCD and hadronic rescattering. arXiv: 2002.10236 [hep-ph] (Feb. 2020).

85. Sjöstrand, T. *et al.* An Introduction to PYTHIA 8.2. *Comput. Phys. Commun.* **191,** 159–177. arXiv: 1410.3012 [hep-ph] (2015).

86. Söjstrand, T. & van Zijl, M. A Multiple Interaction Model for the Event Structure in Hadron Collisions. *Phys. Rev.* **D36,** 2019 (1987).

87. Sjöstrand, T. in, 191–225 (2019). arXiv: 1706.02166 [hep-ph].

88. Andersson, B., Gustafson, G., Ingelman, G. & Sjöstrand, T. Parton fragmentation and string dynamics. *Physics Reports* **97,** 31 –145. ISSN: 0370-1573. http://www.sciencedirect.com/science/article/pii/0370157383900807 (1983).

89. Andersson, B., Gustafson, G. & Soderberg, B. A General Model for Jet Fragmentation. *Z. Phys.* **C20,** 317 (1983).

90. Sjostrand, T. Jet Fragmentation of Nearby Partons. *Nucl. Phys.* **B248,** 469–502 (1984).

91. Andersson, B. The Lund model. *Camb. Monogr. Part. Phys. Nucl. Phys. Cosmol.* **7,** 1–471 (1997).

92. Gribov, V. Glauber corrections and the interaction between high-energy hadrons and nuclei. *Sov. Phys. JETP* **29,** 483–487 (1969).

93. Alver, B., Baker, M., Loizides, C. & Steinberg, P. The PHOBOS Glauber Monte Carlo. arXiv: 0805.4411 [nucl-ex] (2008).

94. Pi, H. An Event generator for interactions between hadrons and nuclei: FRITIOF version 7.0. *Comput. Phys. Commun.* **71,** 173–192 (1992).

95. Bialas, A., Bleszynski, M. & Czyz, W. Multiplicity Distributions in Nucleus-Nucleus Collisions at High-Energies. *Nucl. Phys.* **B111,** 461–476 (1976).

96. Ferreres-Solé, S. & Sjöstrand, T. The space–time structure of hadronization in the Lund model. *Eur. Phys. J.* **C78,** 983. arXiv: 1808.04619 [hep-ph] (2018).

97. Bass, S. *et al.* Microscopic models for ultrarelativistic heavy ion collisions. *Prog. Part. Nucl. Phys.* **41,** 255–369. arXiv: nucl-th/9803035 (1998).

98. Loizides, C. Glauber modeling of high-energy nuclear collisions at the subnucleon level. *Phys. Rev. C* **94,** 024914. https://link.aps.org/doi/10.1103/PhysRevC.94.024914 (2 Aug. 2016).

99. Vries, H. D., Jager, C. D. & Vries, C. D. Nuclear charge-density-distribution parameters from elastic electron scattering. *Atomic Data and Nuclear Data Tables* **36,** 495 –536. ISSN: 0092-640X. http://www.sciencedirect.com/science/article/pii/0092640X87900131 (1987).

100. Abe, F. *et al.* Observation of Rapidity Gaps in $\overline{p}p$ Collisions at 1.8 TeV. *Phys. Rev. Lett.* **74,** 855–859. https://link.aps.org/doi/10.1103/PhysRevLett.74.855 (6 Feb. 1995).

101. Abelev, B. *et al.* Measurement of inelastic, single- and double-diffraction cross sections in proton–proton collisions at the LHC with ALICE. *Eur. Phys. J.* **C73,** 2456. arXiv: 1208.4968 [hep-ex] (2013).

102. Aamodt, K. *et al.* Centrality dependence of the charged-particle multiplicity density at mid-rapidity in Pb-Pb collisions at $\sqrt{s_{NN}} = 2.76$ TeV. *Phys. Rev. Lett.* **106,** 032301. arXiv: 1012.1657 [nucl-ex] (2011).

103. Abelev, B. B. *et al.* Multiplicity dependence of the average transverse momentum in pp, p-Pb, and Pb-Pb collisions at the LHC. *Phys. Lett.* **B727,** 371–380. arXiv: 1307.1094 [nucl-ex] (2013).

104. Breakstone, A. *et al.* Multiplicity Dependence of the Average Transverse Momentum and of the Particle Source Size in pp Interactions at $\sqrt{s} = 62$-GeV, 44-GeV and 31-GeV. *Z. Phys.* **C33,** 333 (1987).

105. Albajar, C. *et al.* A Study of the General Characteristics of $p\bar{p}$ Collisions at $\sqrt{s}$ = 0.2-TeV to 0.9-TeV. *Nucl. Phys.* **B335,** 261–287 (1990).

106. Alexopoulos, T. *et al.* Multiplicity Dependence of the Transverse Momentum Spectrum for Centrally Produced Hadrons in Anti-proton - Proton Collisions at $\sqrt{s}$ = 1.8-tev. *Phys. Rev. Lett.* **60,** 1622 (1988).

107. Adams, J. *et al.* The Multiplicity dependence of inclusive p_t spectra from pp collisions at $\sqrt{s}$ = 200-GeV. *Phys. Rev.* **D74,** 032006. arXiv: nucl-ex/0606028 [nucl-ex] (2006).

108. Aaltonen, T. *et al.* Measurement of Particle Production and Inclusive Differential Cross Sections in $p\bar{p}$ Collisions at $\sqrt{s}$ = 1.96-TeV. *Phys. Rev.* **D79.** [Erratum: Phys. Rev.D82,119903(2010)], 112005. arXiv: 0904.1098 [hep-ex] (2009).

109. Khachatryan, V. *et al.* Charged Particle Multiplicities in pp Interactions at $\sqrt{s}$ = 0.9, 2.36, and 7 TeV. *JHEP* **01,** 079. arXiv: 1011.5531 [hep-ex] (2011).

110. Aad, G. *et al.* Charged-particle multiplicities in pp interactions measured with the ATLAS detector at the LHC. *New J. Phys.* **13,** 053033. arXiv: 1012.5104 [hep-ex] (2011).

111. Christiansen, J. R. & Skands, P. Z. String Formation Beyond Leading Colour. *JHEP* **08,** 003. arXiv: 1505.01681 [hep-ph] (2015).

112. Argyropoulos, S. & Sjöstrand, T. Effects of color reconnection on $t\bar{t}$ final states at the LHC. *JHEP* **11,** 043. arXiv: 1407.6653 [hep-ph] (2014).

113. Christiansen, J. R. & Sjöstrand, T. Color reconnection at future e^+ e^- colliders. *Eur. Phys. J.* **C75,** 441. arXiv: 1506.09085 [hep-ph] (2015).

114. Acharya, S. *et al.* Transverse momentum spectra and nuclear modification factors of charged particles in pp, p-Pb and Pb-Pb collisions at the LHC. *JHEP* **11,** 013. arXiv: 1802.09145 [nucl-ex] (2018).

115. Voloshin, S. A. Transverse radial expansion and directed flow. *Phys. Rev. C* **55,** 1630–1632. arXiv: nucl-th/9611038 (1997).

116. Centrality determination in heavy ion collisions. https://cds.cern.ch/record/2636623 (Aug. 2018).

117. Acharya, S. *et al.* Transverse momentum spectra and nuclear modification factors of charged particles in Xe-Xe collisions at $\sqrt{s_{\mathrm{NN}}} = 5.44$ TeV. *Phys. Lett.* **B788,** 166–179. arXiv: 1805.04399 [nucl-ex] (2019).

118. Andrade, R., Noronha, J. & Denicol, G. S. Jet quenching effects on the anisotropic flow at RHIC. *Nuclear Physics A* **932.** Hard Probes 2013, 432 –436. ISSN: 0375-9474. http://www.sciencedirect.com/science/article/pii/S0375947414002206 (2014).

119. Muller, B. Phenomenology of jet quenching in heavy ion collisions. *Phys. Rev.* **C67,** 061901. arXiv: nucl-th/0208038 [nucl-th] (2003).

120. Majumder, A. & [van Leeuwen], M. The theory and phenomenology of perturbative QCD based jet quenching. *Progress in Particle and Nuclear Physics* **66,** 41 –92. ISSN: 0146-6410. http://www.sciencedirect.com/science/article/pii/S0146641010000542 (2011).

121. Qin, G.-Y. & Wang, X.-N. Jet quenching in high-energy heavy-ion collisions. *Int. J. Mod. Phys.* **E24.** [,309(2016)], 1530014. arXiv: 1511.00790 [hep-ph] (2015).

122. Agakishiev, G. *et al.* Directed and elliptic flow of charged particles in Cu+Cu collisions at $\sqrt{s_{NN}} = 22.4$ GeV. *Phys. Rev.* **C85,** 014901. arXiv: 1109.5446 [nucl-ex] (2012).

123. Aad, G. *et al.* Measurement of the pseudorapidity and transverse momentum dependence of the elliptic flow of charged particles in lead-lead collisions at $\sqrt{s_{NN}} = 2.76$ TeV with the ATLAS detector. *Phys. Lett.* **B707,** 330–348. arXiv: 1108.6018 [hep-ex] (2012).

124. Bilandzic, A., Christensen, C. H., Gulbrandsen, K., Hansen, A. & Zhou, Y. Generic framework for anisotropic flow analyses with multiparticle azimuthal correlations. *Phys. Rev.* **C89,** 064904. arXiv: 1312.3572 [nucl-ex] (2014).

125. Lu, Y. *et al.* Anisotropic flow at RHIC: How unique is the number-of-constituent-quark scaling? *J. Phys.* **G32,** 1121–1130. arXiv: nucl-th/0602009 [nucl-th] (2006).

126. in. *Encyclopedia of Operations Research and Management Science* (eds Gass, S. I. & Fu, M. C.) 815–815 (Springer US, Boston, MA, 2013). ISBN: 978-1-4419-1153-7. https://doi.org/10.1007/978-1-4419-1153-7_200343.

127. Cao, S. *et al.* Multistage Monte-Carlo simulation of jet modification in a static medium. *Phys. Rev. C* **96,** 024909. arXiv: 1705.00050 [nucl-th] (2017).

128. Adler, C. *et al.* Disappearance of back-to-back high p_T hadron correlations in central Au+Au collisions at $\sqrt{s_{NN}}$ = 200-GeV. *Phys. Rev. Lett.* **90,** 082302. arXiv: nucl-ex/0210033 (2003).

129. Dorau, P., Rose, J.-B., Pablos, D. & Elfner, H. Jet quenching in the hadron gas: An exploratory study. *Phys. Rev. C* **101,** 035208. https://link.aps.org/doi/10.1103/PhysRevC.101.035208 (3 Mar. 2020).

130. Sjöstrand, T. & Utheim, M. A Framework for Hadronic Rescattering in pp Collisions. arXiv: 2005.05658 [hep-ph] (May 2020).